STUDIES OF SURFACE STATES IN ZINC OXIDE NANOPOWDERS

by

RAUL MUGABE PETERS

Bachelor of Science, 2005

Midwestern State University

Wichita Falls, Texas

Submitted to the Graduate Faculty of the

College of Science and Engineering

Texas Christian University

in partial fulfillment of the requirements

for the degree of

Doctor of Philosophy

August 2010

Acknowledgements

I would like to gratefully and sincerely thank Dr. Yuri Strzhemechny for his understanding and patience during my graduate studies here at TCU. His mentorship was vital in providing a well-rounded experience consistent my long-term career goals and career objectives. His help and guidance have made this dissertation a reality.

I would also like to thank all of the members of our research group that I have worked with in the Nanoelectronics Optical Spectroscopy lab over the years. In particular to my colleague Jorge Antonio Paramo for all his help. I am thankful for the photoluminescence data and software support.

I would like thank Dr C. A. Quarles for allowing me to use the positron annihilation apparatus in his research lab. His help and suggestions have made a difference. I would also like to thank M. Murdoch, D. Yale (TCU Machine Shop), J. Katchinska (TCU Electronics Shop), and J. Cuanzon (TCU Glass Shop) for all the technical support provided.

I also extend my gratitude to my friends and family. I would like express gratitude to my parents, Anderson Peters and Julie Mae George, for their faith in me. Thank you for everything. Also I would like to thank Mr. And Mrs. Harris for the support that they have lent me during my stay in Fort Worth. I would also like to thank Mr. Fitzroy Henry for his support during my studies for his encouragement and support.

Finally, I would like to thank all the professors that I worked with here at TCU. I would like to thank Dr. Bruce Miller for his support in my development as a professional. I enjoyed the time working as a teaching assistant in the Physics of Music lab.

Contents

List of Figures

List of Tables

List of Abbreviations

AA – Alpha Aesar

AE – American Elements

AES – Auger electron spectroscopy

CCP – Capacitively coupled plasma

CFF – ConFlat flange

CFFD – Constant–fraction differential discriminator

CL – cathodoluminescence

CMA – Cylindrical mirror analyzer

CPD – Contact potential difference

EG – Electron gun

ICP – Inductively coupled plasma

LT – Lifetime

LL – Load lock

PAS – Positron annihilation spectroscopy

PL – Photoluminescence

PLT – Pellet

QTH – Quartz tungsten halogen

RF– Radio frequency

RP – Remote plasma

SA – Sigma Aldrich

SCR – Space charge region

SPV – Surface photovoltage spectroscopy

TAC – Time–to–amplitude converter

TC – Thermocouple

TMP – Turbomolecular pump

TSS – throttling SoftShut gate valve

UHV – Ultra high vacuum

UV – Ultraviolet

Z (ZA, ZB) – Zochem

Chapter I. Introduction

The scope of applications of semiconductor materials is truly remarkable and is growing by the day. Semiconductors can be generally characterized by the magnitude of their band gap, E_g [1]. The values of electrical resistivity of semiconductors generally fall in the range of 10^{-2} – 10^{9} Ω-cm at room temperature, intermediate between good conductors (10^{-6} Ω-cm) and insulators (10^{14} – 10^{22} Ω-cm) [2]. Their conductive properties are determined essentially by electrons and holes excited across the forbidden gap and bound charge carriers. These properties can be modified by thermal excitation, optical excitation, lattice defects, impurities or lack of stoichiometry [2].

Semiconductors can be categorized as elemental or compound. Most common semiconductors produce an average of four electrons per atom and the ionic character of the bonds varies based on the relative charge with respect to each other in the compound. The chemical formula AB for compound semiconductors is a useful nomenclature. For instance, a III-V compound exists when A is a trivalent element and B is a pentavalent element.

Impact of crystal lattice defects on the performance parameters of semiconductors may be beneficial or detrimental. Lattice defects occur in a variety of types. For example, edge and screw dislocations are defined as extended defects, while vacancies, interstitials, substitutional impurities and antisites (Figure 1.1) constitute point defects. The defects that cause the increase of electron (hole) concentration are called donors (acceptors). A semiconductor in which concentration of electrons (holes) is higher than the concentration of holes (electrons) is said to be an *n*-type (a *p*-type) semiconductor [3].

Most of the time, lattice defects give rise to electronic energy states (shallow donors, deep levels, and/or shallow acceptors) inside the band gap (Figure 1.2). Understanding and control of the defects' behavior in semiconductors is crucial for tailoring the underlying basic physical and chemical properties of the material of interest [4].

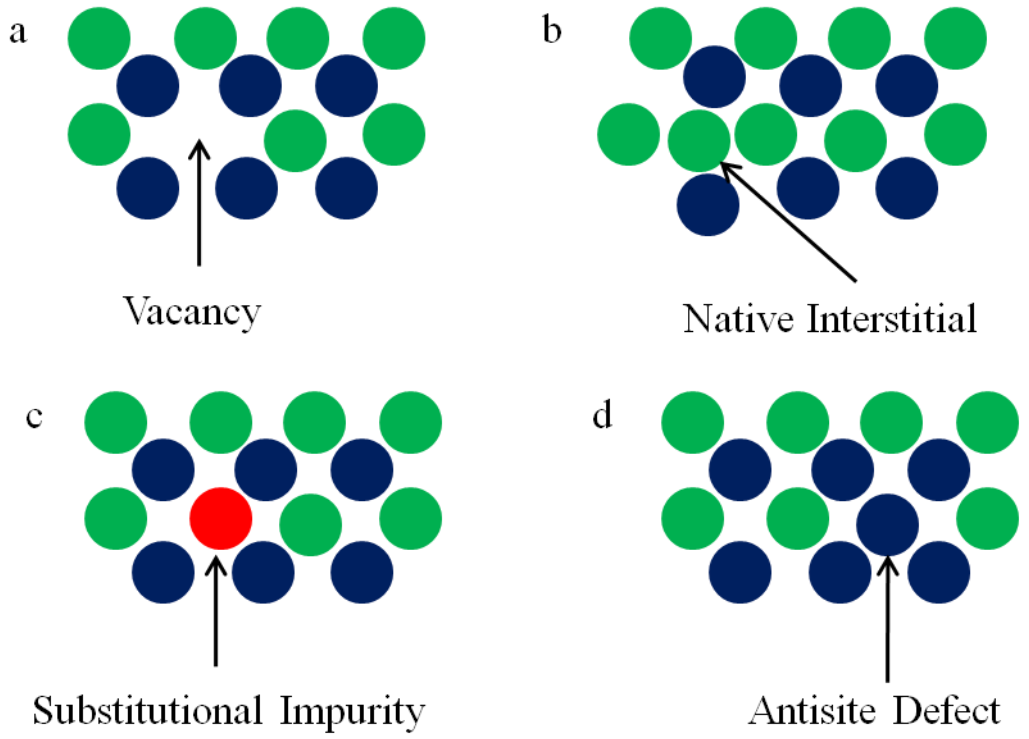

Figure 1.1: Examples of point defects in a crystal: (a) vacancy; (b) interstitial; (c) substitutional impurity; (d) antisite defect.

In our studies the semiconductor of interest is a II-VI compound zinc oxide (ZnO) with a wurtzite crystal structure (Figure 1.3, [5]). ZnO possesses a number of remarkable properties making it suitable for many current and potential applications such as ultraviolet (UV) light-emitting diodes, room temperature operated UV excitonic lasers, blue luminescent devices, etc. in concurrence with high speed and operating at high powers, high-temperatures, and in a high irradiation environments [4,6-9]. ZnO has a

wide direct band gap of ~ 3.3 eV at room temperature and unusually high exciton ionization energy of 60 meV [4, 6, 10]. Thus, excitons in ZnO are not easily thermally dissociated and the near band gap UV recombination is very efficient even at room temperature. An electron can make a transition between the allowed energy states by emitting a photon without the involvement of a phonon. ZnO also generally exhibits luminescence in the visible region of different wavelength ranges.

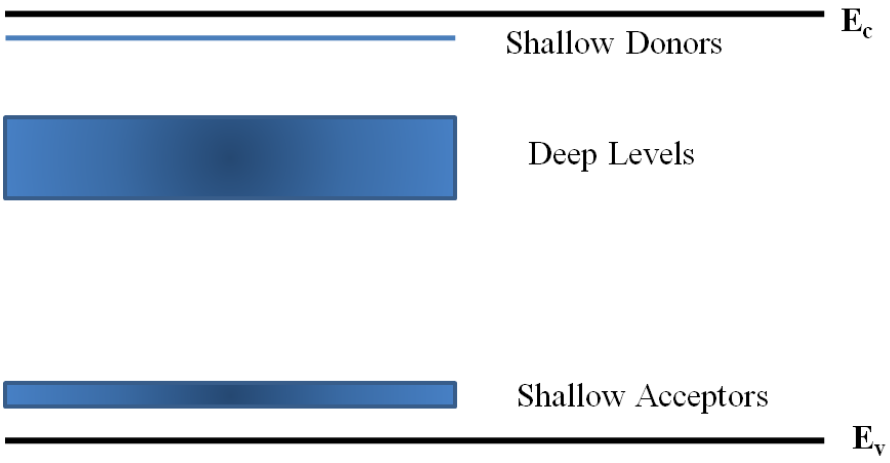

Figure 1.2: Defect states within the band gap

Recent advances in crystal growth have propelled ZnO as a semiconductor of choice over more established semiconductors due to many technologically promising advantages. It should be noted however that the ubiquitous *n*-type behavior of ZnO is a major limitation hindering it from reaching its full potential in applications. There are significant challenges with a reliable synthesis of a *p*-type phase plus insufficient understanding and control over ZnO's electrical conductivity. As previously mentioned, extended and point defects have a strong influence on the electrical and optical properties of semiconductors such as ZnO. Evidently, certain group of defects, hitherto

undetermined, compensates acceptors and thus causes difficulty in producing a reliably *p*-type ZnO [11]. It must be noted that defects may also act as nonradiative recombination centers and degrade the light emission efficiency [12]. Moreover, a reliable room temperature dilute ferromagnetism in ZnO, despite numerous attempts, remains largely unanswered primarily because of some intrinsic defects [11]. Thereby, defect properties of ZnO are the object of vigorous and comprehensive research.

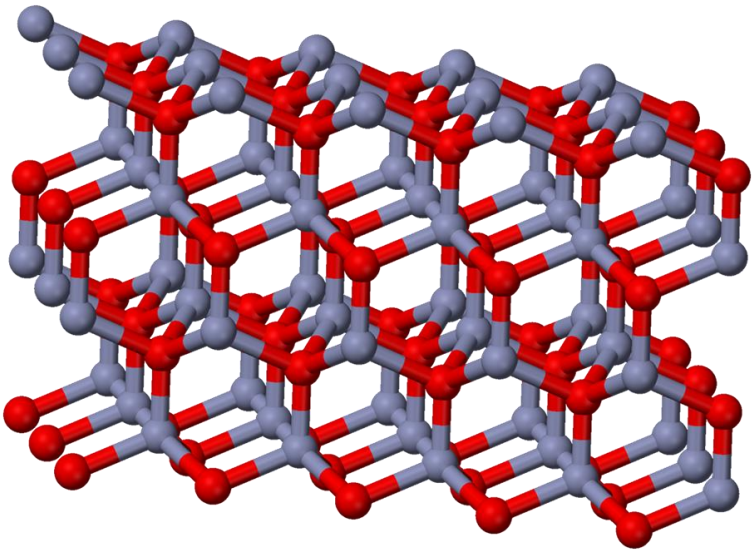

Figure 1.3: Crystal lattice of ZnO (after Ref [5]).

A surface between a substance such as ZnO and vacuum or gas is commonly referred to as a 'free surface' [13]. Conversely, a solid interface is usually defined as a small number of atomic layers that separate two solids in intimate contact with one another [13]. The surface is a disruption of a crystal lattice and may be considered as effectively the largest defect of the lattice. Condition of the semiconductor surface affects numerous macroscopic properties [14]. Since the periodic structure terminates at

the surface/interface, localized electronic states are formed there due to extended and point defects associated with dangling bonds, nonuniform and irregular surface reconstruction or relaxation, chemisorbed impurity atoms, etc. Importantly, the elevated concentration of these surface defects may extend well below the surface driven by such factors as diffusion, stress, and cation/anion imbalance. For ZnO, many aspects of surface and interface defects are poorly understood.

Nanoscale materials, i.e. the ones with dimensions in the range of 1-500 nm, usually have many optical, electrical and magnetic characteristics different from those displayed by bulk materials [15] and thus provide new technological opportunities and challenges [16]. Nanosize semiconductor materials are generating an increased attention to a wide range of possible applications [17]. Because of the large surface-to-volume ratio in nanocrystals, surface-related effects become amplified, and very often in nanostructured systems the performance of the surface is a key performance-defining factor. Therefore for such specimens the concepts of surface physics become significantly more important and must be taken into account.

ZnO represents a very important class of nanostructured semiconductors with multiple potential optoelectronic, spintronic, and electromechanical applications [18-20]. Nanostructured ZnO is readily available in various controlled geometries, shapes and dimensions [21]. Crystal morphology and quality are crucial for the performance of many ZnO nanosystems. Current understanding of the relationship between the performance parameters of ZnO nanostructures and their defect properties is still largely incomplete. The nature of the surface and sub-surface defect states is still ambiguous and only in a small number of studies in the past few years attempts were made to correlate

properties of these states with the morphology of the nanocrystals themselves on the one hand [22-26] and on the other hand to modify these states in a controllable fashion [27-31]. A nanoscale defective layer has been reported for ZnO in several recent publications. For example, in ZnO tetrapod powders Fisher, *et al.* [18] directly observed an enhanced ~ 2.5 eV deep-defect luminescence at the surface of the legs relative to the bulk, pointing to the high near-surface concentration of deep defects. Furthermore, Mosbacker, *et al.*, [19] reported for single-crystalline ZnO samples a decrease in the relative intensity of the catodoluminescence feature at ~ 2.5 eV with the increase of the electron beam energy, indicating a greater defect density closer to and at the surface of the sample, in agreement with Ref. [18]. The nature of this near-surface defect layer in ZnO is not fully understood, its ubiquity in nanosystems is not confirmed, and methods of controllable manipulation of its properties are not addressed. Therefore, we seek to gain a deeper understanding of the properties of the surface and subsurface defective states in nanoscale ZnO and investigate a correlation with other phenomena. Additionally, we look for obtaining a reliable route to tailor the surface/subsurface properties of ZnO, nanosize ZnO in particular.

To adequately address these issues one needs to employ a combination of suitable surface-sensitive and surface-specific tools. Such set of tools should provide capabilities to probe surface-defect properties as well as surface composition, and should allow to modify characteristics of the surface proper, being able to handle nanoscale samples. In our lab we successfully designed and built an appropriate experimental setup suitable for the studies of semiconductor surfaces based on the *in situ*/*in vacuo* approach, and which incorporates a combination of the surface photovoltage spectroscopy (SPV) for

characterization of the surface optoelectronic properties, the Auger electron spectroscopy (AES) for the composition analysis of the surfaces of interest, as well as the remote plasma (RP) treatment and *in situ* resistive annealing for surface preparation and processing.

The argument in favor of using the ultra high vacuum (UHV) arrangement is that it is crucial to avoid detrimental surface contaminations for the duration of processing and characterization. SPV is a top candidate of a tool to be used for semiconductor surface characterization; it offers outstanding effectiveness in a direct measurement of the surface states. AES is a reliable, cost-effective technique to elucidate the stoichiometry of the surface in a wide range of the periodic table.

RP is useful for controlled manipulation of the surface. Such surface treatments can be employed to clean surfaces of foreign chemisorbed and physisorbed species, for chemical and structural alterations of the surface properties, and for assisted growth applications. Previous studies [19, 32] on a single-crystalline ZnO showed that, for example, oxygen RP treatment might considerably reduce the concentration of defects responsible for green emission (probably, oxygen vacancies) especially within the uppermost nanoscale layer. Also, oxygen plasma was instrumental in removing adsorbate species accumulated on the ZnO surface. It was established, by the same token, that hydrogen RP exposure introduces changes in both electrical and optical properties of ZnO [32]. Importantly, it was reported [32] that in ZnO the penetration depth of the plasma species is of order of tens of nanometers, which is comparable with the thickness of a near-surface defective layer. For the case of nanostructured ZnO, the size of nanocrystals has the same scale as both the plasma penetration depth and the

thickness of the defective layer. Thus, because of this scale compatibility and bearing in mind the demonstrated efficiency of plasma treatments of ZnO surfaces, it is very likely that we may potentially be able to gain substantial advantages and enhancement in manipulating the surface defect-related effects.

In addition to the above stated approach, other complementary defect-sensitive *ex vacuo* methods such as positron annihilation spectroscopy (PAS) and photoluminescence (PL) spectroscopy could be used to investigate defect-related properties in the materials of interest. PL is a popular tool for detecting energetics of luminescent transitions associated with lattice defects, whereas PAS is an efficient technique instrumental in identification of free-volume type defects (such as vacancies) in semiconductors [7-9, 33].

Thereby in this work we employ approaches described above to investigate defect properties in nanoscale ZnO crystals and to develop controllable processing protocols for the studied specimens.

Chapter II. Experimental Setup

In this chapter we examine fundamentals and technical aspects of UHV, as well as processing and characterization techniques used in our work. The capabilities of the system designed and built in our lab will be discussed in details.

II.1 Fundamentals of UHV Processing and Characterization Techniques

II.1.1 UHV Basics

As previously mentioned, to elucidate surface and near-surface properties of nanoscale ZnO, surface-sensitive experiments such as SPV and AES should performed under UHV conditions on atomically clean surfaces. Vacuum conditions better than 10^{-9} Torr are conventionally defined as UHV [34].

Key parameters that influence maintenance of atomically clean surfaces in UHV can be explained in terms of the gas density n, the mean free path λ of the particles in the gas phase, and the incident molecular flux I on the surfaces. The flux I is related to the mean speed of the molecules:

$$v = \sqrt{\frac{8k_BT}{2\pi m}}, \tag{2.1}$$

where k_B is the Boltzmann, T – the absolute temperature, and m – the mass of a molecule.

For the molecular density

$$n = \frac{P}{k_BT}, \tag{2.2}$$

and from the standard kinetic theory formula for the flux per unit area $I = nv/4$ one obtains:

$$I = \frac{P}{\sqrt{2\pi m k_B T}}, \tag{2.3}$$

where P is the pressure.

The mean free path is given by:

$$\lambda = \frac{f}{n\sigma^2}, \tag{2.4}$$

where $f = \frac{1}{\pi\sqrt{2}}$ and σ^2 is the molecular cross section. Then the monolayer arrival time:

$$\tau = \frac{n_0}{I}, \tag{2.5}$$

with n_0 being the number of atoms in a monolayer.

So, the monolayer arrival time can be determined from fundamental parameters. For instance, if we apply these parameters to nitrogen as a model gas species, it is determined that the number of molecules absorbed to the surface from the gas phase in about one hour should not exceed a few percent of a monolayer reiterating the need for the UHV conditions. The molecular density is still relatively high at UHV. Nevertheless, the particles mean free path are such that they exceed the dimensions of our chamber, so that a gas molecule will collide with the wall chambers numerous times before meeting another gas molecule. The average coverage also depends on the sticking coefficient S (the probability that an impinging atom or molecule remains absorbed). For most surfaces, including ZnO, S is considered to be close to unity.

Vacuum level	*Pressure (Torr)*	*Gas Density, n (mol/cm^3)*	*Molecular Incident Rate, I (cm^{-2}s^{-1})*	*Mean Free Path*	*Time/ Monolayer*
Atmosphere	760	2×10^{19}	3×10^{23}	700 Å	3 ns
Low	1	3×10^{16}	4×10^{20}	50 μm	2 μs
Medium	10^{-3}	3×10^{13}	4×10^{17}	5 cm	2 ms
High	10^{-6}	3×10^{10}	4×10^{14}	50 m	2 s
Ultra High	10^{-9}	3×10^{7}	4×10^{11}	50 km	1 hour
Ultra High	10^{-10}	3×10^{6}	4×10^{10}	500 km	7 hour

Table 2.1: Variation of vacuum parameters with pressure.

The table above (Table 2.1) shows characteristics of nitrogen gas at room temperature (T = 293 K) and various pressures. The molecular diameter for N_2 is 3.1 pm. The molecular weight is 28.01 a.u. or 4.65×10^{-26} kg. The sticking coefficient is assumed to be unity. The density of one monatomic layer is defined to be $n_0 = 10^{15}$ cm^{-2}; this value is close to the real values for solid surfaces [34]. Note that 1 Torr = 133 Pa.

II.1.2 Surface Photovoltage Spectroscopy

SPV is a contactless technique for probing changes in the surface voltage due to illumination.

At the free surface of a semiconductor, the periodic structure terminates, and localized electronic states are formed. The surface localized states induce charge transfer between the bulk and surface in order to establish equilibrium between them. The outcome of such charge transfer is a non-neutral near-surface region referred to as the

surface space charge region (SCR) [13]. The incident light induces a change in the near surface potential distribution resulting in charge transfer and/or rearrangement, which is monitored by a Kelvin probe. The Kelvin probe is well suited for measurements of the surface built-in-voltages. The arrangement is such that only the applied bias that discharges the effective capacitance is determined. The Kelvin probe usually consists of a small metallic reference electrode placed within a close proximity to the surface. This vibrating electrode generates a steady state AC current in the capacitor formed between the electrode and the surface of the sample and thus is a measure of the contact potential difference (CPD). CPD is a potential energy drop that is equal to the change in the work function $\Delta\Phi$ of the two surfaces involved. Note that $\Delta\Phi = E_{\text{vacuum}} - E_{\text{Fermi}}$ and the work function difference = $eV_{\text{semiconductor}}$.

When the surface of the sample is illuminated by a monochromatic light of a variable wavelength, the induced photovoltaic effects applied to the capacitor cause changes of the surface voltage V_s, which must be equal to the change in the voltage detectable between the two capacitor terminals. Incident photon energy could result in a super-bandgap or a sub-bandgap process depending on the dominant excited carriers [13].

When the surface is illuminated with a sub-bandgap monochromatic light, a charge exchange occurs between the band edges and the local surface electron states due to the excitation (de-excitation) of trapped carriers. These phostostimulated electron transitions from (into) the surface states affect the electrical charge localized in the surface states Q_{ss} [35]. An analogous change takes place in the net electrical charge in the SCR, Q_{sc}, resulting in a change of the surface barrier height. This ensures that charge neutrality is maintained between the surface and the bulk. For a Schottky-type surface

barrier, $Q_{sc} = - Q_{ss}$ (Fig. 2.1). In the sub-bandgap illumination process, the probability of a band-to-band absorption is essentially zero [13].

In the super-bandgap process, the electric field in the SCR causes excess electrons (holes) to be swept away (towards) from (towards) the surface. This mechanism reduces the density of the surface-trapped electrons, and the band bending is reduced. For the super-bandgap SPV, the probability of band-to-band adsorption is usually orders of magnitude larger than the probability of trap-to-band adsorption [35]. Conversely, in the second super-bandgap illumination process, there is a high possibility of electrons or holes trapped at surface defects.

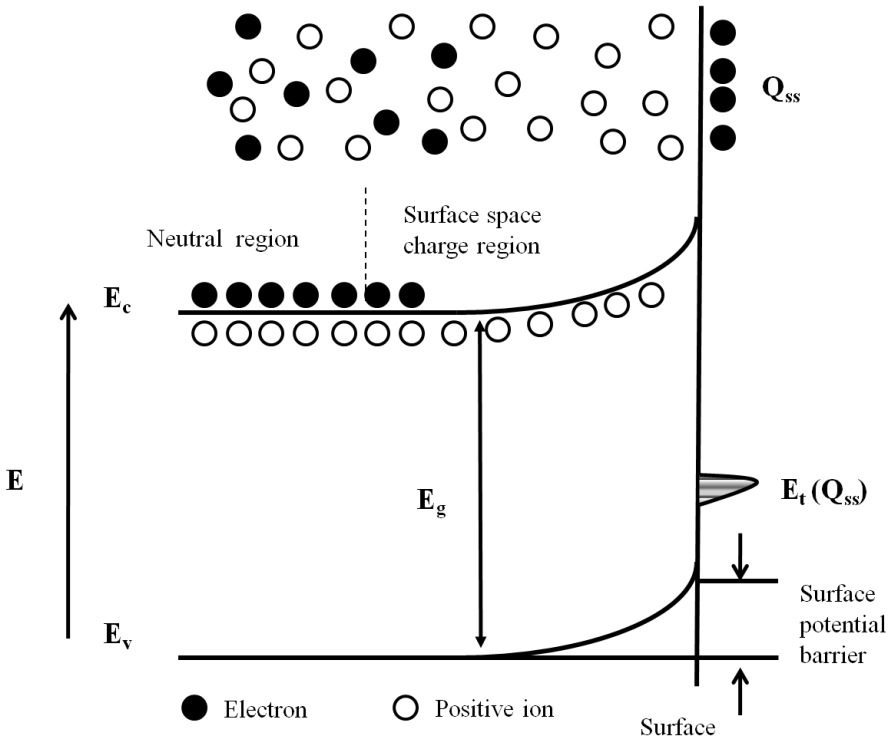

Figure 2.1: Diagram illustrating the effects of surface states on the formation of the space-charge region and the band bending at the semiconductor surface (E_t – energy of the surface trap state; Q_{ss} – net surface charge).

So for an *n*-type semiconductor such as ZnO, with a Schottky type barrier surface, two distinctive sub-bandgap photovoltaic effects may occur. These occur when the energy of the photons is lower than the material's bandgap E_g. First, there is a possibility of an induced electronic transition from a surface state with energy E_t into the conduction band. The energy relationship is as follows: $h\nu \geq E_c - E_t$, where E_c is the minimum conduction band energy (Fig 2.2a). The excited electrons are quickly swept to the conductor bulk under the built-in surface electric field. As a result, Q_{ss} becomes smaller and SCR is less depleted. The gap state depopulation corresponds to a decrease in the band bending from which the SPV signal is obtained. So we have an increase in the surface potential. By the same token, illumination could also result in a population of a gap state situated above the valence band maximum E_v with a photon energy of $h\nu \geq E_t - E_v$ (Fig. 2.2b). The energies of these photons promote electron transitions from the valence band E_v into the trap state with energy E_t. For this transition to occur, the surface states should not be completely filled before excitation. Q_{ss} becomes larger increasing the surface barrier height. This photovoltaic effect corresponds to a decrease in the surface potential and is accompanied by an increase in the band bending. The change in the surface barrier is evident via the CPD measurements obtained as a function of the incident photon energy.

Analysis of the SPV spectra allows one to detect the presence of the surface gap states, determine their energy positions and their band associations by observing changes in the slope of the surface potential versus incident wavelength dependence. Moreover, the type of the semiconductor (*p* or *n*) can be determined by SPV, since the bands of *p*-type (*n*-type) semiconductors are bent downwards (upwards) towards the surface. For a

specific surface trap state with energy E_c, the sum of the threshold energy associated with $E_c - E_t$ (state depopulation) and threshold energy associated with $E_t - E_v$ (state population) is approximately equal to the optical energy gap for a direct transition [35].

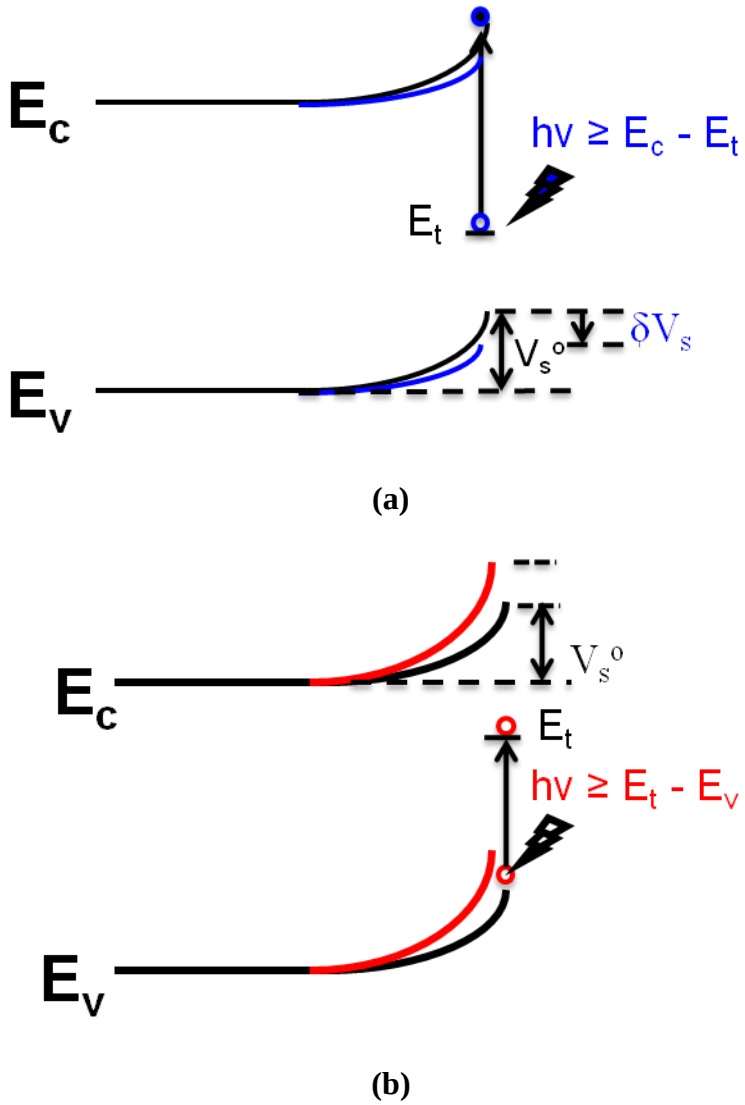

Figure 2.2: Diagram demonstrating the surface photovoltage responses to the trap-to-band/band-to-trap transitions in an *n*-type semiconductor. (a) Surface state depopulation; (b) surface state population.

One advantage of obtaining both transitions from and into a given surface state helps to verify E_t. In addition, such complementary transitions allow us to conveniently

distinguish between transitions related to surface states and other possible bulk transitions.

In addition, SPV can be employed to determine other surface state parameters from the transient dependencies of the phostostimulated depopulation transitions from surface states to the conduction band ($E_c - E_t$) [36]. In the process of obtaining the time transient dependencies, the surface is first illuminated with a monochromatic or white light which begins at $t = t_0$ and when the surface photovoltage saturation is obtained, the illumination is cut at $t = t_1$. Subsequently, the sample is allowed to relax in the dark until equilibrium is achieved. A typical photovoltage transient graph is depicted in Fig. 2.3. Parameters $\dot{V}_s^0$, $\dot{V}_s^1$, V_s^0, V_s^1, and δV_s^0 are defined in the graph.

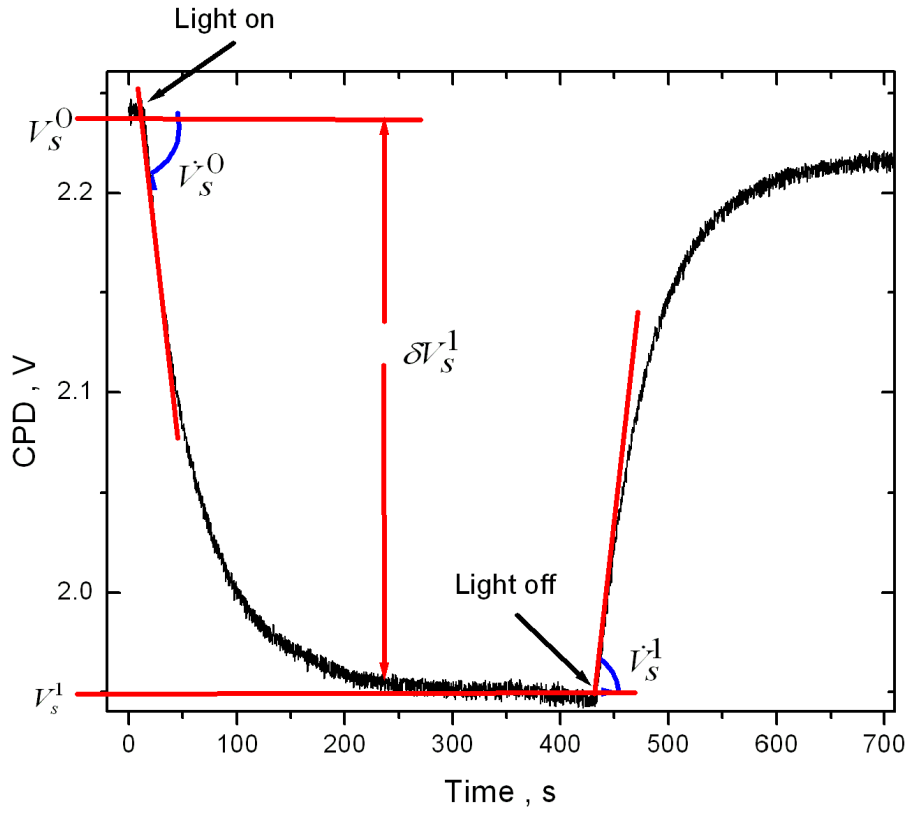

Figure 2.3: Typical surface photovoltage transient behavior.

From a fundamental standpoint, we can use the rate d(CPD)/dt and the total change in CPD to calculate the photoionization cross section K_{ph}, the density of electrons before illumination n_0^t, the density of electrons (holes) after illumination n_t^1 (p_t^1) due to a transition within the bandgap. The rate of change of the density of the occupied states is given by

$$\frac{dn_t}{dt} = -K_{ph}^d n_t I + K_n n_s p_t - K n_t n_1 . \tag{2.6}$$

Here K_{ph}^d is the capture cross section of the surface states for photons (for surface state depopulation); I – light intensity; K_n – capture cross sections of electrons multiplied by thermal velocity: $K_n = k_n v_t$; n_s – density of free electrons at the surface; n_t – density of captured electrons; p_t – density of captured holes; n_1 – emission constant.

The capture cross section for photons during surface state depopulation can be determined as follows:

$$K_{ph}^d = \frac{\dot{V}_s^0 + \dot{V}_s^1}{I \delta V_s^1} . \tag{2.7}$$

The density of the rapped electrons in the dark can be calculated as

$$n_0^t = \frac{\delta V_s^1 \sqrt{2\varepsilon k_B T n_b}}{2q\sqrt{\left|V_s^0\right|}\left(1 + \frac{\dot{V}_s^1}{\dot{V}_s^0}\right)}, \tag{2.8}$$

whereas the density of trapped electrons with illumination is

$$n_t^1 = -n_0^t \frac{\dot{V}_s^1}{\dot{V}_s^0} . \tag{2.9}$$

We could also obtain properties for the trapped holes for illumination. Note that for the $E_t - E_v$ transition corresponding to the phostostimulated population of the surface

states, we simply have to interchange *n* and *p* and reverse voltage signs in the above equations.

SPV is also suitable to determine the relationship between surface electronic structure and surface treatment history (through chemical processing, thermal processing, etc.).

II.1.3 Auger Electron Spectroscopy

Kinetic energy of electrons expelled from a specimen after electron, ion, or photon bombardment can offer surface-specific elemental information [37]. It is based on two factors: (a) the inelastic mean free path of electrons within the energy range of 15 – 1000 eV in most substances is less than 1 nm (depth of detection) and (b) the binding energy of a core electron is sensitive to the atomic individuality. Only electrons within the escape depth of a surface can leave it without losing their energy escaping elastically.

One of the most common electron energy-based elemental characterization techniques is the Auger Electron Spectroscopy. AES probes the composition and chemistry of the specimen's surface and thin sub-surface layers. Among a number of applications of AES one may mention monitoring of surface cleanliness in UHV, thin film growth uniformity, and depth profiling of elemental composition. This surface-sensitive technique measures the energy of electrons emitted from the surface when it is irradiated with X-rays or high-energy electrons in the range greater than 1 keV. AES offers numerous advantages such as surface-specific analysis (typically 0.5 to 5 nm in the vicinity of the surface), fast data acquisition, ability of detecting all elements above helium (atomic numbers $Z = 3$ to $Z = 92$), and a high spatial resolution (limited,

essentially, by the diameter of the incident electron beam). It is also possible to obtain compositional depth profiles when employing a simultaneous ion-induced sputtering of a sample [38].

The AES process involves interaction of electrons with atoms at the surface. Photoelectrons are ejected from the core levels and leave behind vacant states. As a result, atoms in the excited state emit Auger electrons and/or X-ray photons. The energies of the X-rays and photoelectrons are determined by the energy levels of the elements in the sample. Thus, each specimen possesses a distinctive Auger spectrum. The Auger emission of electrons is nonradiative and is described by the following formula:

$$E_{ABC} = E_A(Z) - E_B(Z) - E_C(Z) - \Delta E(B,C) - \Phi. \qquad (2.10)$$

The parameters above are defined as follows: E_{ABC} is the energy of the Auger transition; E_A is the energy of the ionized core level; E_B is the energy of the level from which the electron initiates to fill the core vacancy; E_C is the energy level from which the Auger electron is emitted and Φ is the work function of the specimen. Z is the atomic number of the atom involved. The ΔE term is negligible. It appears since the energy of the final doubly ionized state is to some extent larger than the sum of the energies for individual ionization of the same levels. During bombardment of the specimen, an incident electron with sufficient energy removes a core electron from the *A* level and ionizes the atom. The generated electron vacancy is immediately filled by another electron from the *B* level. The excess energy released, $E = E_A - E_B$, is then transferred to another electron from the *C* level. Consequently, this electron is ejected from the atom as

an Auger electron. This electron must also surmount the work function to escape from the surface.

For example, for a $KL_1L_{2,3}$ transition, $E_{KL1L2,3} = E_K - E_{L1} - E_{L2,3} - \Phi$. The Auger electron in this case originates from the $L_{2,3}$ levels. The electronic energy levels K and L correspond to the 1*s* and 2*s*/2*p* levels respectively. Figure 2.4 below the $KL_1L_{2,3}$ AES process.

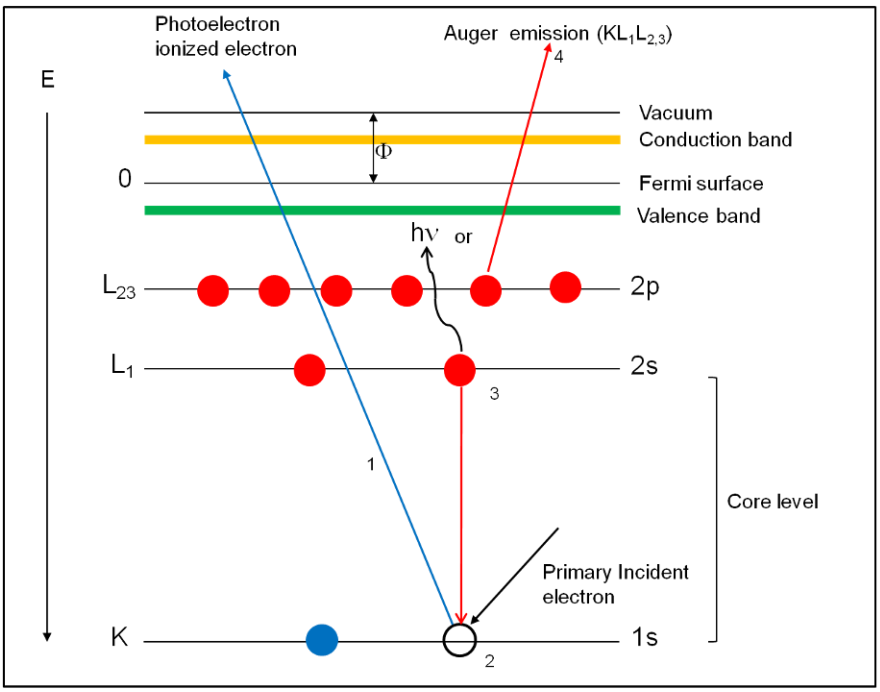

Figure 2.4: Energy level diagram for the Auger process.

There are several other possible groups of Auger transitions such as $KL_1L_{2,3}$, $L_1M_1M_1$, $L_1L_{2,3}M_1$ and L_3VV processes. These nomenclatures indicate the core levels involved in the Auger transitions. So, for the $L_1M_1M_1$ case, the initial vacancy is in L_1 and the two final vacancies are both in the M_1 shell. Similarly, for the $L_1L_2M_1$ transition,

also known as the Coster-Kronig transition, the vacancy is filled by an electron from the same shell. The L_3VV transition process is such that a primary vacancy is formed in the L_3 shell and de-excitation is mediated by an electron from the valence band; this valence band electron transfers its energy to another valence band electron. The L_3VV process occurs when an atom is bound in a solid. The most dominant Auger energy transitions are the KLL transitions for $3 < Z < 14$; the LMM transitions for $14 < Z < 40$, and the MNN transitions for $40 < Z < 82$ [39]. Probabilities of these transitions depend on the energy of the primary electron beam. However, the Auger electron energies are independent of the incident beam energy.

A typical AES setup consists of an electron gun, electron energy analyzer and data processing electronics. The electron gun produces a primary electron beam within a typical energy range of 2 to 5 keV. The electron beam is usually focused with a spot diameter controlled by the beam energy, the beam current, and the electron optics. The most common designs for the electron energy analyzer are cylindrical, hemispherical, and four grid [40].

Auger electrons spectral contributions appear as relatively small peaks in the total energy distribution function, $N(E)$, with a major broad background contribution from scattered and secondary electrons. The visibility of the Auger peaks against the background can be significantly improved by recording or analyzing the spectra in a derivative mode $dN(E)/dE$. It must be reiterated that since AES is a surface-sensitive technique, the specimen should be analyzed in UHV. Figure 2.5 shows the schematics of a typical AES experimental arrangement.

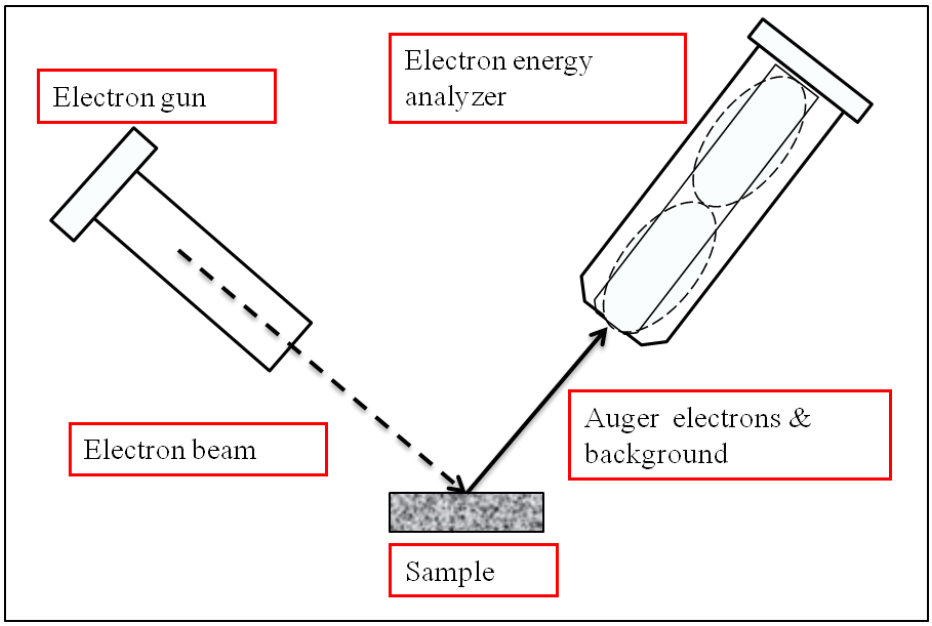

Figure 2.5: AES setup geometry.

As mentioned previously, the Auger electrons have well-defined energies unique to the nature of the atom-emitter; thus, elemental identification is possible based on the energy positions of the Auger peaks. Auger spectra can also provide information on the chemical bonding states of the atoms related to the change in electron binding energy and thus redistribution of the electron density states in the valence band. This could be observed through changes in the peak positions and peak shapes. It must be noted though that quantitative interpretation is not straightforward since three electrons are involved in the Auger process.

AES surface analysis proved to be effective and is widely employed to measure surface composition, effects of surface cleaning, etc. for various ZnO specimens [41].

II.1.4 Fundamentals of Remote Plasma and Its Applications for Surface Processing

Plasma is typically an ionized gas. Plasma occurs naturally and by man-made technological means. It occurs via energy added to a gas and is considered to be the fourth state of matter. Plasma contains charged and neutral species, including some or all of the various constituents, namely electrons, positive ions, negative ions, atoms and molecules [42]. Plasma is commonly electrically neutral – the density of electrons and negative ions equals the density of positive ions since the electric field eliminates charge imbalances. Plasmas may have different degrees of ionization when a fraction of the original neutral species, which have become ionized, is much less than unity (near unity) are weakly (fully) ionized.

An ideal plasma considered to be quasi neutral is an ionized gas with negative and positive charges in approximately equal numbers. However, there are exceptions for which a deviation from this neutrality occurs in a relatively small plasma region while preserving the overall intrinsic plasma identity. A characteristic size of such a region is known as the Debye length λ_D, within which a significant charge separation occurs. The magnitude of the Debye length in plasma it is given by [42]:

$$\lambda_D = \sqrt{\frac{\varepsilon_0 k T_e}{n_e q_e^2}} \tag{2.11}$$

Here T_e is the temperature of the plasma electrons, n_e is the plasma density, q_e is the elementary charge, ε_0 is the permittivity of free space, and k_B is the Boltzmann constant. So, in the event of internal or external factors causing deviation from charge neutrality such as an introduction of an extra charge, a Debye sphere forms that essentially shields

such charge neutrality perturbation (Figure 2.6). This shielding can occur only if enough particles are present in the charge neutralizing "cloud". Importantly, the Debye length must be much smaller than the characteristic dimensions of the plasma generating hardware.

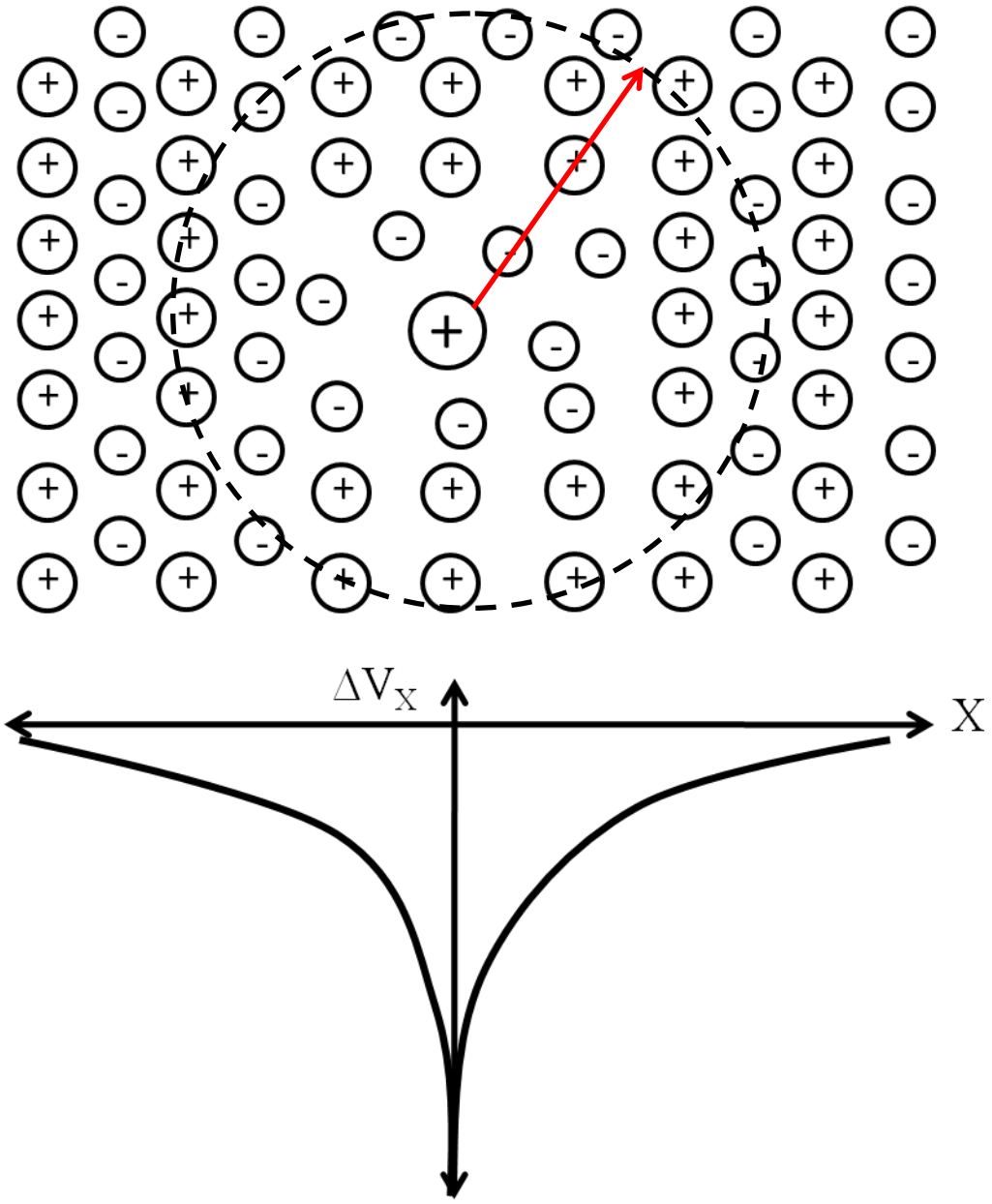

Figure 2.6: Formation of the Debye sphere through which the mobile charge carriers screen out the electric field due to the introduction of an extra charge.

Plasmas are generated through various means: direct power and alternating power (microwave, radio frequency (RF), medium frequency, low frequency) [43]. There is nonetheless a common generation scheme:

Power Supply → **Electric Field** (electrons accelerated) → **Gas** (ionization, excitation) →**Plasma**

In our lab we use RF-generated plasmas. In the process of the RF breakdown, the ac electromagnetic field supplies enough energy to the electrons to initiate ionization. The RF power can be coupled capacitively or inductively. Inductively coupled plasma (ICP) is a type plasma source in which the energy is due to electrical currents produced by electromagnetic induction (time-varying magnetic fields). During the ICP process, a time-varying electric current is passed through the coil (usually copper). A time varying magnetic field around the coil is created; hence, it induces azimuthally flowing electric currents in the gas leading to a breakdown and formation of plasma. A capacitively coupled plasma (CCP) generator consists of two metal electrodes separated by a few cm, placed inside (outside) a reactor. The plasma is generated between the two electrodes by means of RF power.

It is crucial that the rate of ionization balances the losses due to diffusion to the walls, volume recombination, electron attachment, and other factors. Diffusion loss is considered to be the dominating factor in a usual plasma process. Before breakdown there is a homogeneous neutral gas accompanied by a constant electric field and a linear voltage drop. The first state after breakdown is a glow discharge.

Remote plasma discharge in our system is obtained from direct plasma generated in the Pyrex glass tube component. The plasma is pulled downstream by applying an electric field to some electrode located in the plasma chamber. An important advantage of remote plasma is its much lower temperature compared to direct plasma providing independent control of temperature and pressure of the surface of the solid. RP can be used to clean semiconductor surfaces of foreign chemisorbed and physisorbed species, and to chemically alter surface properties through structural changes and removal of native defects. RP can be also used in assisted growth applications such as plasma enhanced chemical vapor deposition (PECVD).

Bearing in mind a demonstrated efficiency of plasma treatment of ZnO surfaces and the fact that the surface defect layers and the plasma penetration depth have the same scale, through RP surface processing we may be able to gain substantial advantages in manipulating the properties of surface/near surface defects.

II.2 Functionalities of the UHV Chambers

II.2.1. General Description

The implementation of surface-sensitive studies requires UHV instrumentation to allow for a well defined preparation of the studied samples and to provide means to keep the surface clean for prolonged periods of time. In our lab we designed and built a UHV system to perform surface-specific studies and to controllably manipulate surface and sub-surface properties. The setup consists of three main compartments: a load lock (LL) chamber, a preparation chamber, and a characterization chamber. Figure 2.7 outlines key elements of the system, which is designed and built using vacuum compatible materials

such as 304 stainless steel, ceramics, glass, copper, aluminum and other low vapor pressure materials operating at typical temperatures of a vacuum system. The interconnected chambers are equipped to perform multiple tasks employing processing equipments, service components, surface analysis facilities and designed support structures. All UHV connections are made using standard knife edged ConFlat flanges (CFF), which establish seals using copper gaskets. On the other hand, components not under UHV but a part of the system such as backing pump connection to a turbomolecular pump (TMP) and gas lines are connected using viton or Swagelok seals. Since no single pump can achieve UHV conditions from the atmospheric pressure by itself, a combination of several pumps is selected to achieve and maintain vacuum in the chamber accompanied by valves and pressure gauges. These gauges cover different pressure ranges. The thermocouple gauges (TC) measure pressures in the $10 - 10^{-3}$-mTorr range. The ion gauges measure pressures below 10^{-4} Torr.

Pumping of our UHV facility is outlined in Figure 2.8. To evacuate the system from atmospheric pressure, a rotary oil pump (Welch Duo Seal Vacuum) is used to rough the system and act as a backup for the TMP (Varian TV301 Navigator), attached to the preparation chamber. The TMP has a maximum speed of 56000 rpm and "shuffles" gas molecules from UHV to the backing side where molecules are removed by the rotary oil pump. The TMP allows remote control of temperature and speed. An ion pump (Varian VacIon Pump) is connected to the characterization chamber. It has no moving parts and is used to maintain UHV in the characterization chamber. This pump is equipped with permanent magnets and operates at a high voltage. Inside, helical movement of electrons generates ionization of gas molecules, which are either captured or chemisorbed. The ion

pump control has the capability of providing pressure readings from 10^{-4} down to 10^{-9} Torr. This is essentially the pressure in the ion pump.

The LL and preparation chambers can be evacuated independently of the characterization chamber. An initial vacuum of about 10^{-3} Torr is established using the rotary pump. During this period the pressure is monitored with a TC gauge. The system is then pumped with a TMP. Once lower pressure is achieved, it is monitored using ionization gauges. The characterization chamber is interconnected with the preparation chamber. The evacuation process of the system includes an independent operation of the

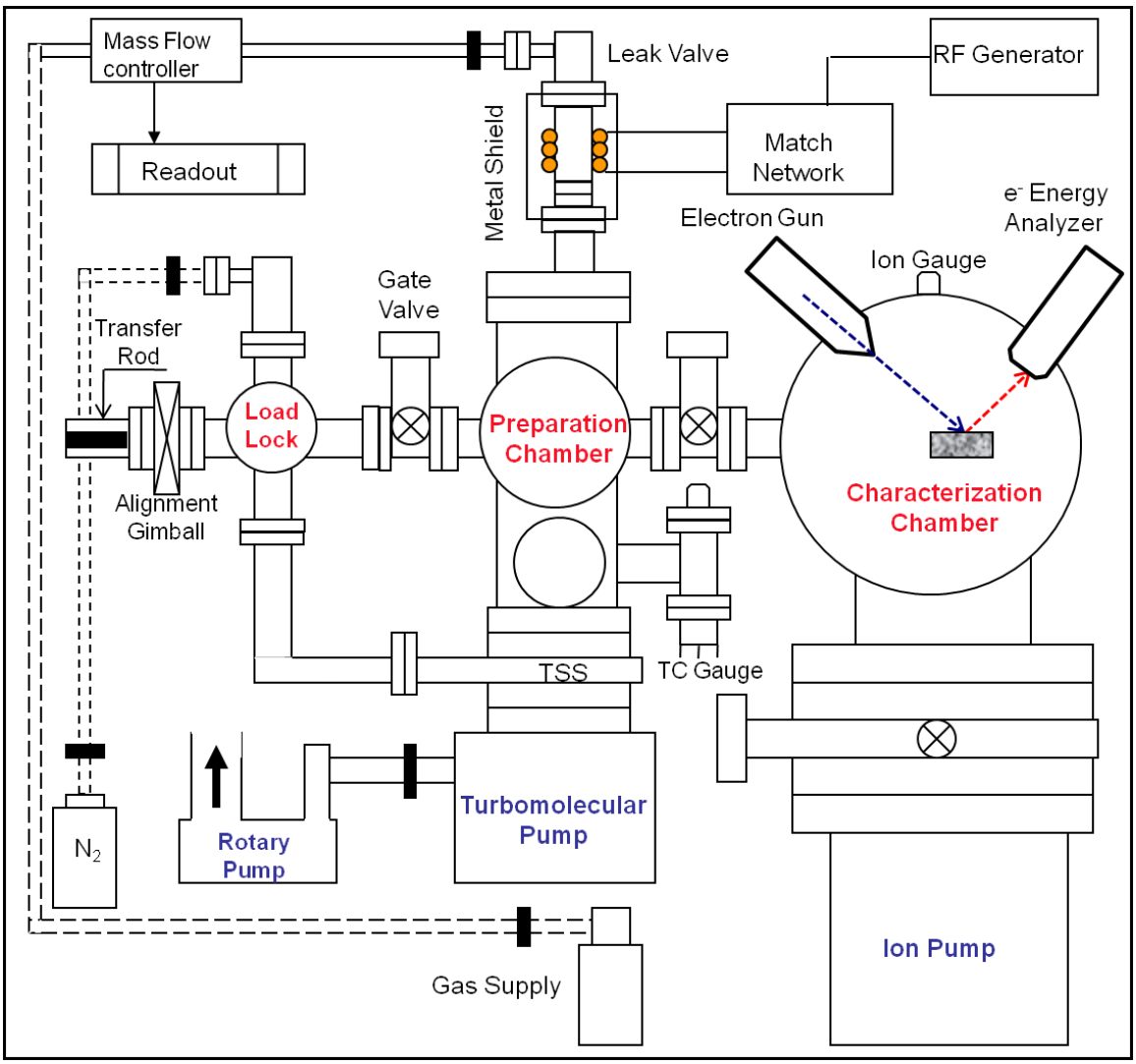

Figure 2.7: Schematics diagram of our UHV system.

ion pump. Pressure is monitored over time to detect significant leaks. Such leaks are distinguishable from outgassing of the chamber walls since the pressure rise associated with the leak is linear over time whereas outgassing tends to saturate.

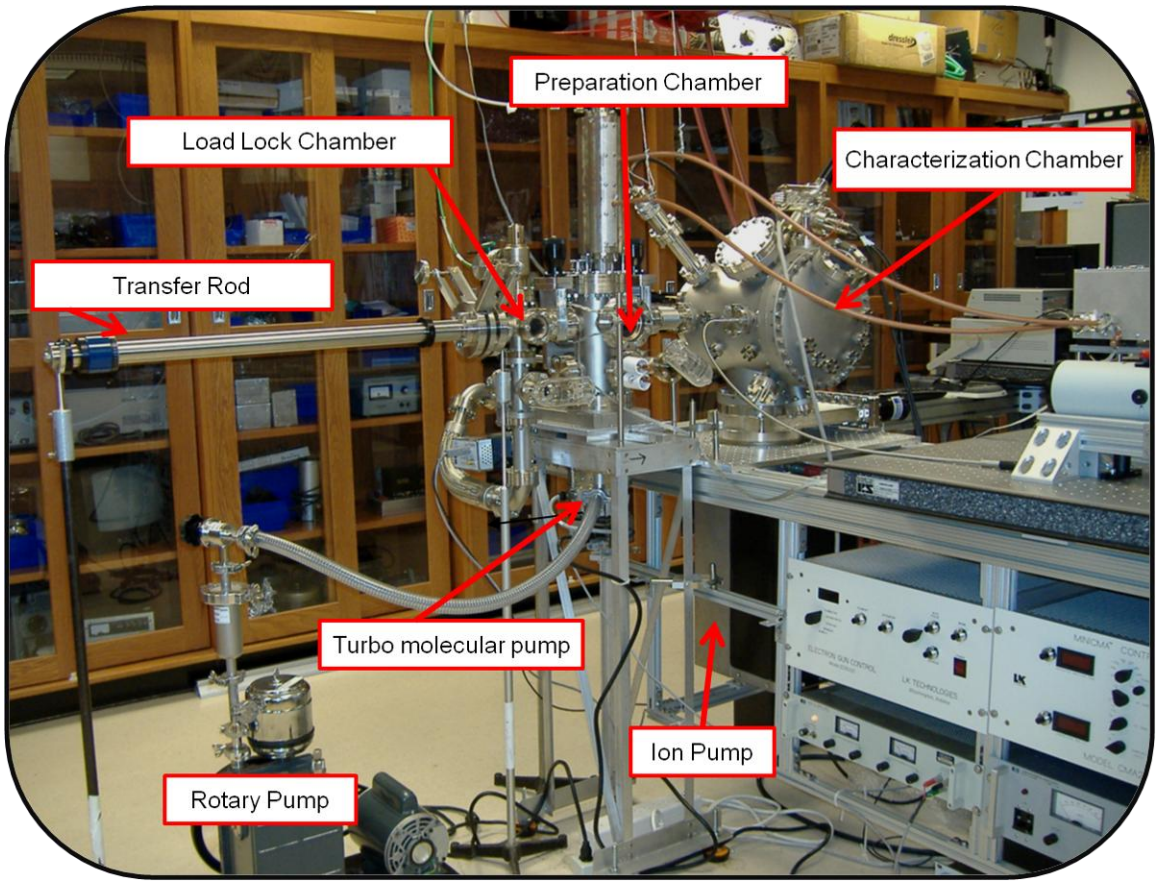

Figure 2.8: Overview of the UHV multi-chamber system.

II.2.2. Load Lock Chamber

In our UHV setup, the loading facilities are accompanied by transfer mechanisms. A quick access door is mounted at a convenient port of the LL system. A home-built sample holder enters the system via this door. A transfer facility aligned with the entire system is also attached to the LL chamber and provides contamination-free transport between the different UHV chambers via a magnetically coupled transfer rod. The sample holder enters the system via this door and it easily screws into the transfer rod. One can easily mount a variety of different samples depending on the requirements of

experiments. For instance, flat UHV compatible plates could be attached in tandem with sample attached to vacuum compatible conductive carbon tape.

The 6-way cross compartment of the LL chamber can be isolated from the rest of the system using a manually operated gate valve, which connects the LL chamber to the preparation chamber and a remotely controlled throttling SoftShut gate valve (TSS). This valve is connected to the bottom port of the sample preparation chamber and is accompanied by a 2.75" CFF gate valve that establishes a connection to the LL chamber. The TMP only pumps the loading facilities when the 2.75" CFF gate valve is at close position.

Additionally, the LL chamber has an evacuated gas inlet system connected to the UHV chamber through a leak valve. This gas supply mechanism is connected to the LL chamber to vent the system using dry nitrogen gas. This provision protects the chamber walls from contamination with water and foreign species when the door of the system is opened. In this procedure, the rotary pump valve is closed and the TMP is turned off. When the pressure in the LL chamber is low enough, dry nitrogen gas is supplied equalizing the internal pressure with the outside pressure. Once the pressure exceeds equilibrium, the access door pops open. During the loading (unloading) of samples the LL chamber can be isolated from the rest of the system due to the feature of the TSS valve mentioned previously. UHV can be maintained in the preparation chamber and characterization chamber using an ion pump during this isolation stage.

II.2.3 Preparation Chamber: Annealing and Plasma Generation

The preparation chamber is equipped with a home-built stage that translates by means of an XYZ manipulator. The stage can also be rotated around the *z*-axis by means

of the rotary feedthrough. The two electrical terminals of the stage are insulated by ceramic standoffs. When the sample holder is fitted into the stage, the sample can be annealed via resistive (I^2R) heating as schematically depicted in Figure 2.9. Thin tantalum plate along with sample clips mounted on the sample holder is employed for resistive heating. Electrical connections between isolated terminals are established through the tantalum foil. Figure 2.10 shows the stage and the sample holder located in the preparation chamber. An electrical feedthrough is attached to the chamber. The insulated flexible copper braided connections are set up between the stage and the feedthrough to provide flexible maneuvering of the stage during processing (see Fig. 2.10).

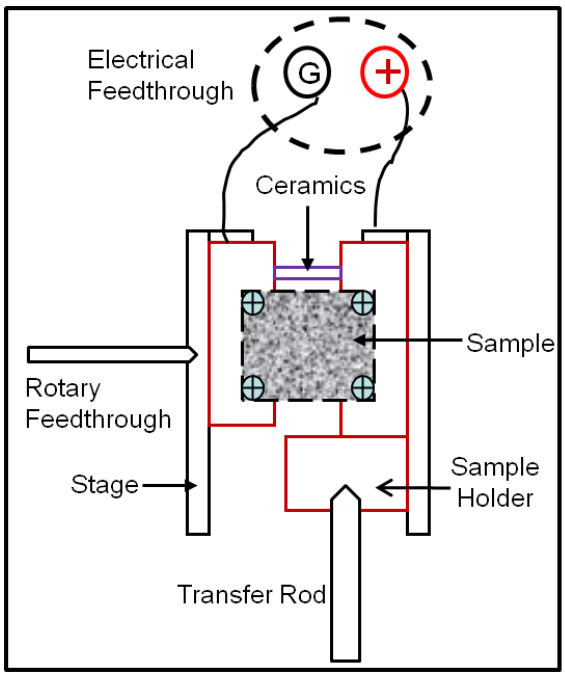

Figure 2.9: Diagram of the resistive heating setup.

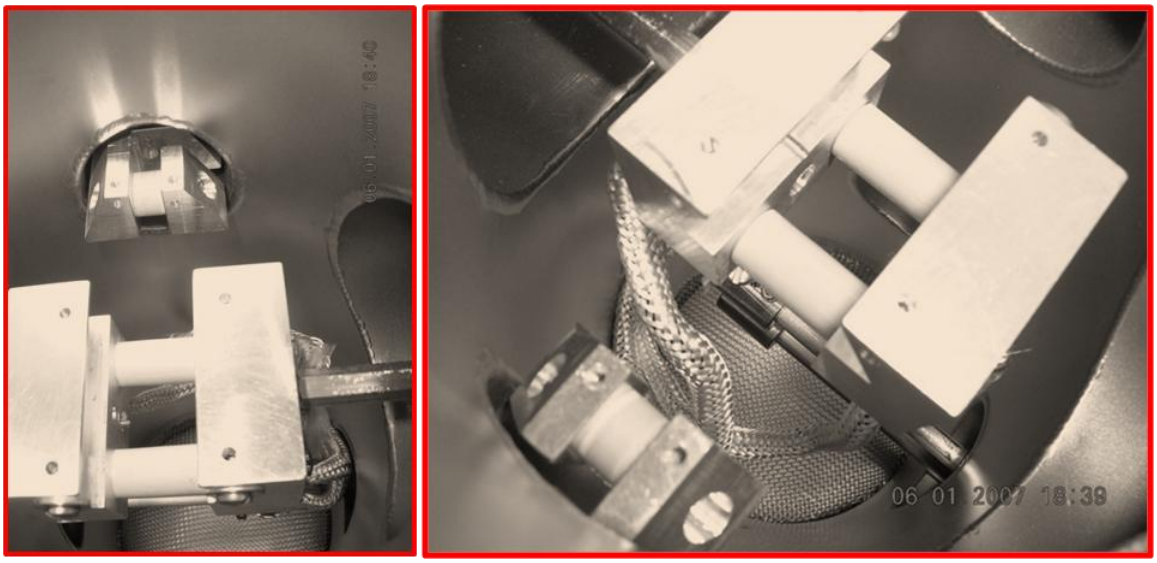

Figure 2.10: Sample stage and sample holder inside the preparation chamber.

The preparation chamber is also designed to generate direct and remote plasma (Fig 2.11). Direct plasma is generated in a Pyrex glass tube located on top of the preparation chamber. On the other hand, remote plasma is produced inside the chamber proper. Generated plasmas are initiated and sustained by electromagnetic fields that are produced by an AC power supply. The frequency of excitation is 13.56 MHz (the RF range of the electromagnetic wave spectrum). The power supply is designed for a 50 Ω impedance load for maximum delivery of power. Since the discharge system may have a different impendence, an impedance-matching network is placed between the power supply and the discharge system. The match network consists of a shunt capacitor and a series capacitor and inductors (LRC network). Here, one reactance is parallel to the load (load capacitor) and the other (variable capacitor connected in series with a fixed inductor) is in series with the source. The match network is used to maximize the power into the load, or minimize the amount of power reflected back from the cable into the source. This minimizes formation of reflected waves, which could set up standing wave

resulting in power loss in the cable connecting the coil and match network. The match network also serves to protect the RF generator from unstable load conditions. An induction coil of a few turns is wound around the glass tube to create an oscillating magnetic field which sets up an oscillating current in the ions and electrons of the supplied gas. The system is optimized to successfully obtain these conditions required to create plasma.

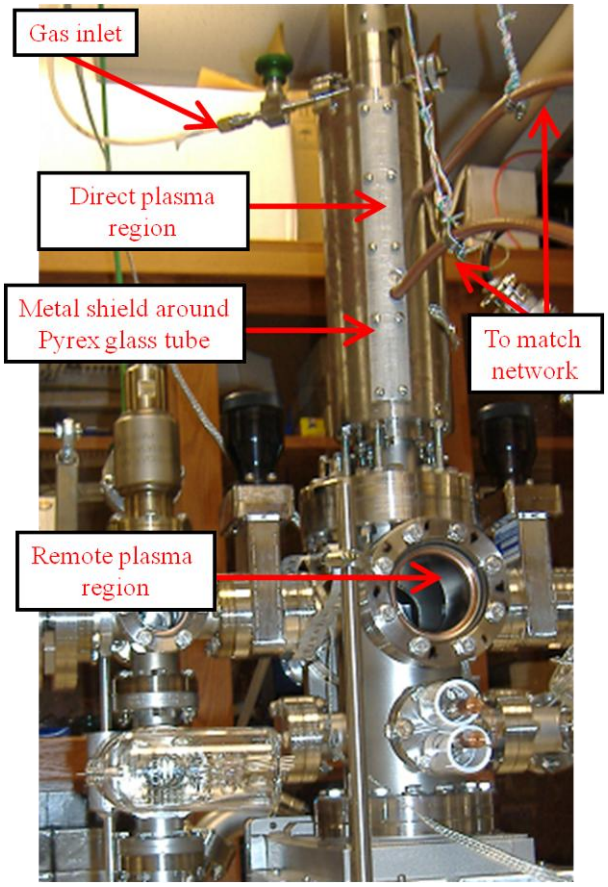

Figure 2.11: Remote plasma system

The gas is supplied to the direct plasma region using a leak valve. The gas flow rate from a gas bottle is controlled and monitored with a 200 sccm MKS flow controller

(type 1179A) in tandem with readout. Plasma generation and optimization is a multi-step preparation routine, which is initiated by pressure regulation (operating the TMP to its lowest frequency of 187 Hz), automatic adjustment of the position of the TSS valve between the chamber and the turbo pump, and supplying a few sccm of the gas to be ionized, with an application of the RF power. The parameters are optimized until a resonance is achieved.

Resonance in the circuit could not be established within the set-up with a copper wire coil. Most of the power was reflected back due to a mismatch between the source impedance and the load impedance. Other parameters involving the match network such as the load capacitor settings were varied automatically and manually. However, RP was successfully generated using the Tesla coil. This result indicted that the gas parameters established were adequate for plasma generation. The suggestion followed to make adjustments within the RLC circuit.

After several trials, a 0.25" copper tubing (as shown in Fig. 2.12) was implemen-

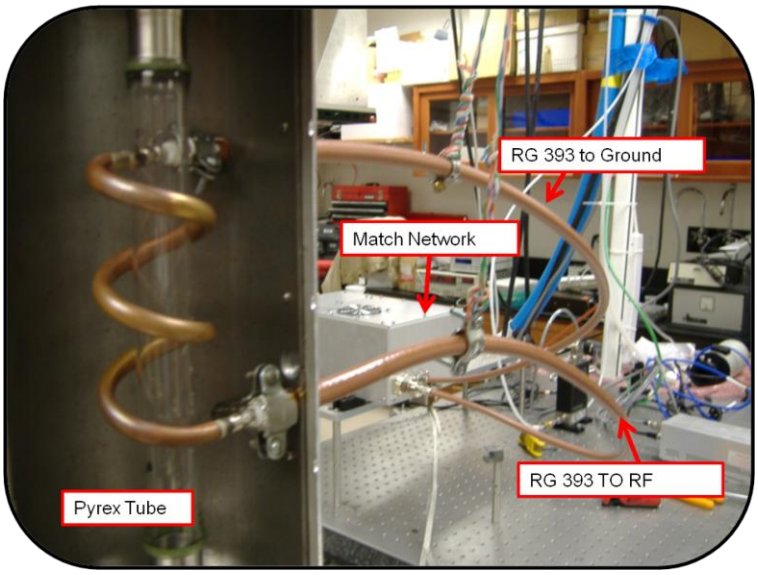

Figure 2.12: RF inductive coupling employing copper tubing and RG393 cable.

ted for the coil. The cables between the coil and match were also replaced with RF 393 coaxial cables, approximately 3" in length. A number of advantages are derived using the RG 393 cable. Its center conductor is Teflon-insulated and thus has a high thermal immunity. This cable can run up to of 200°C without any damage and has a high voltage tolerance. The Teflon insulator provides a better insulation between the wiring and the shield. Ground connections between the cable shield and the wall of the shield cylinder are shown in Figure 2.13.

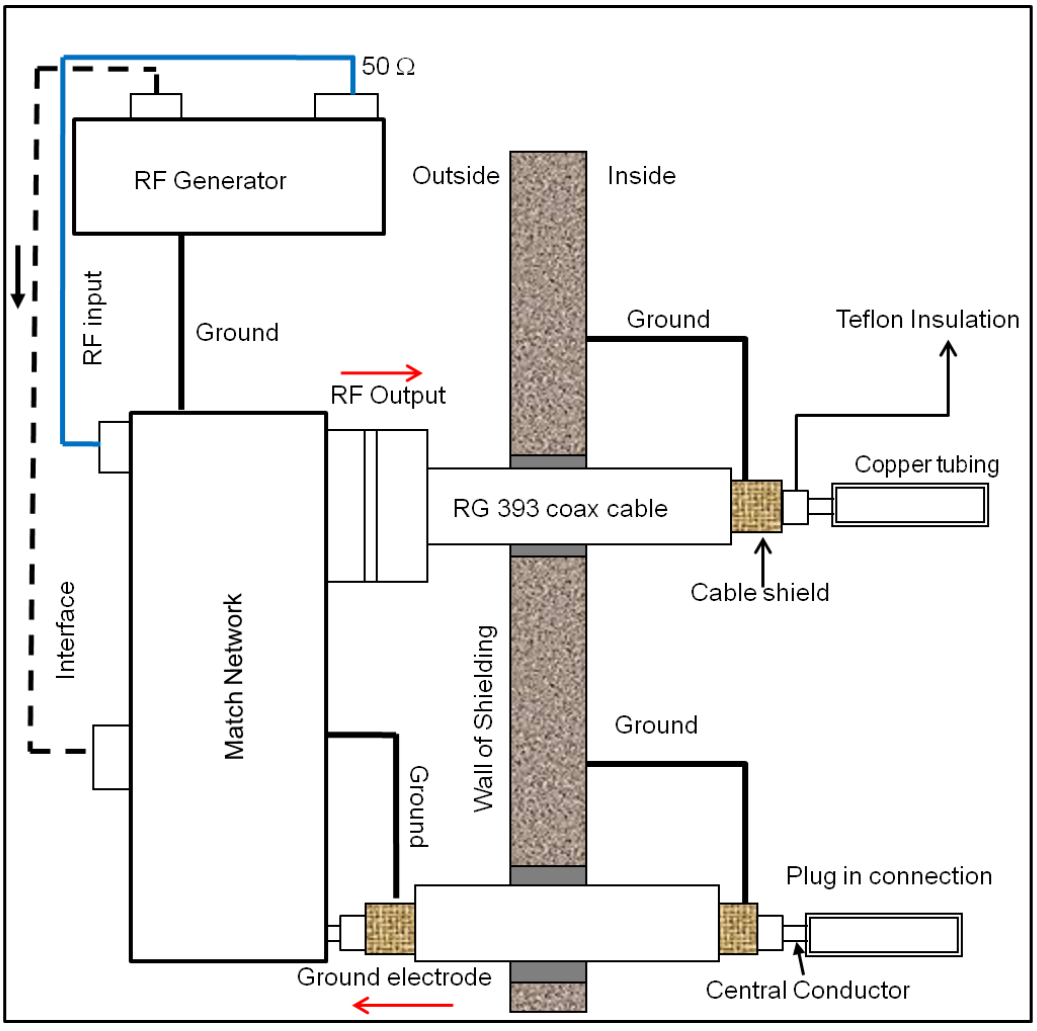

Figure 2.13: Schematic diagram of the electrical components for the plasma setup.

Such changes in setup yielded direct plasma as shown in Figure 2.14. Almost all of the power was forwarded to the load. Moreover, there was no longer a need for ignition using the Tesla coil as the plasma was ignited and maintained via RF excitation alone. However, pressure optimization did not yield remote (cold) plasma in the chamber. To correct that, excited species were extracted from the tube by applying an electric field using the electrically isolated stage. By the same token, an independently installed wire mesh was employed as an electrode in the system. This allowed for annealing in tandem with plasma treatment of the sample. Figure 2.15 shows remote nitrogen plasma as seen through a viewport window. We also successfully generated hydrogen and oxygen/helium plasmas (Figure 2.16)

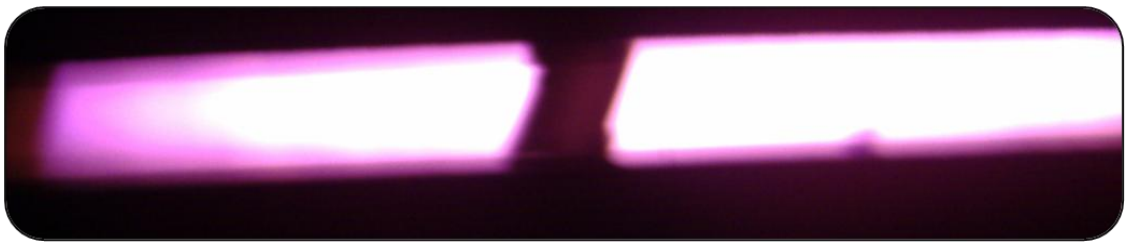

Figure 2.14: Direct nitrogen plasma.

In order to be able to create plasma of a preset mix of gases, we expanded the capabilities of our plasma generating setup. An additional 200 sccm MKS gas flow rate controller (type 1479A) was installed in the set such that specific flow rates of two gases (e.g., O_2 and He) to a common junction point (T-like configuration) to create gas mixture, which eventually flows to the remote plasma generating region. Plasma generation and optimization was employed using previously mentioned routines for various gas mixtures and their ratios.

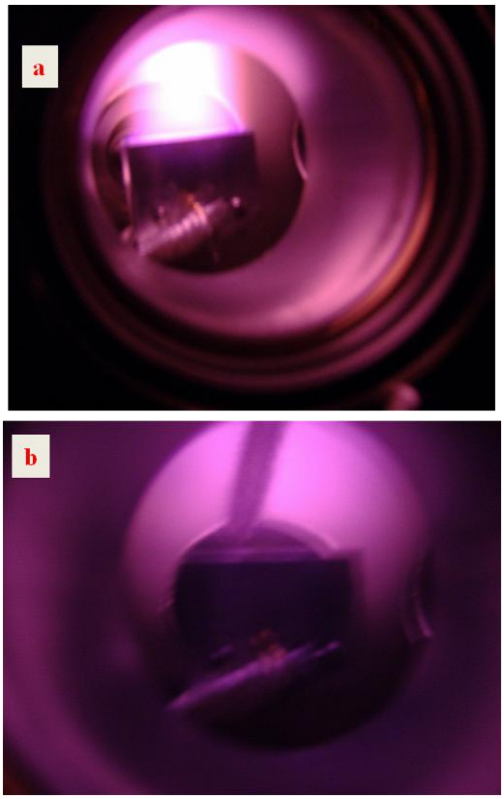

Figure 2.15: Remote nitrogen plasma generated by the bias on (a) the sample stage; (b) mesh electrode.

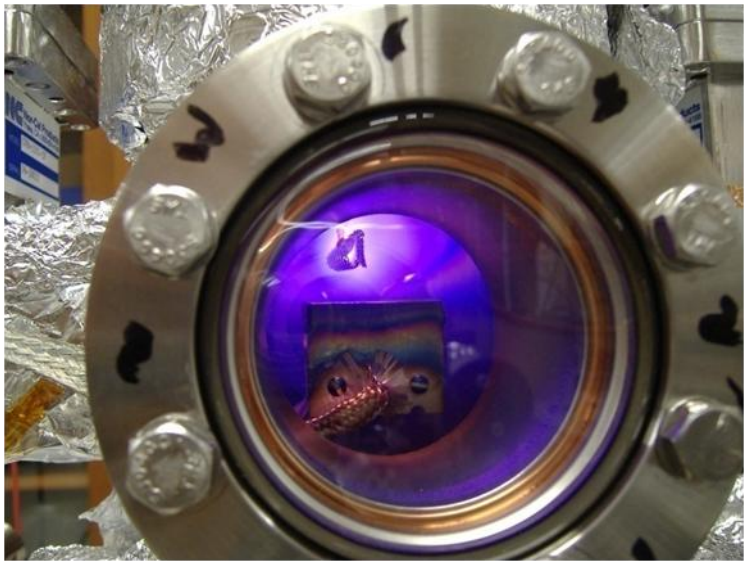

Figure 2.16: Remote oxygen/helium plasma.

II.2.4 Characterization Chamber

The preparation chamber can be isolated from the characterization chamber by means of a manually operated gate valve. An ion pump separated by a gate valve is mounted to a bottom flange of the characterization chamber. This chamber is dedicated to surface analysis. To run AES, it is equipped with an LK EG300 electron gun (EG) to irradiate the samples and a 4″-retractable LK CMA 2000 cylindrical mirror analyzer (CMA) to characterize the energy of the emitted secondary electrons. The EG and CMA are mounted at 90° with respect to each other (Figure 2.17).

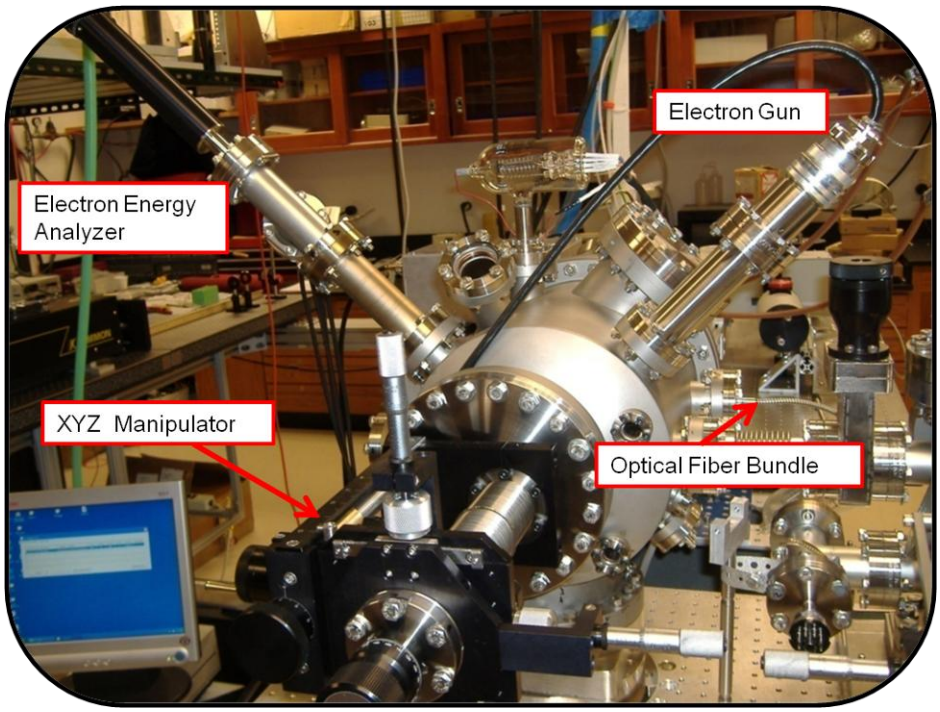

Figure 2.17: Exterior of the characterization chamber.

This characterization chamber is also designed to perform SPV analysis. A home-built Kelvin probe/fiber bundle holder is provided to accommodate the Kelvin

probe in tandem with an optical fiber, which remotely provides light via a fiber bundle vacuum feedthrough. The surface of a sample is illuminated by a monochromatic light of a varying wavelength generated *ex vacuo* by an external light source, a monochromator and an F# matcher. The Kelvin probe is a small metallic vibrating reference electrode that can be placed within a close proximity of the surface of the sample via an XYZ manipulator to measure the CPD. Figure 2.18 shows the instrumentation and fixtures provided inside the chamber.

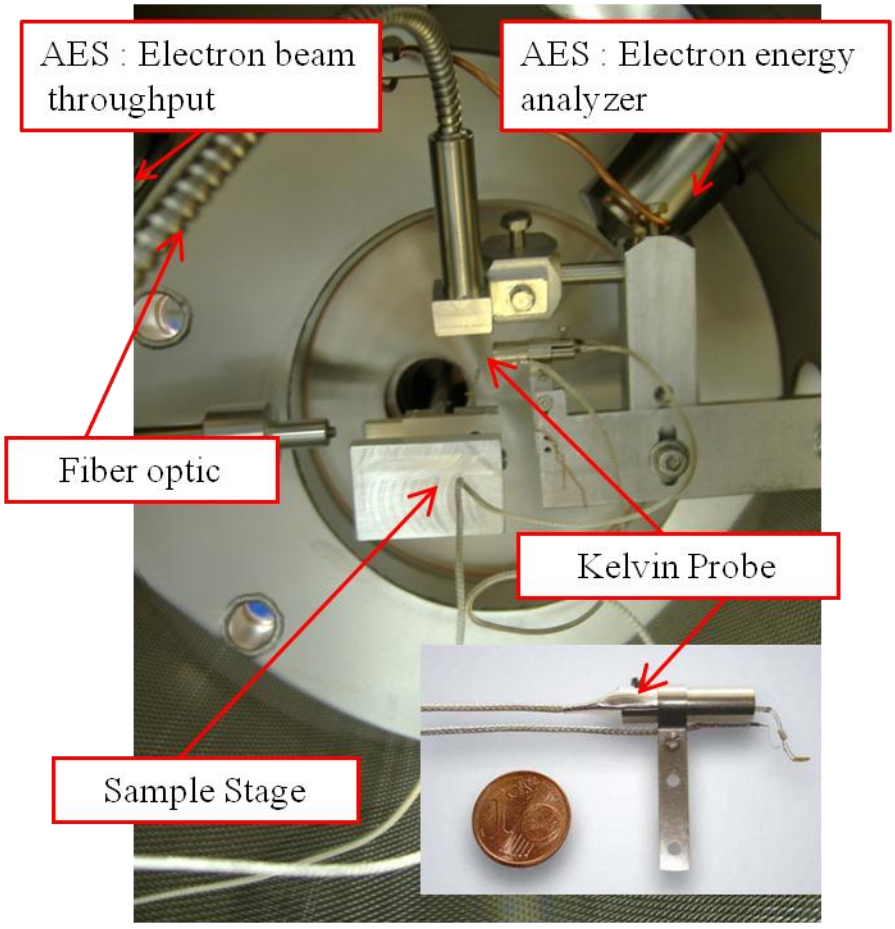

Figure 2.18: Interior view of the characterization chamber.

To the best of our knowledge the described experimental setup is unique – *in vacuo* SPV is operated *in situ* with AES and remote plasma processing.

II.2.5 Discussion of Technical Aspects of SPV

The efficiency of measurements (the signal-to-noise ratio) depends on many factors. The intensity of incident light is one such important aspect. The fiber bundle component of the optical train was used to feed light into the characterization chamber. We installed a feedthrough with a bundle on both sides because the intensity throughput of the bundle is better than that of a single fiber. Our fiber bundle has a transmission range of 160-1200 nm.

A light of a variable frequency with photon energy range 1.13 eV – 3.65 eV, excites the SPV response. The *ex vacuo* part of our optical train consists of a 250 W QTH lamp as a white light source, a pair of fused silica lenses, band-pass filters, and the Oriel Cornerstone grating monochromator with an F/# matcher and a chopper (Fig. 2.19). A LabVIEW program that allows us to conveniently vary the energy ranges, their intervals and vary the time constant does the recordings of SPV spectra. The LabVIEW program controls the wavelength changes through the monochromator and operates the electronics of the Besocke Kelvin Probe S. There are two gratings with wavelengths ranging from 180 to 750 nm and 450 to 2000 nm respectively. For such monochromator gratings, the SPV response may be susceptible to the contribution of the higher order diffraction peaks and stray light [44]. To address this concern, band pass filters are installed in our optical apparatus that block possible higher diffraction interferences, which yield spectral artifacts and decrease energy resolution. Most importantly, the

effects of the vicinity of the bandgap energy are removed since the absorption coefficient drastically increases around this energy. For instance, a band pass filter used in the energy range 1.13 eV to 1.91 eV substantially improved the SPV response in this range for ZnO samples with the removal of apparent second order diffraction features. Additionally, to deal with the artifacts caused by a filter change at particular energies, we carefully juxtapose spectra obtained using different gratings or different filter exchange energies to provide distinction between photon-flux-induced signal variation and real spectral features, as suggested in literature [13,40].

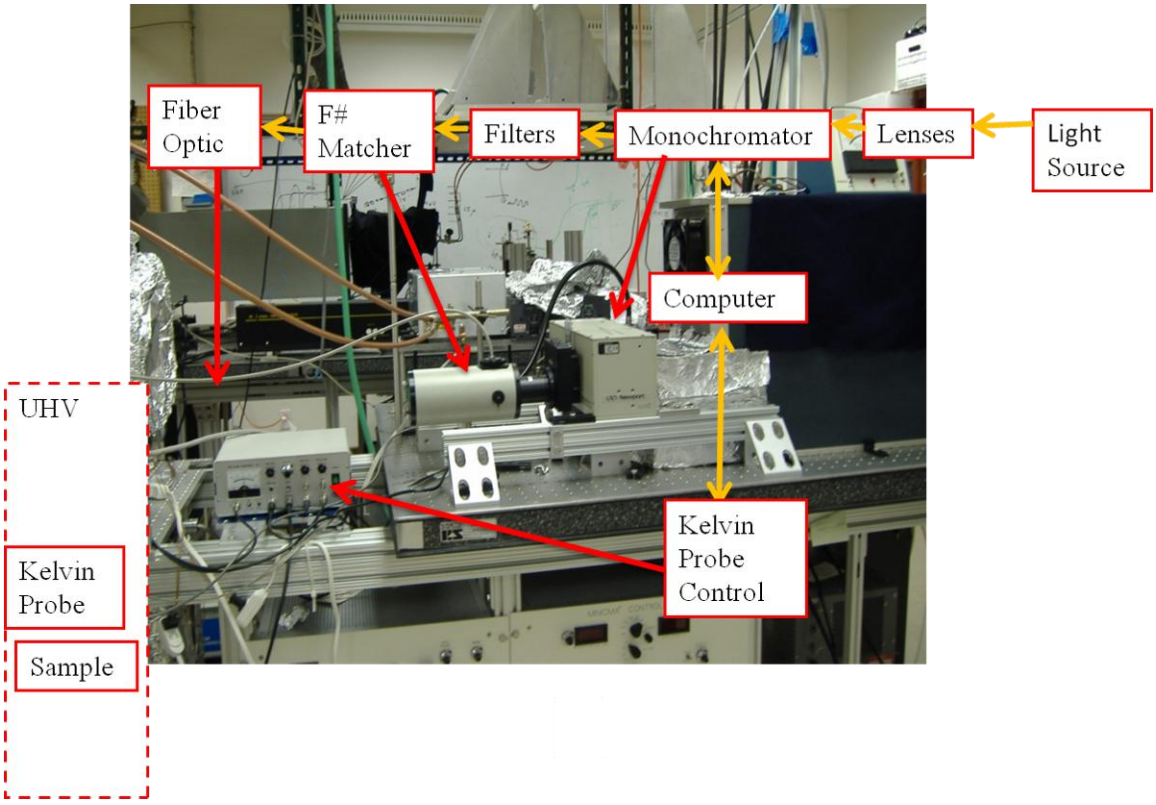

Figure 2.19: SPV illumination system.

Prior to each spectral sequence, transient response curves were obtained. The samples were illuminated directly with white light until the SPV saturation was achieved. Then the experiment continued in the dark until the surface state equilibrium was achieved. The presence of continuously moving parts *in vacuo* poses challenges since we may have to deal with mechanical noises. For the duration of the experiment, the ion pump maintains the vacuum in the system while the TMP and the rotary pump are turned off as the primary contributors of mechanical vibrations of the whole UHV setup. The ion pump has no moving parts, as previously mentioned.

II.3 Positron Annihilation Spectroscopy

Positron annihilation spectroscopy is a useful tool to study defects in semiconductors. It is sensitive to microscopic defects with relatively low concentrations. PAS could probe bulk, subsurface and layered structured properties. It is a non-destructive technique [45] and is widely used in tandem with other techniques.

PAS analysis employs gamma rays resulting from the annihilation of positrons (e^+) and electrons (e^-). Positrons are commonly produced by a nuclear decay. The general sources of positrons for PAS are artificial radioisotopes emitting β^+-radiation. A β^+-decay is given by the following relation:

$$\text{Proton } (p) \rightarrow \text{Neutron } (n) + e^+ + \text{Neutrino } (\nu).$$

For instance, a beta decay of sodium $^{22}Na_{11} \rightarrow {}^{22}Ne_{10} + e^+ + \nu$, is a frequently used decay mechanism used in the PAS lifetime (PAS/LT) studies. ^{22}Na has a half-life of 2.602 years. A fundamental feature of this decay is emission of a 1275 keV γ-photon within 3 ps of emission of a positron. This decay scheme is shown in Figure 2.20. ^{22}Na

disintegrates primarily to the 1275 keV level of ^{22}Ne (90.4 % β^+, 9.5 % electron capture). However, a very small fraction (0.1 %) disintegrates to the ground state of ^{22}Ne.

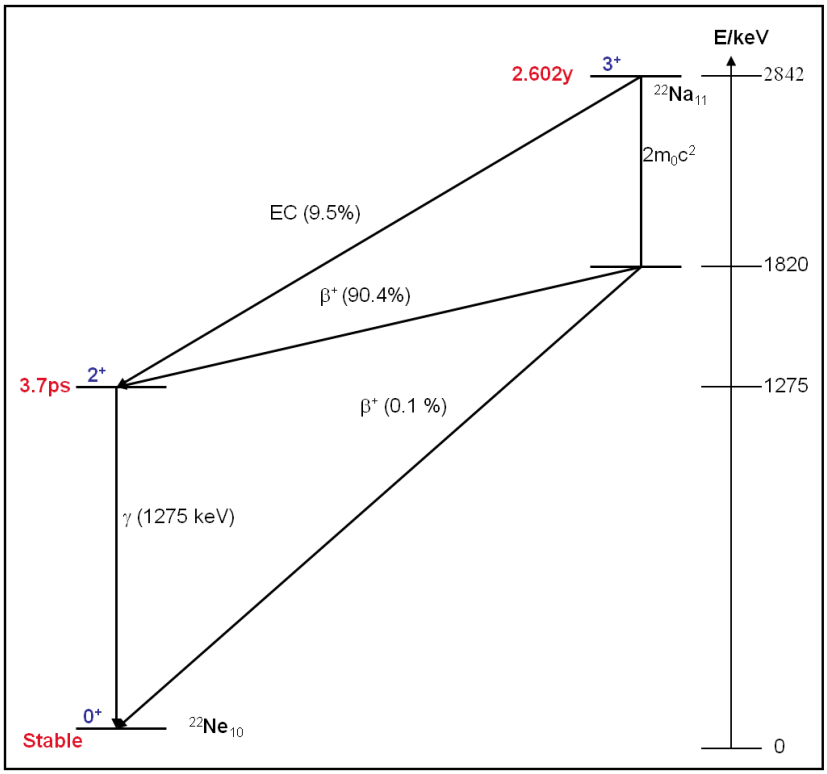

Figure 2.20: Radioactive decay scheme for ^{22}Na.

The electromagnetic interaction within an electron-positron pair causes the two to annihilate each other. The most probable decay mechanism is given by $e^+ + e^- = \gamma_1 + \gamma_2$. Each γ-ray has one half of the energy of the e^+-e^- pair such that mc^2 = 511 keV while energy and momentum are conserved. The two photons are emitted in approximately opposite directions. We can therefore obtain information about the material where annihilation occurs by the time between the birth of the 1275 keV γ-quantum and birth of the 511 KeV γ-quantum. The probability of annihilation is dependent on the density of

available electrons. In PAS, positrons are highly sensitive to regions of lower than average electron density arising from open volume defects such as monovacancies, vacancy clusters, voids, edge dislocations and grain boundaries.

It is important to note that in some cases the slowed down positron can form a bound state with a host electron. This formation is referred to as positronium (Ps). One example of such a reaction is

$$e^+ + X \rightarrow Ps + X^+$$

This formation is equivalent to a hydrogen atom with the proton replaced by a positron. The relative orientation of the spins of the electron and the positron determines whether the positron is in the singlet or triplet state. The singlet state in which the spins of the positron and the electron are oppositely directed is referred to as parapositronium (pPs) while the triplet state with parallel spins is known as orthopositronium (oPs), thus the formation of oPs is three times more likely than that of pPs. Processes involving annihilation of pPs and oPs are self-annihilation and pick-off. For pPs the main channel of annihilation involves a two-photon process. However, for oPs the two-photon annihilation can involve only the pick-off process with an electron of the host, during which oPs can annihilate with one of the surrounding atoms or molecules [45]. On the other hand, for oPS three photons are produced upon decay for the self-annihilation reaction in vacuum. Therefore, the lifetimes can be distinguished by the process through which the positron annihilates. For self-annihilation, the characteristic lifetimes are 0.1 ns for pPs and 140 ns for oPs [45]. The oPs pick-off annihilation process has longer annihilation lifetimes of 1-5 ns. Free positrons that did not undergo Ps formation have lifetimes in the 0.1-0.4 ns range in semiconductors [45].

Stopping profile of a β^+ particle in a solid is an exponential function of the penetration depth. Typical mean penetration depths are of order of 10 – 100 μm [45]. Thus, positrons probe primarily bulk properties of matter. For ZnO, a characteristic penetration depth of 48 μm can be calculated based on a density of 5.605 g/cm^3. Consequently, it can be deduced that approximately 90% of positrons annihilate in the depth up to 100 μm from the surface [46]. For the β^+ -decay positrons from ^{22}Na, the initial average and maximum kinetic energy equals 225 keV and 542 keV, respectively. The positron energy rapidly decreases in the sample over a few ps via non-elastic interactions (thermalization process). The thermalization time is negligible compared to the positron lifetime. Thermalization results primarily from successive ionizing collisions and interaction with phonons so that the initial kinetic energy of positrons (usually between 0.1 to 1 MeV) drops below 0.1 eV [45]. Once the positron reaches thermal equilibrium, it diffuses through the periodic lattice potential and interacts with its surroundings until eventual annihilation by an electron. Positron trapping in open-volume defects leads to longer lifetimes as compared to those that annihilate in defect-free regions. The diffusion length (typically in a nanometer range) determines the number of atoms to be probed for positron traps during the positron lifetime. For positron beam energies in the range of 10 eV to 100 KeV, the mean stopping depths could vary with corresponding energies from 1 mm to a few μm [45]. Therefore, PAS can potentially be used to study surface and interface regions of semiconductors and other materials.

A typical positron lifetime experimental set-up is shown in Figures 2.21 and 2.22 (referred to as the "fast-fast coincidence") with a special sandwich arrangement of a foil

source, samples and detectors. The system consists of nanosecond electronic components, which measure the time intervals between events. The detector records the start (positron arrives in the medium) and stop (positron is destroyed) γ-quanta. Constant-fraction differential discriminators (CFDDs) which are single channel analyzers, generate standard time pulses. The signals are then sent to a time-to-amplitude converter (TAC). The stop pulse is coaxial cable-delayed and the amplitude of the TAC output signal is proportional to the time delay t between the detection of birth and annihilation of photons. Thus, the spectrum is given by a histogram of counts, N vs. t and is usually a convolution of several exponential decay components.

In our PAS/LT measurements, the positron source was ^{22}Na on Ti foil with an activity of 30 μCi and another source on Kapton sheet. A conventional sandwich arrangement of two nominally identical samples and a source was placed between two Photonis VD124K high-speed photomultiplier tubes. Signals were then processed by ORTEC CFDD to select the start (1.27 MeV) and stop (511 KeV) gamma-ray signals. These signals were in turn sent to an ORTEC TAC connected to a Trump Multichannel Analyzer with Maestro-32 software program to acquire and control the data. The PAS/LT spectra were analyzed by a fitting software to evaluate the lifetime components τ_i along with their intensities I_i. Each spectrum contained approximately 1-2 × 10^6 counts.

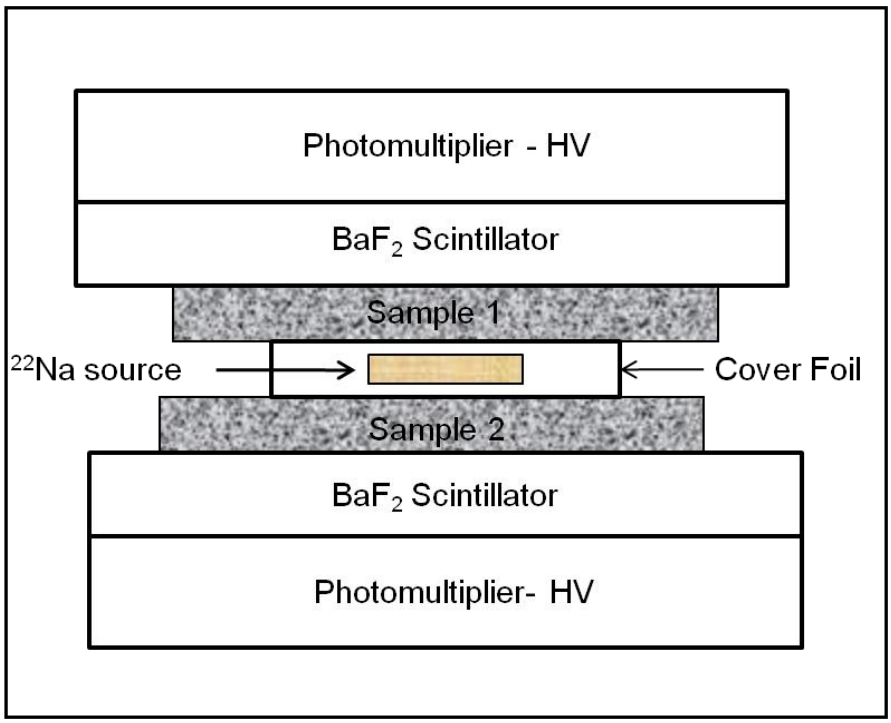

Figure 2.21: PAS sample/source experimental geometry.

The sample holders were cylindrical polyethylene cups with polyethylene stages providing various depths to accommodate samples. The cups containing the two identical samples were sealed with polyethylene rings using 8-micron Kapton films. In order to assess errors related to sample arrangement inside a sample holder, placement of the sample relative to the source as well as transient effects, for each specimen we ran several experiments on different days.

Doppler broadening and angular correlation are two other PAS techniques that are not discussed here.

PAS/LT shows sensitivity to numerous defect structures in substances including such semiconductors as ZnO. In materials with grain size of a few tens of nanometers, the majority of the positrons diffuse to the grain surfaces, which are defective in nature

[47]. Thus, PAS/LT can be used to obtain information about defects in ZnO specimens on the nanoscale level, specifically to understand possible changes in free volume defects in ZnO nanoparticles before and after remote plasma treatments. For nanostructured ZnO, with a large surface-to-bulk ratio, plasma could affect a substantially larger volume fraction, thus providing enhanced effects on the surface/subsurface defects. PAS measurements of a nanocrystalline ZnO may also provide information on the differences between ZnO species of variable morphology and structure.

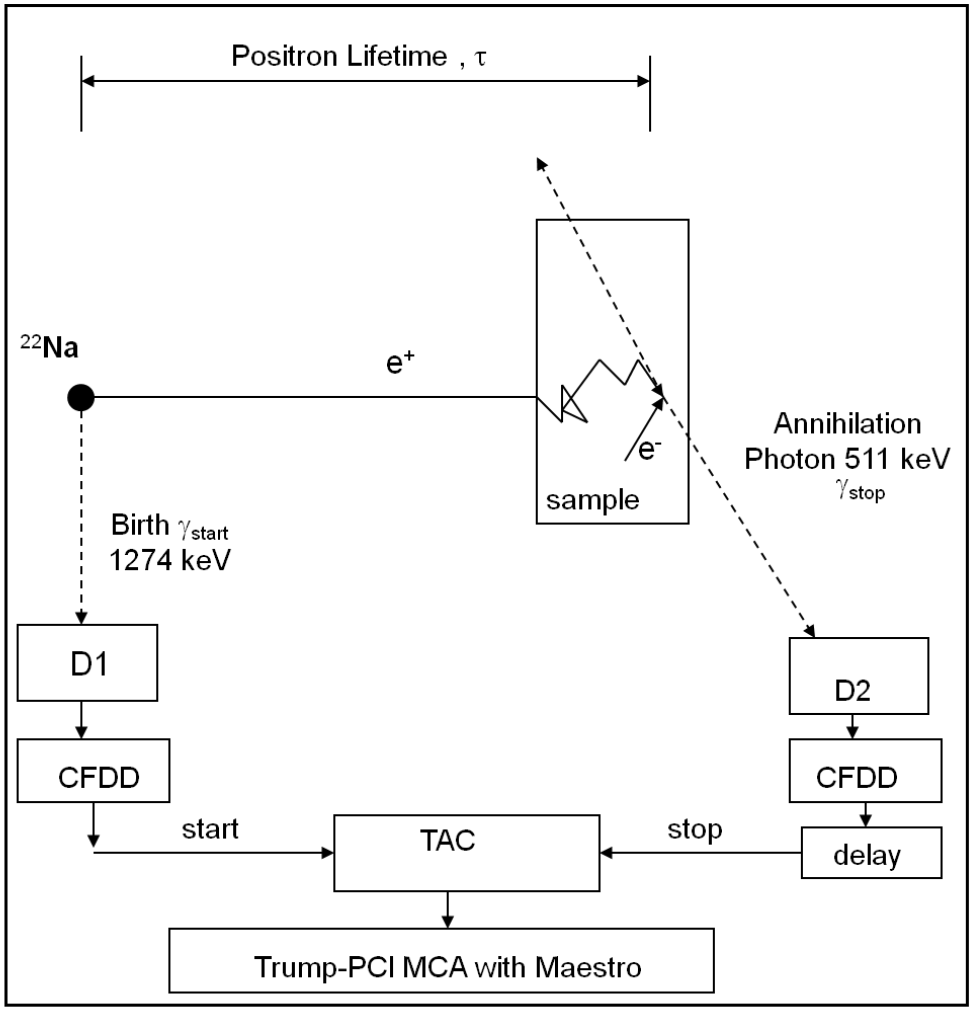

Figure 2.22: PAS/LT measurement sequence.

II.4 Photoluminescence Spectroscopy

Luminescence spectroscopy is a popular and very effective technique for detecting optically-active defects. Incident illumination photons generate high population of electron-hole pairs, which, following thermalization, recombine with each other by emitting secondary photons. Such recombination occurs via different mechanisms, oftentimes mediated by the defect states in the band gap.

In our PL setup, the signal is excited by a CW Kimmon IK5452R-E HeCd laser with a wavelength of 325 nm. A variable frequency chopper is employed to provide a reference frequency. The samples are mounted inside an evacuated Janis CCS-150 cryostat operating within a controllable range of temperatures between 8 and 325 K. The spectra are probed by a Spex 1401 monochromator with a spectral resolution of 0.18 cm^{-1} and an RCA C31034 photomultiplier tube detector connected to a Stanford Research-830 lock-in amplifier for a background noise reduction.

Chapter III. PAS/LT and PL investigations of the ZnO nanopowders

Although ZnO nanostructures are realized in many morphologies and dimensionalities, we chose, as a natural starting point, to run experiments on a number of commercially available ZnO nanopowders with different average grain sizes. ZnO nanopowders represent an important class of ZnO nanosystems. They are valuable objects for research, firstly, because of their bulk commercial availability in a large variety of sizes and morphologies, and also due to their numerous and diverse applications (electrical and optoelectronic components, tire industry, agriculture, pharmaceutics and personal care, chemical technology, ceramics, etc.) In the past few years numerous novel applications of ZnO nanopowders have been suggested and tested. Elucidation of defect properties in ZnO nanopowders is an object of nascent vigorous investigations.

We performed SPV, AES, PL, and PAS measurements on a range of commercially available ZnO nanopowders (along with a bulk single-crystalline ZnO as a reference) with varying size and morphology to elucidate materials' quality, optoelectronic properties, defect-related behavior, and the impact of the surface/volume ratio. We also used remote plasma treatment as a surface-specific processing tool.

III.1 Experimental details

III.1.1 Samples

Nanopowder ZnO samples were obtained from four different vendors: Alpha Aesar, Sigma Aldrich, American Elements, and Zochem. The latter two supplied

different grades with dissimilar average grain sizes. Hereinafter we will use the following corresponding abbreviations to distinguish between six different nanopowder specimens: AA, SA, AE25, AE31, ZA, and ZB. To verify nanocrystal size distributions and morphologies, the samples were characterized by scanning electron microscopy (SEM) and transmission electron microscopy (TEM). Crystal sizes and size distributions were determined from the SEM/TEM images (Figure 3.1) with 30 to 50 nanocrystals per sample being analyzed. The distributions of the average grain size were obtained for the AA, ZA and Z samples from the analysis of the electron microscopy images as follows: AA ~ 70 ± 30 nm, ZA ~ 180 ± 100 nm and ZB ~ 210 ± 100 nm.

Bulk ZnO single-crystalline sample was obtained from Cermet Inc. for reference measurements.

In addition, the as-received powders were compressed at room temperature into circular pellets ~ 2 mm thick and ~ 1.3 cm in diameter using a Carver hydraulic column press with the nominal force of 7 metric tons (Figure 3.2). The pellets were rather brittle pointing to a relatively weak bonding between the nanocrystals.

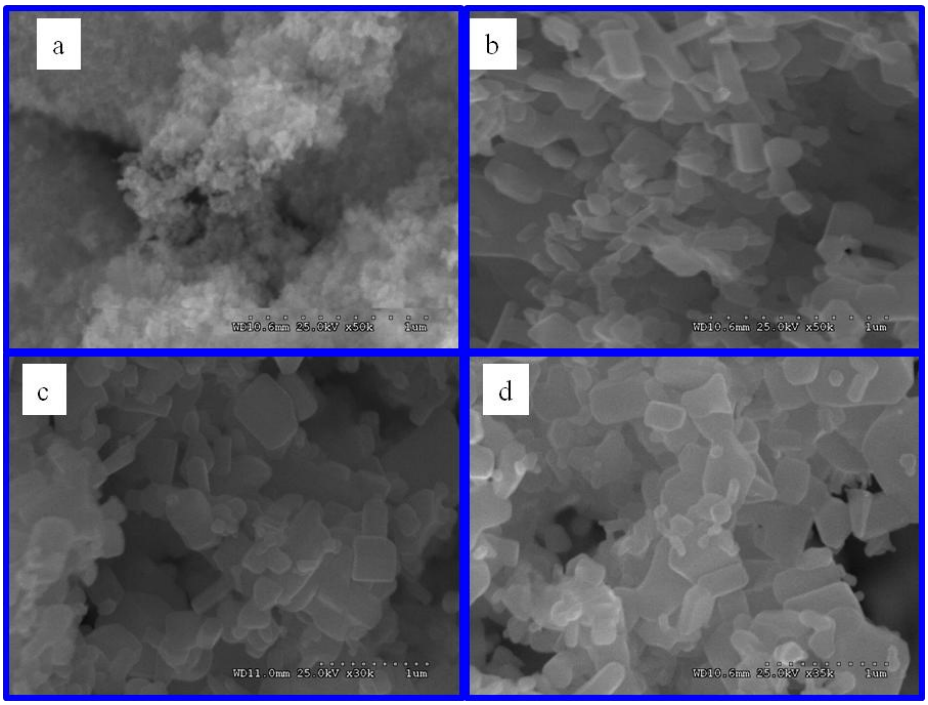

Figure 3.1: SEM images of ZnO nanopowders: (a) AE25; (b) AE31; (c) ZB; (d) ZA.

Figure 3.2: Pelletized samples.

III.1.2 PAS Procedure

PAS/LT measurements in ZnO were reported by many authors [48], and a reasonable degree of understanding of the results for the bulk single-crystalline materials has been achieved. Still, many effects remain ambiguous and assignments of individual

LT components are rather tentative. The situation becomes significantly more complicated with ZnO nanostructures due to such factors as presence and abundance of the surface and sub-surface layers rich in defects, substantial free volume contributions of the inter-granular voids, as well as interplay of the positron diffusion length and the grain size. Recent reports on the LT studies of nanosized ZnO, and ZnO nanopowders in particular [9, 47, 49, 50], revealed a substantial discrepancy in the interpretation of the obtained results. Not only were the assignments of the measured components varying from author to author but the fitted values of the LT components were reported to span over a broad range as well. The surface/subsurface defect contributions to the positron spectra were discussed, although no surface-specific processing techniques were applied in conjunction with the positron annihilation experiments.

III.2 Results and Discussion

III.2.1 PAS/LT Measurements

Practically for all our samples, the best fits of the positron annihilation spectra can be obtained using three LT components τ_1, τ_2, τ_3 (with relative intensities I_1, I_2, I_3).[51] The first two components τ_1 (below 200 ps) and τ_2 (above 300 ps) are predominant, whereas the τ_3 component (ranging between slightly below 1 ns to several ns) is relatively weak. Usually, the shortest values are related to bulk recombinations while the longer ones are due to annihilation in a free volume, defect-related or otherwise [49]. The τ_3 component was found to be statistically insignificant and we employed it primarily for optimization of fitting results.

Detailed analysis of the collected LT spectra revealed a common peculiarity: although the three-component model consistently yields the most reasonable fits of the experimental annihilation curves, the exact LT values cannot be established precisely. This ambiguity is the most striking for the shortest component. For practically all the samples we observed (see Appendix A) several stable local minima of the fitting parameter manifolds corresponding to different seed values of τ_1 (140 ps, 160 ps, and 180 ps). Surprisingly, for all these stable fits, the fitting variances turned out to be very close. A strong dependence on the resolution function parameters (either fixed or variable) was also observed. We concluded that the fitting ambiguity does not provide unequivocal assignment of the LT components, and probably explains the discrepancies in the previously reported LT results [9, 49, 50, 52, and 53]. Apart from the fact that in the case of ZnO crystals we are dealing with lifetimes of the order of instrumental resolution, possible explanation of the detected uncertainty can be linked to the existence of defect clusters (especially within the grain surfaces) with a continuous distribution of sizes as well as inter-granular voids of different volumes and shapes. Moreover, additional "fudging" effect can be introduced by the fact that the average size of a nanocrystal can fall below the positron diffusion length leading to a dominating role of the surface layers in positron annihilation [49].

However, regardless of a specific set of the fitting values, the mean LT $\tau_M = \sum \tau_i I_i / \sum I_i$ turned out to be insensitive to the seed values and local minima on the parameter manifold. Thereby, we accepted τ_M as a meaningful physical quantity providing account of the overall positron recombination response in a given specimen. The solid squares in Figure 3.3 correspond to calculated values of τ_M for the as-received

ZnO nanopowders and a reference ZnO bulk crystal with multiple points per sample corresponding to different trials (see Chapter II). These values were obtained for a free fit with a fixed resolution function. Sample-to-sample distribution of the shown lifetimes reveals only a limited correlation with the average grain size – the reference bulk crystal has the smallest average LT, the ZA/ZB samples with larger grains show the shortest τ_M among all the powders and AE31 has a somewhat shorter average LT compared to its smaller-grain counterpart AE25.

Comparison of PAS/LT measurements of the nanopowders with those of the bulk sample (Figure 3.3) reveals that the reference bulk sample has a significantly lower mean lifetime. This suggests a significant relative abundance of defects in nanopowders in good agreement with the suggestion that positron annihilation in nanocrystalline materials is qualitatively different [47].

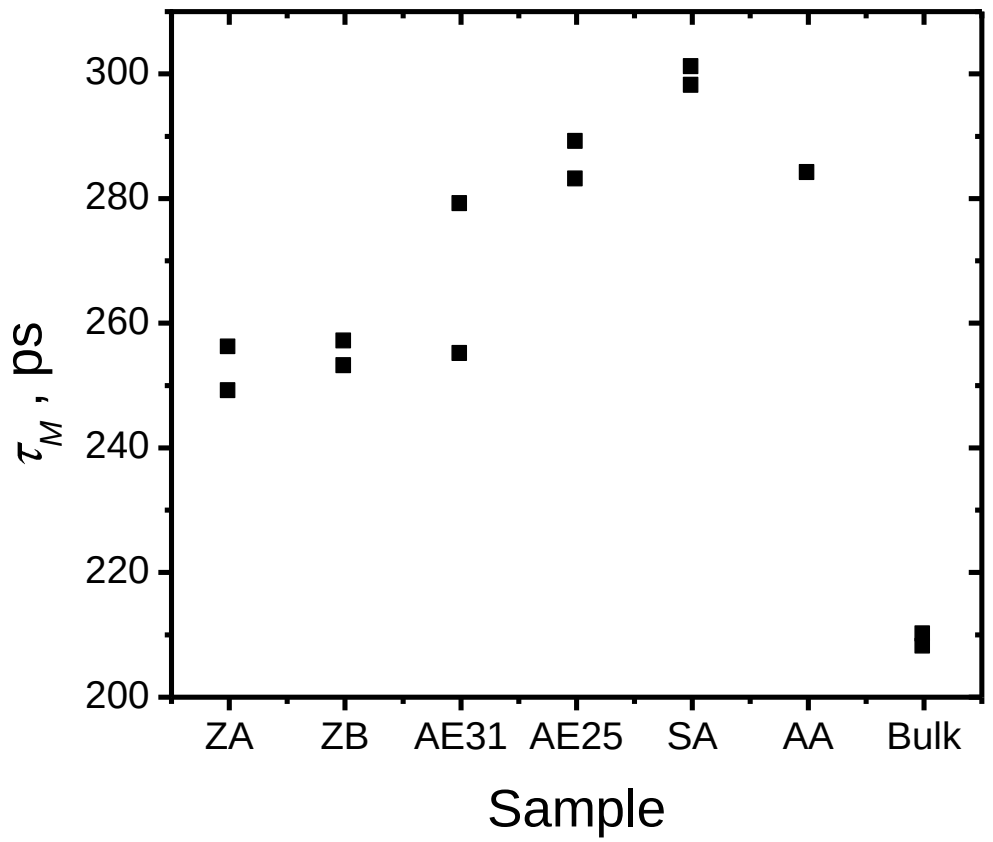

Figure 3.3: Average positron lifetimes for the as-received ZnO nanopowders.

We addressed the issue of the contribution of the intergranular spacing to the PAS lifetimes. Additional PAS/LT measurements were carried out on the pelletized ZnO nanopowders forms, prepared as mentioned above. Obviously, during pelletization the intergranular spacing shrinks as shown in Figure 3.4. Compression of the powders into pellets brings in further modifications of the LT parameters (Fig. 3.5, circles). For all the specimens, pelletization bears a consistent and visible decrease of the mean LT, a robust evidence of the contribution to τ_M of the inter-granular space, albeit convoluted with the annihilation on crystal defects.

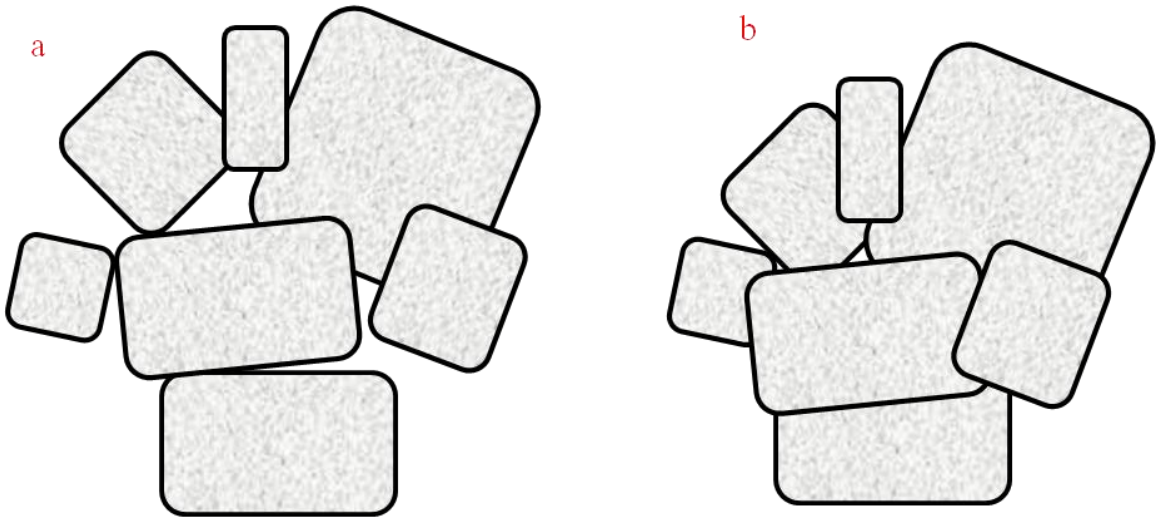

Figure 3.4: Reduction of intergranular spacing after pelletization

Thus we conclude that there is always a contribution to the PAS lifetimes from the intergranular spacing in nanoscale ZnO specimens. It is therefore important to always reduce the intergranular spacing to obtain more realistic PAS/LT characteristics.

III.2.2 PL Measurements

The results of the PAS/LT experiments were correlated with the optoelectronic properties of the samples, as probed by the photoluminescence spectroscopy. Generally, ZnO is a very luminescent material. Literature describes a variety of PL defect signatures in ZnO associated with states of different origins and positions in the band gap. Understanding the nature of luminescent defects in the ZnO gap is among the most pressing issues in defect studies in this material. Despite decades of research in the field of optoelectronic properties of ZnO, an unambiguous assignment of the optical transitions to specific defects in ZnO is largely missing. Many radiative transitions occur in the visible part of the ZnO PL spectra. The shape of the spectral distribution of the visible

bands varies from case to case and is oftentimes very sensitive to the quality and the history of the specimen. Recent theoretical studies for single native defects offer plausible explanation for such uncertainty in assignment, resulting from a multitude of possible transitions with similar energy differences involving different charge states of assorted native defects [54]. One should also bear in mind that the transitions are mediated not only by native defects but also by most common impurities, extended defects, and defect clusters. Whereas optical centers located deeper in the gap are readily

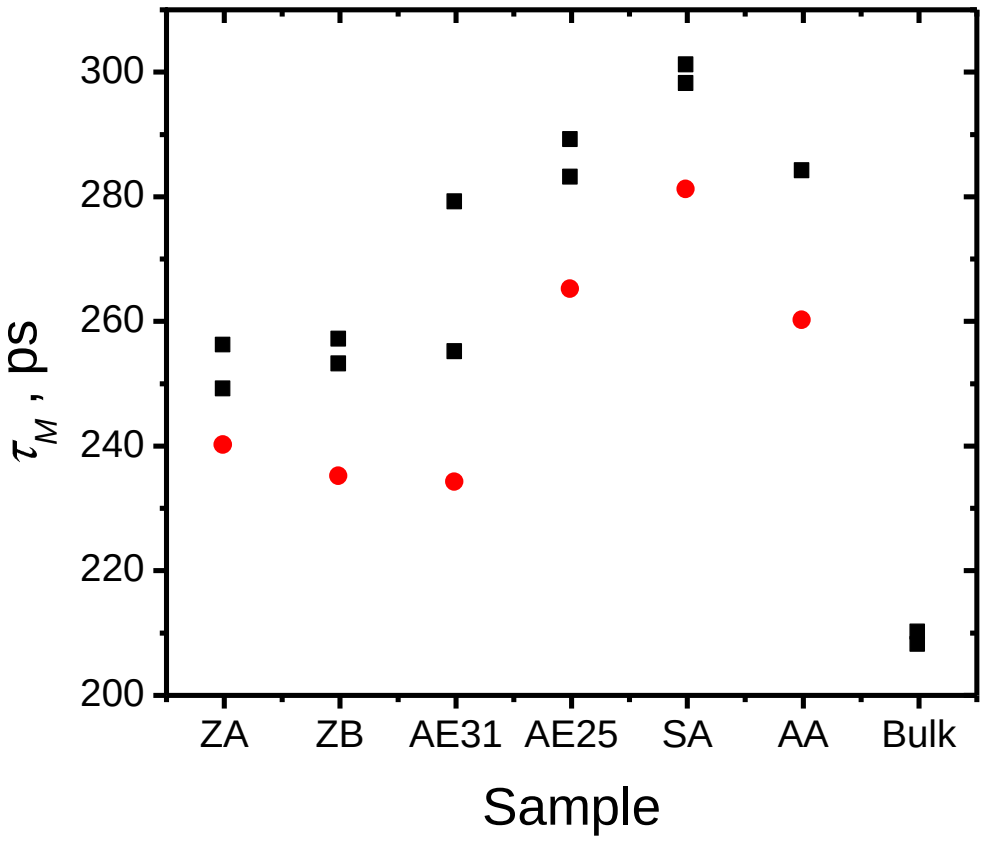

Figure 3.5: Effects of pelletization on the average positron lifetimes of the ZnO nanopowders (squares – as-received, circles – pelletized).

detectable in a wide range of temperatures, observation of transitions associated with shallow defects requires low temperatures.

There is a greater degree of correlation though between the results shown in Fig. 3.5 and the relative intensity of the defect emission in the PL spectra of the as-received specimens (Fig. 3.6), indicating prevalent dependency on the particular defect properties of a specific ZnO nanopowder rather than a generic scaling behavior. One can see significant variations between room temperature PL spectra of different nanopowders.

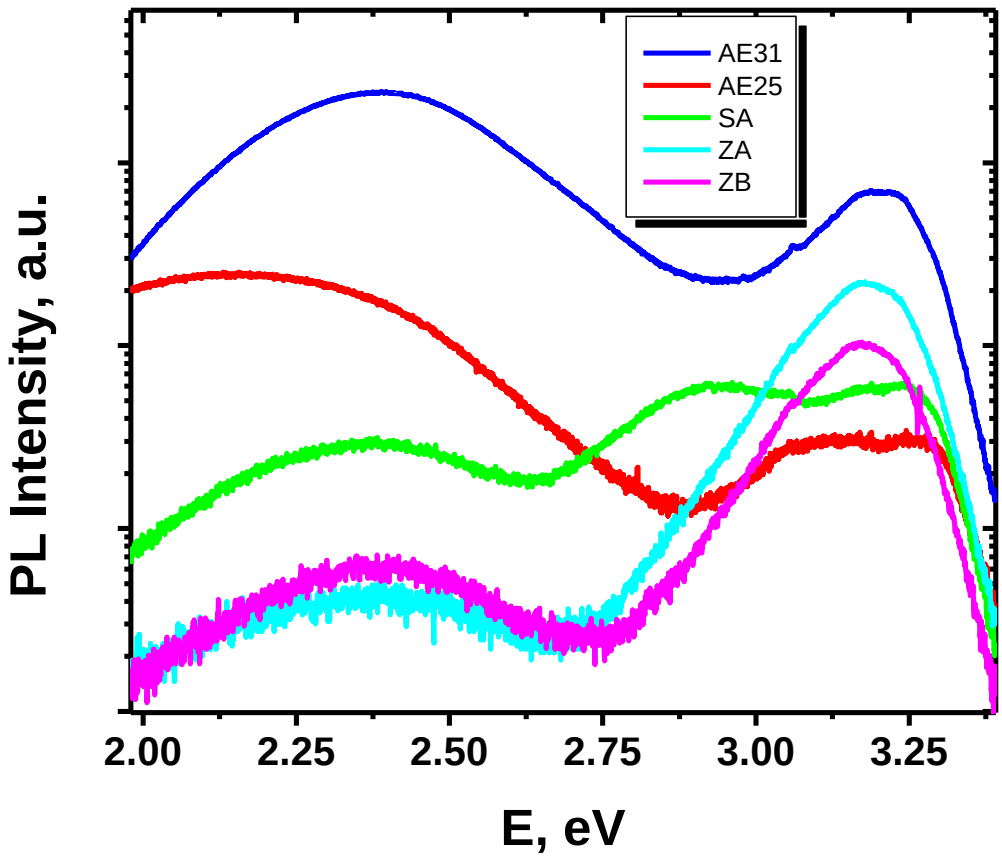

Figure 3.6: Room temperature PL spectra of the as-received ZnO nanopowders.

Thus, the ZA and ZB powders show a relatively high intensity of the near-band edge (NBE) emission at ~ 3.2 eV and a much weaker deep defect emission band centered at ~ 2.4 eV. This observation is consistent with the lower PAS/LT values. For the AE31/AE25 samples the relative intensity of the defect emission exceeds that of the near-band edge intensity (~3.2 eV) and is much stronger than in the ZA and ZB samples, again showing a consistency with the PAS/LT results.

Again, as can be seen from Fig. 3.6, the defect properties are significantly different from sample to sample, and even for the same vendor (as in the case of specimens AE 25 and AE31), the spectral differences are be substantial too. Evidently, sample-to-sample differences in crystal quality obscure potential spectral dependence on the size and morphology of the ZnO nanocrystals.

We obtained Gaussian-resolved fits for the room temperature PL spectra of the studied samples to further elucidate characteristic emissions as shown in Figures 3.7-3.11 below. The AE 31 and AE 25 samples both have defect levels at ~ 2.2 eV. On the other hand, the SA, ZA and ZB nanopowders all have the characteristic emission of ~ 2.3 eV. Similarly, all the samples have spectral features at ~ 2.9 eV. This indicates that even for samples among the same vendors there are differences in the characteristic defect features.

The results of Gaussian fitting for the PL spectra described above are synopsized in Table 3.1 for the most prominent components.

It is important to note that despite decades of research in the field of optoelectronic properties of ZnO, an unambiguous assignment of the optical transitions to specific defects in ZnO is largely missing. Moreover, recent report [54] on theoretical

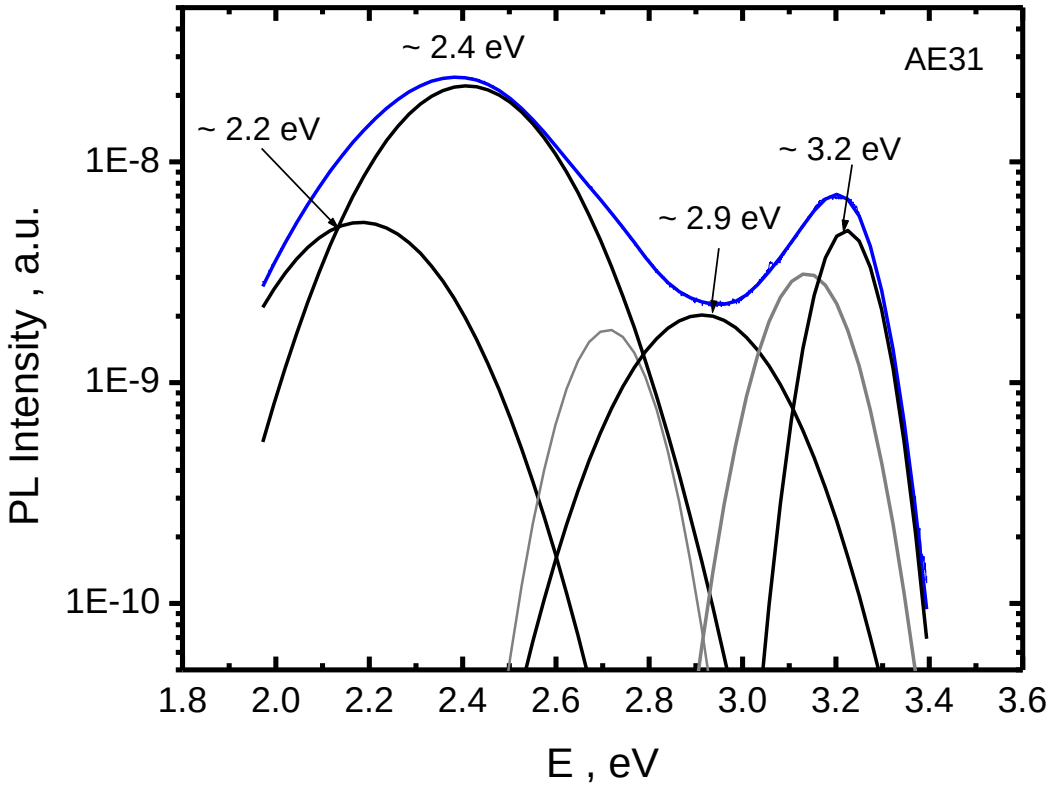

Figure 3.7: Gaussian-resolved PL spectrum of the AE31 sample.

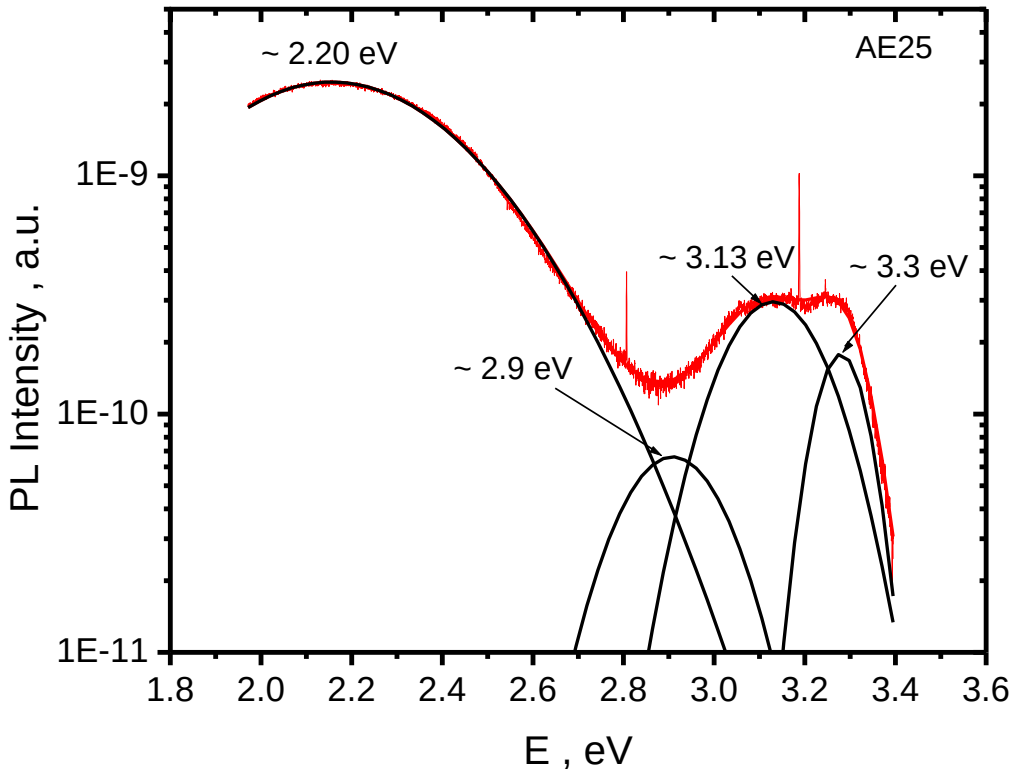

Figure 3.8: Gaussian-resolved PL spectrum of the AE25 sample.

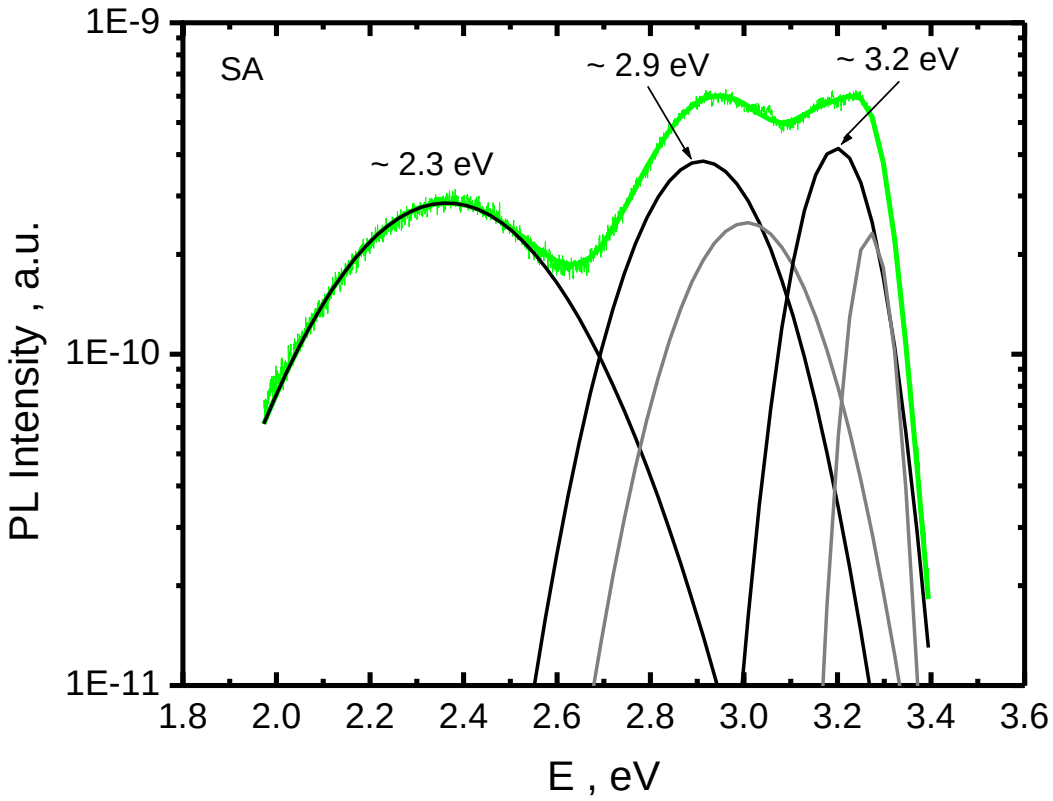

Figure 3.9: Gaussian-resolved PL spectrum of the SA sample.

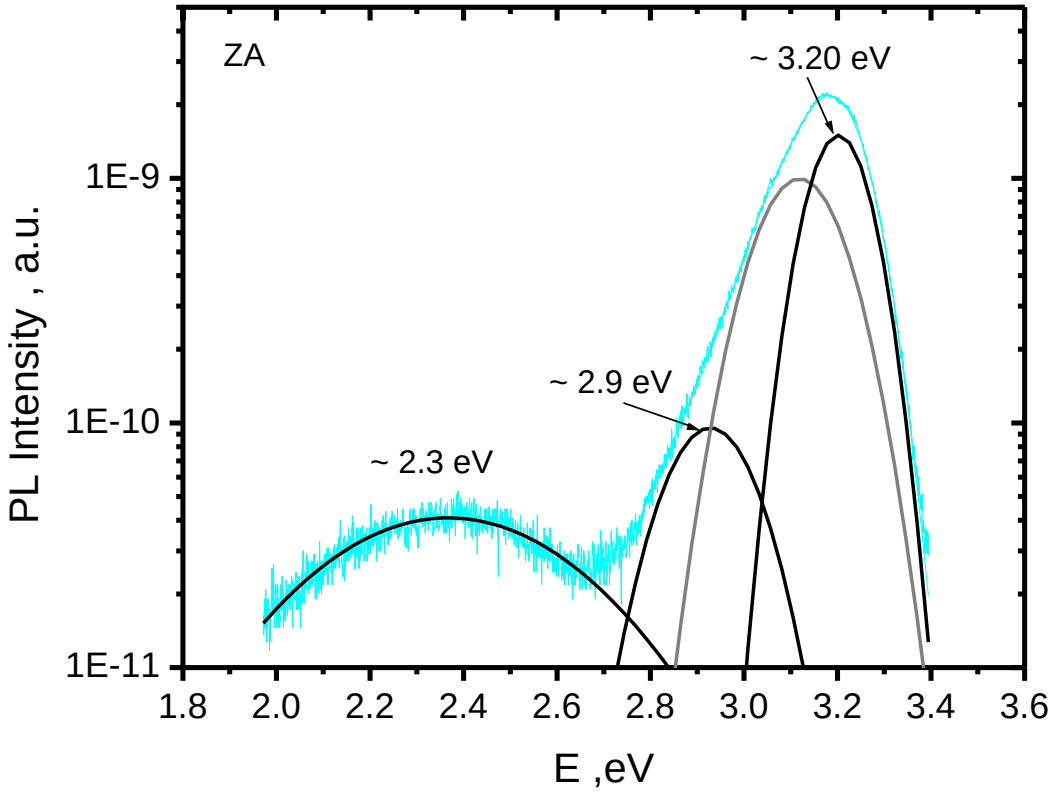

Figure 3.10: Gaussian-resolved PL spectrum of the ZA sample.

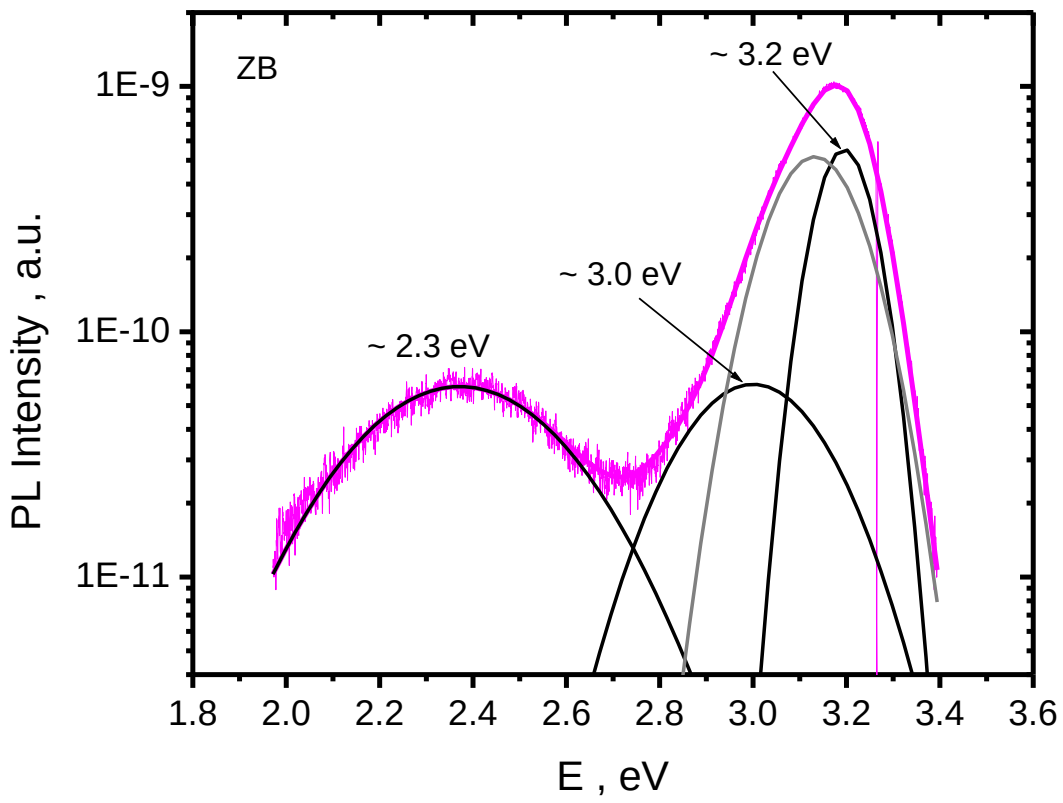

Figure 3.11: Gaussian-resolved PL spectrum of the ZB sample.

studies for native point defects offer plausible explanation for such uncertainty in assignment, resulting from a multitude of possible transitions with similar energy differences involving different charge states of assorted native defects. One should also bear in mind that the transitions are mediated not only by native defects but also by most common impurities, extended defects, and defect clusters. For nanosize crystals the picture becomes even more intricate because of the contribution from the surface-related optical transitions as well as the size-related spectral shifts.

Sample	*Approximate transition energy (eV)*
AE31	2.2, 2.4, 2.7, 2.9, 3.1, 3.2
AE25	2.2, 2.9, 3.1,3.2
SA	2.4, 2.9, 3.00, 3.20
ZA	2.4, 2.9, 3.1, 3.2
ZB	2.4, 3.0, 3.1, 3.2

Table 3.1: PL transitions in the ZnO nanopowders obtained from Gaussian fits.

In view of these arguments, before attempting to assign specific defects to the observed optical transitions of the Gaussian-resolved spectra for each sample, we suggest that the relative abundance of optically-active defects in our samples is a good measure of the overall quality of the nanocrystals studied.

There are several important observations that stem from our PL and PAS/LT experiments on the as-received ZnO nanopowders. In all the nanosized samples the mean LT has a substantially higher intensity compared to that of a bulk sample, indicating a significant abundance of free volume. The correlation between the mean LT values on the one hand and the average nanocrystal size on the other is rather insignificant, which exposes a much stronger influence of the quality of individual powders overshadowing possible scaling effects. Nevertheless, our results are consistent with a substantial increase of the free surface in the nanopowder samples as a source of a higher concentration of defects within the surface and subsurface layers.

It should be noted that in our group we performed numerous PL experiments on nanoscale ZnO of various morphologies and sizes (e.g., [55-57]) and many of these experiments confirmed the model of the defect-rich surface in nanocrystalline ZnO.

Chapter IV. SPV studies of the ZnO nanopowders

As discussed above (cf. Chapter III), analysis of the PAS and PL spectra shows an abundance of defects in the ZnO nanopowders with an insignificant evidence of scaling effects. SPV is known [13] for its ability to detect surface states and distinguish their charge sates and donor- vs. acceptor-like nature, with additional information transpiring from the SPV transient measurements. SPV as an experimental tool is capable of providing further important information on the surface defects in ZnO nanopowders. One major advantage of SPV is that it is sensitive to surface and bulk defect state parameters. SPV can significantly help with identifying the origin of defect sates detected by PL and PAS.

In recent years there were only a few published SPV studies of nanoscale ZnO [58-63]. Most of them employed a capacitive SPV geometry, and the spectra did not reveal well-defined surface defect transitions, primarily because of a relatively low signal-to-noise ratio. Moreover, these experiments were performed, as a rule, in ambient air. In our work we implemented the Kelvin-probe geometry of the SPV setup *in vacuo* and *in situ* with RP and AES. We were able to obtain clear spectral signatures of a number of defect states and observe a significant plasma-induced evolution of the surface.

One has to bear in mind that SPV experiments on nanocrystalline samples pose a challenge. In macroscopic crystals, the efficient separation of the electron-hole pairs, essential for meaningful SPV response, is driven by the built-in field in the space-charge region as well as the Dember effect (light-induced concentration gradient) [64]. When

the crystal size becomes comparable to the thickness of the space-charge region and the characteristic diffusion length, detection of the SPV signal may become problematic because of the lower field and faster diffusion [58]. For the smallest particles the additional complication arises from the disappearance of a well-defined band gap.

IV.1 SPV Procedure

SPV characterization was performed on the as-received and pelletized powders before and after remote plasma treatments. The as-received powders were deposited with a spatula on a surface of a vacuum-compatible conductive carbon tape (Figure 4.1). For the plasma treated samples, we employed a high-grade oxygen/helium gas mixture (flow rate ratios ~ 1:2) using 150-200 mTorr of gas pressure and 30-40 W of power of the generator. The samples were placed ~ 15 cm downstream from the plasma-generating coil. The plasma exposure time varied between 15 and 40 min. We add the 'PLT' suffix to distinguish the pelletized specimens and the 'RP' suffix to distinguish the RP-treated powders.

Figure 4.1: ZnO nanopowder deposited on carbon tape.

As mentioned previously, white light was focused into the slit of a monochromator by a pair of fused silica lenses. The light of a variable frequency exiting the monochromator entered an F# matcher connected to an optical fiber bundle remotely illuminating the sample's surface placed within a few mm of the vibrating Kelvin probe electrode for signal collection. Prior to obtaining the SPV response to the varying photon energy, the ZnO samples were exposed directly to white or monochromatic light in order to obtain SPV saturation of the surface states followed by dark saturation.

IV.2 SPV Results

IV.2.1 SPV Spectral Signatures

Our super-bandgap SPV data (Figure 4.2) indicates that the ZnO nanopowder semiconductor samples are *n*-type with a band gap value of ~ 3.3 eV consistent with the literature. A well defined optical direct band gap was obtained even for the AE25 sample with the smallest grain size, which is an indication that by employing the *in vacuo* approach we successfully overcame the problem of a weak SPV response due to the inability of the photogenerated electrons and holes to separate effectively [65, 66]. Analysis of the SPV spectra of the studied samples [67] revealed a variety of transitions, most of which were reproducible in the spectra of different powders. Some of these transitions are illustrated in Figures 4.3a-4.6a. Table 4.1 summarizes some most common SPV transitions observed in the studied samples. The remainder of the transitions observed in our samples is listed in Appendix B.

Despite common transitions observed in different samples substantial vendor-to-vendor discrepancies are still evident in both the distribution of the spectral signatures as

well as their relative intensities consistent with the results of Chapter III and previous reports [56]. It must be noted that specific assignments of the defects are more challenging for nanoscale samples compared to single crystals. So far, theoretical calculations of native defects energetics have been performed only for bulk ZnO showing multitudes of possible transitions with similar locations in the gap and different charge states. As of today no consistent calculations have been performed for native surface defect states in nanocrystalline ZnO. Therefore, in the absence of adequate theoretical treatment we may only speculate on the specific assignments of the observed defect states. One can tentatively plot the observed defect levels against the energy levels calculated theoretically in [54] for bulk ZnO. Examples of such plots are given in Figures 4.3b to 4.6b. As one can observe, many of these theoretically calculated defect states are located in the close proximity of each other, especially in the mid-gap vicinity. More similar plots can be found in the Appendix B.

Most of the experimentally observed SPV features could be tentatively attributed to oxygen vacancies, zinc vacancies, and oxygen interstitials. However, we should note that the transitions obtained from the SPV spectra might also be associated with common impurities, extended defects, and defect clusters.

We found that compression of the powders into pellets bears a consistent and visible improvement in the SPV signal-to-noise ratio and spectral stability, a robust evidence of the contribution to enhanced electron-hole pair separation from the reduction of the inter-crystalline space and the increased interaction between grains' surfaces.

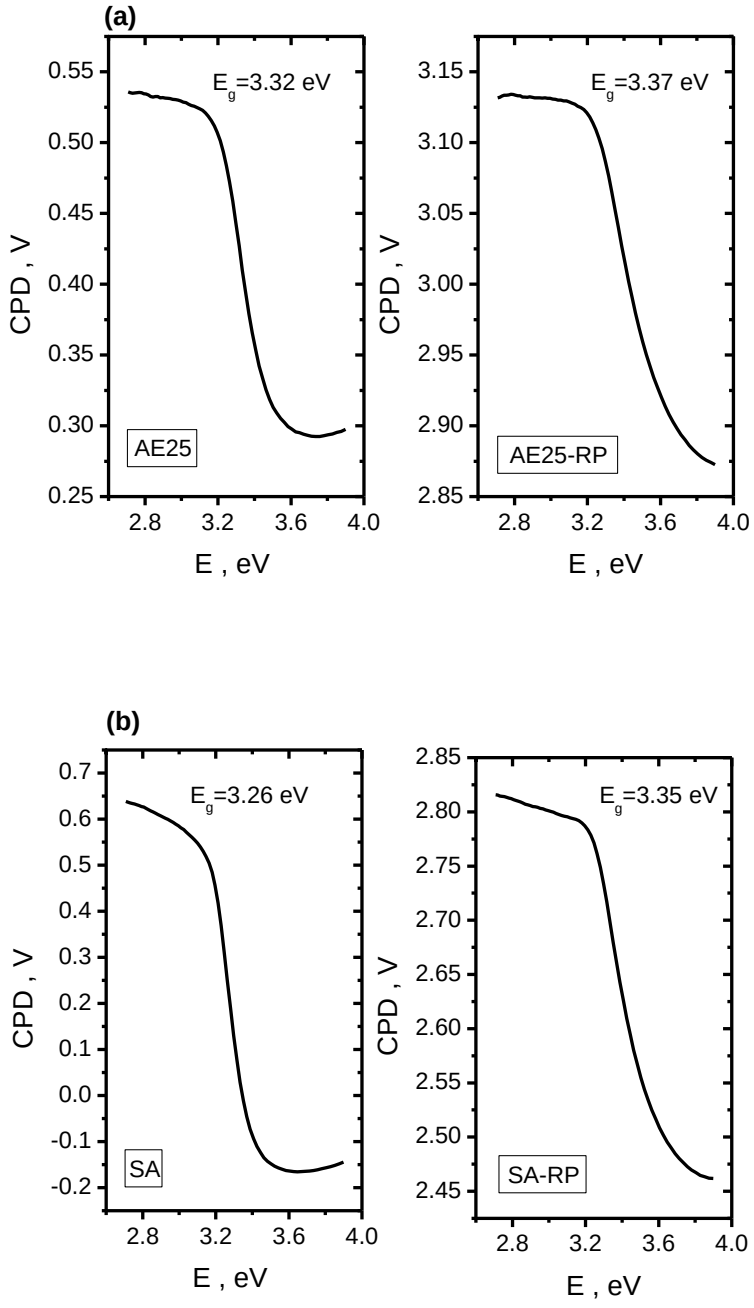

Figure 4.2: Band gap transitions in the SPV spectra of the as-received and remote plasma treated samples – (a) AE25 and (b) SAP.

(a)

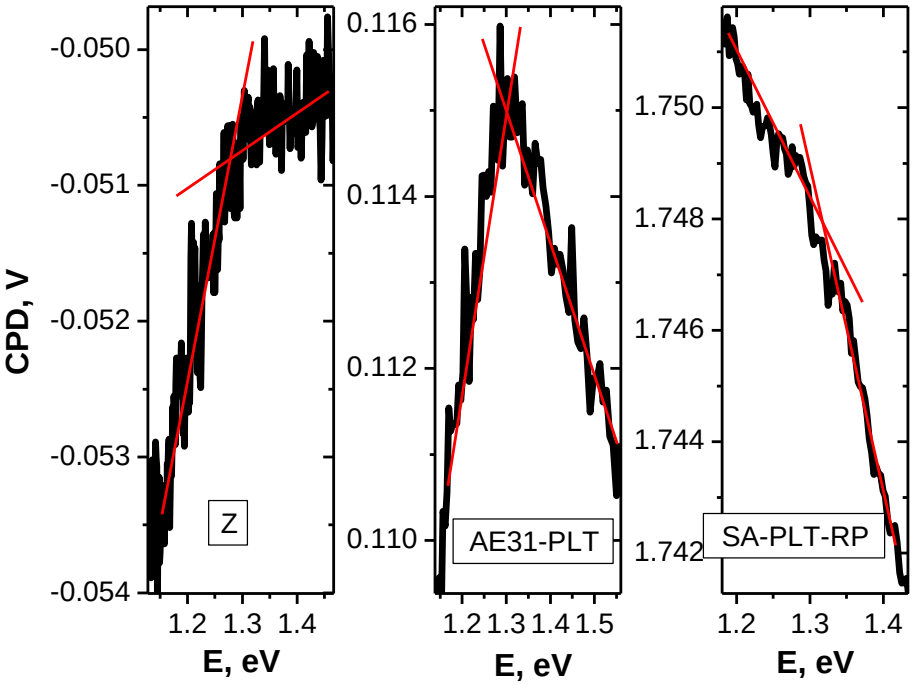

(b)

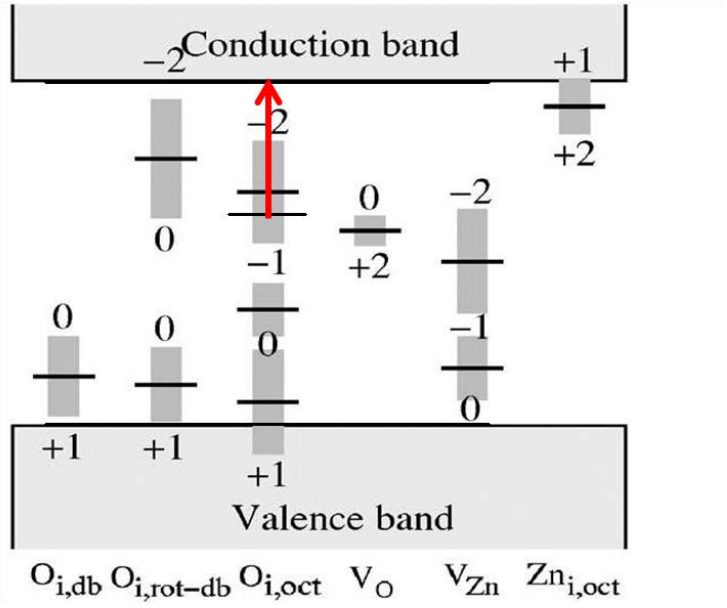

Figure 4.3: ~ 1.3 eV SPV transition to the conduction band.

(a)

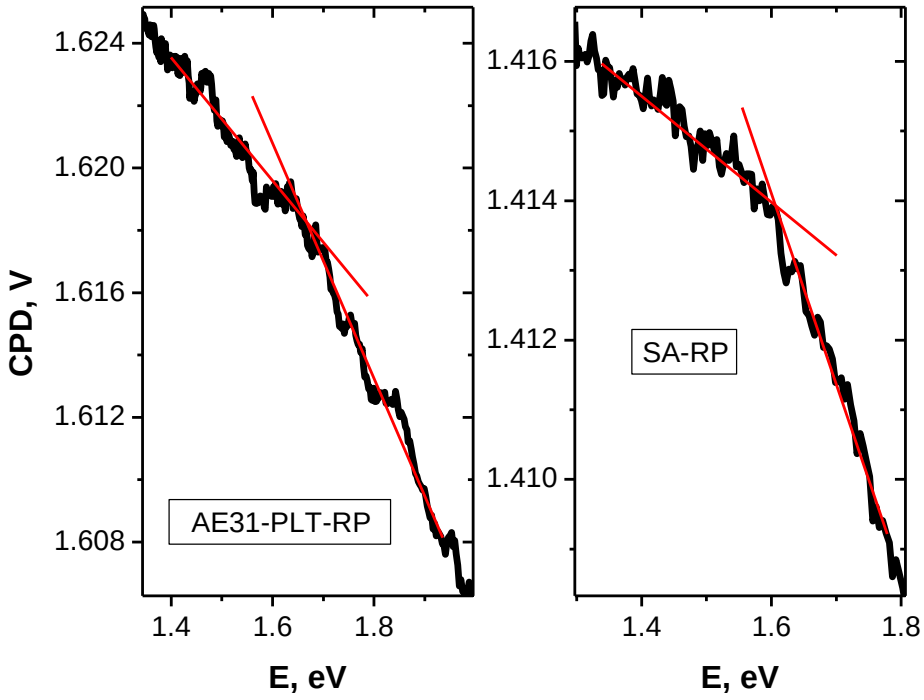

(b)

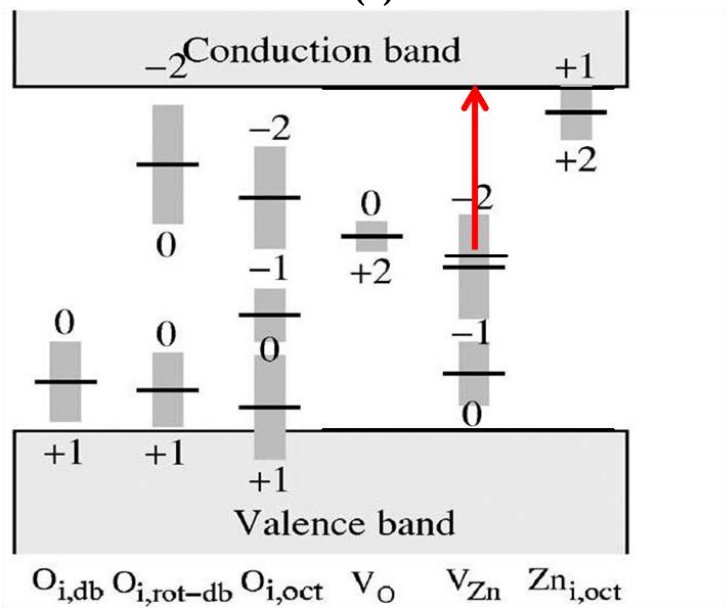

Figure 4.4: ~ 1.65 eV SPV transition to the conduction band.

(a)

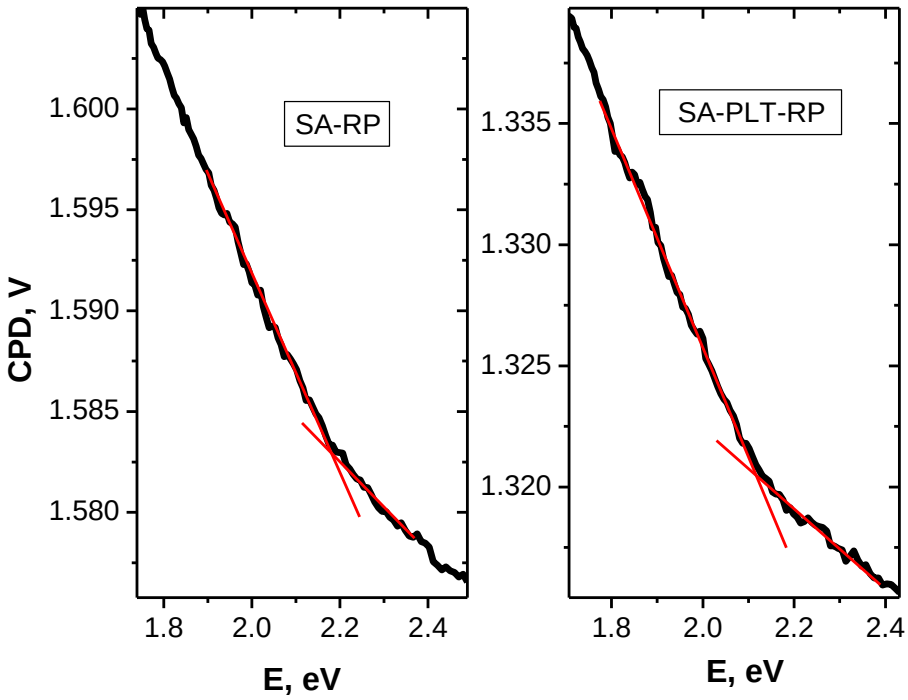

(b)

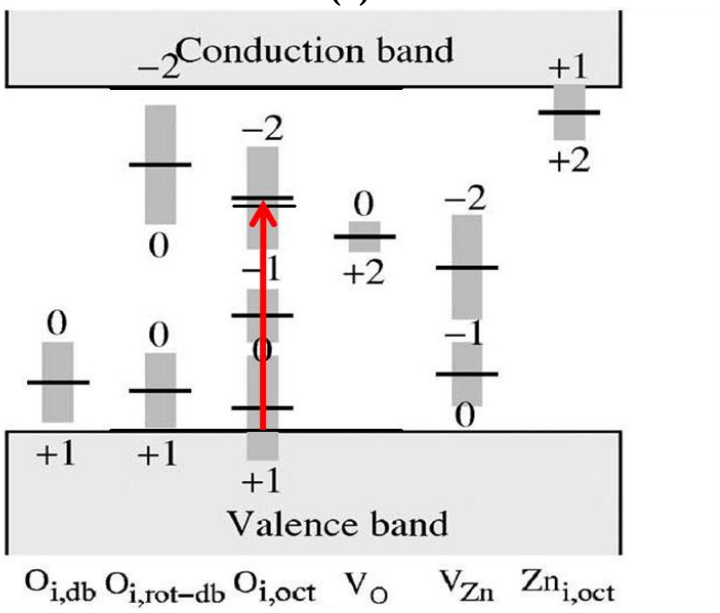

Figure 4.5: ~ 2.2 eV SPV transition from the valence band.

(a)

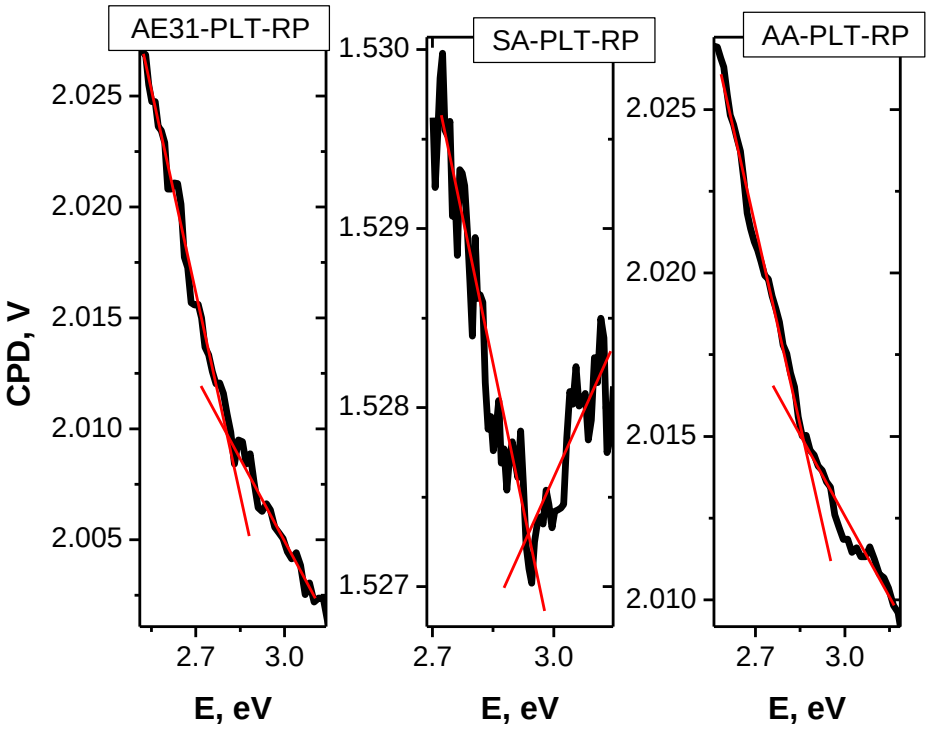

(b)

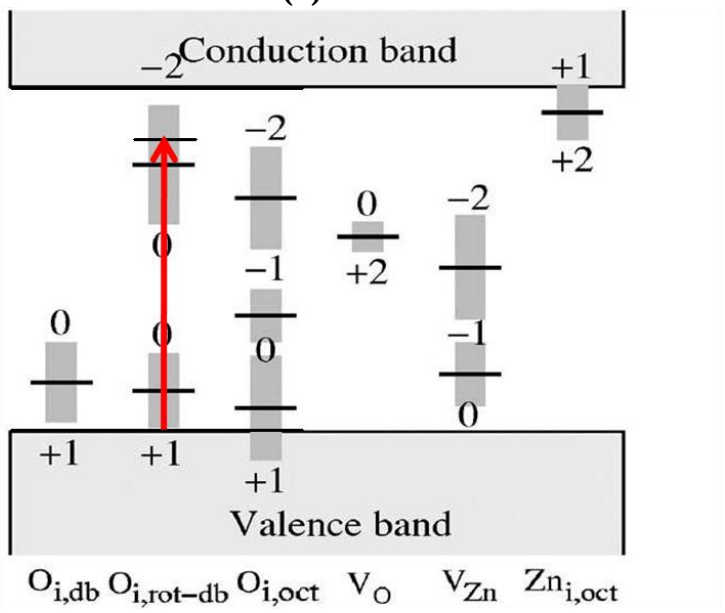

Figure 4.6: ~ 2.85 eV SPV transition from the valence band.

As-received samples	$E_c - E$, *eV*	$E - E_v$, *eV*	*RP-processed samples*	$E_c - E$, *eV*	$E - E_v$, *eV*
Z	1.3	-	Z-RP	1.65, 2.9	-
AA-PLT	1.65	-	AA-PLT-RP	1.65	2.2, 2.4, 2.85
AE25	-	-	AE25-RP	1.5, 1.65	2.2, 2.4, 2.85
AE31	-	-	AE31-RP	1.3, 1.5, 1.65	2.2
AE31-PLT	1.3, 1.5	2.85	AE31-PLT-RP	1.5, 2.9	2.85
SA	-	-	SA-RP	1.5	2.2
SA-PLT	1.3	2.85	SA-PLT-RP	1.3, 1.5, 1.65	2.2, 2.85

Table 4.1: Summary of the most common SPV transitions observed in the studied samples.

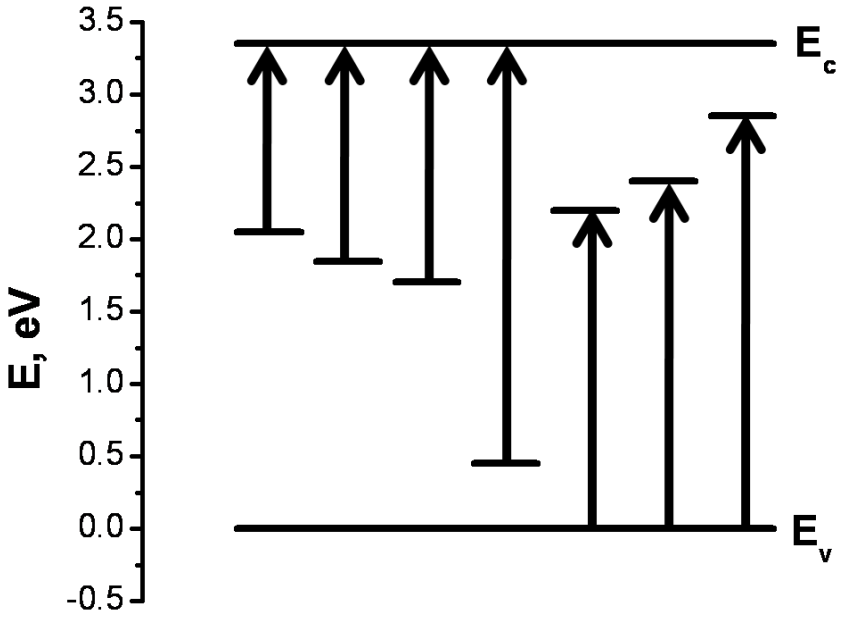

Figure 4.7: Synoptic diagram of the most common SPV transitions observed in the studied samples.

IV.2.2 Correlation with PAS and PL results

To further investigate the nature of these states and to elucidate their surface vs. bulk character, we performed comparison of the SPV spectra with the PL and PAS data

discussed above. From the Gaussian-resolved fits of the PL spectra we identified characteristic emissions at ~ 2.2 eV and ~ 2.4 eV, and ~ 2.9 eV (see Table 3.1), which were also observed in many of the SPV spectra (see, for example, Figure 4.6). Similar transitions observed in both PL and SPV spectra suggest that the states with those spectral features may be present in the bulk and the surface of the nanocrystals. From the SPV spectra one can find that the energy transitions at ~ 2.2 eV and ~ 2.9 eV are from the valence band to a state within the band gap and can be tentatively assigned to oxygen interstitials. However the defect level ~ 2.40 eV corresponds to a transition from the defect level to the conduction band. SA specimen shows the highest values of τ_M (298 – 301 ps, cf. Chapter III). The shortest average LT among the nanocrystals was obtained for the ZA and ZB samples consisting of larger grain sizes (cf. Chapter III.). One can argue that the SA sample shows the highest occurrence of zinc vacancies among all the as-received samples. These defect states could be associated with the ~ 1.65 eV transitions to the conduction band, ~ 2.05 eV to the conduction band, ~1.90 eV to the conduction band, and ~ 2.7 eV to the conduction band. In the case of pelletized and plasma treated samples the tentative analysis implies a presence of zinc vacancies, consistent with the PAS spectra. It is likely that oxygen vacancies are essentially invisible in PAS measurements because they are mostly neutral or positively charged and thus unlikely to trap positrons. Some authors suggested that Zn vacancy is the dominant native acceptor defect in an *n*-type ZnO [6].

IV.2.3 Complementary transitions

One advantage of obtaining both transitions from and into a given surface state is that it helps to verify the value of E_t (cf. II. 1.2). In addition, complementary transitions conveniently allow us to distinguish between transitions related to surface states and other possible bulk transitions. This principle shows that the same surface state is involved in both transitions. Several complementary transitions were detected in the studied samples. Figure 4.8 below shows two such pairs, with tentative assignments to oxygen vacancies and oxygen interstitials.

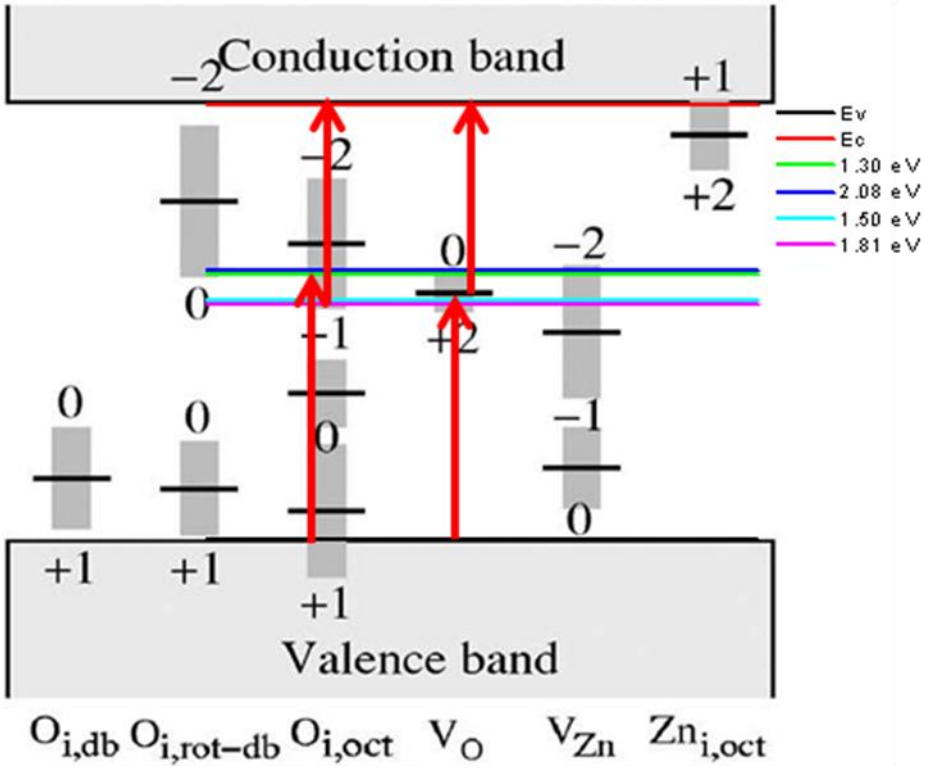

Figure 4.8: Examples of complementary SPV transitions observed in ZnO nanopowders.

IV.2 Effects of oxygen plasma treatments

SPV experiments revealed substantial oxygen plasma-induced changes for practically all the samples. A greater variety of transitions was observed, with defect energetics strongly dependent on a specific sample, as well as plasma parameters. In the plasma-treated samples we generally observed two common effects – a much better signal-to-noise ratio and much faster light-dark equilibration times (see below), both of which may point to a substantial increase of surface charge density. Alternatively, similar to [62] one can argue that oxygen plasma species may be absorbed by the relatively oxygen-deficient surface and thus increase the induced field in the space-charge region, which in turn will enhances the electron-hole pair separation.

Importantly, for several RP-treated samples we observed time evolution of the SPV spectral features, when those samples remained in the characterization chamber for extended periods of time and the spectra were collected on the same spot with an interval of one to several days. We omit detailed description of this spectral evolution and defer such discussion to our further reports. Nevertheless, we have to emphasize in this regard the importance of running our experiments in vacuum, when the plasma-modified surface properties are practically unaffected by the common air contaminants.

In addition to the energy positions of defect states from SPV experiments we can determine other important surface properties by analyzing the SPV transient behavior (see Chapter II). The approach used in the generation of these dependencies involves direct excitation of the surface states via a super-bandgap excitation. Importantly, we may be able to determine the effects of the plasma-induced changes on these surface state

properties such as the change in the surface potential given by $\delta V_s^0 = V_s^1 - V_s^0$. This is essentially the difference of the surface potential heights before and after illumination.

Analysis of the oxygen/helium plasma-induced changes in the transient characteristics indicates a much faster light-dark equilibration times. The saturation times are reduced from hours to essentially minutes, such as shown in figures. 4.9 and 4.10 (note the logarithmic time scale). Further analysis of the plasma-induced changes in the transient characteristics points to an increase of the majority carrier concentration at the surface. For instance, for the SA sample there is a plasma-induced increase in the majority concentration by three orders of magnitude.

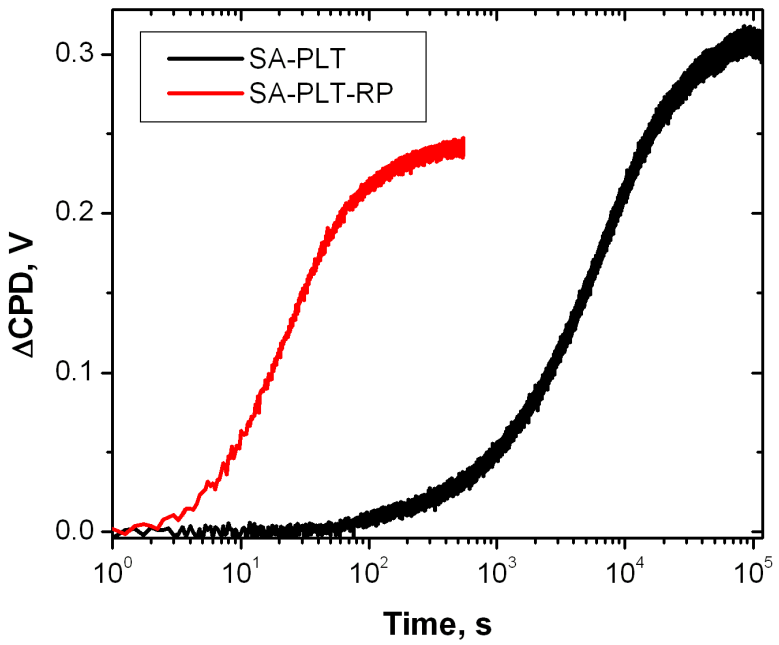

Figure 4.9: Time transient spectra for the SA pellets before and after remote oxygen plasma treatment.

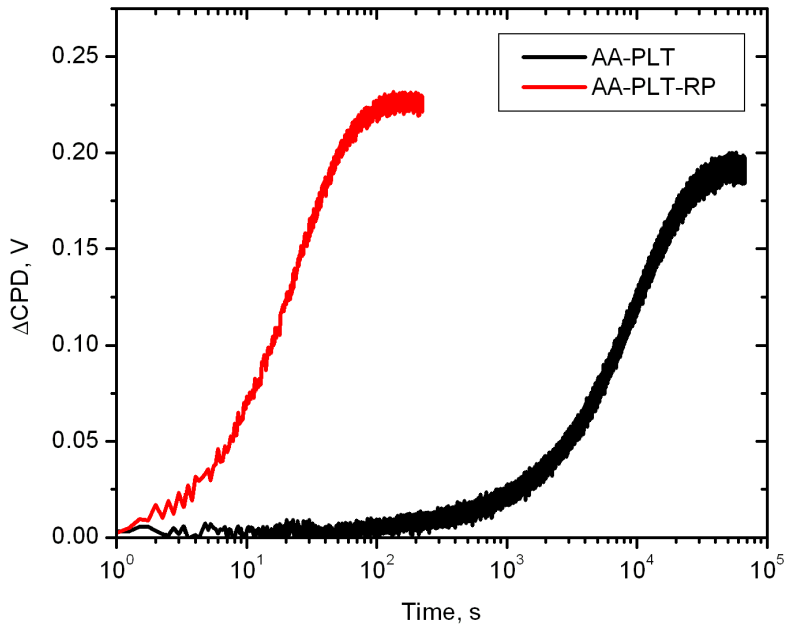

Figure 4.10: Time transient spectra for the AA pellets before and after remote oxygen plasma treatment.

Thus, the SPV measurements for nanopowder ZnO samples performed in tandem with RP treatments were used to determine surface state energetics. Our experiments identified a number of defect signatures present in the spectra of different samples. Assignments of these transitions to native point defects are tentative and require further elucidation and adequate surface-specific theoretical calculations. We demonstrated that both pelletization of the powders and oxygen plasma treatment lead to a significant improvement of the SPV signal, as well as overall evolution of the spectra. Moreover, oxygen treatment of the samples leads to a substantial increase in the near-surface concentration of the majority carriers. Our observations also provide a good example of plasma serving as a supplementary probe of surface properties.

Chapter V. Conclusions

In our work, we successfully designed and built a multi-chamber UHV setup featuring a combination of *in situ* surface-specific and surface-sensitive characterization and processing techniques such as SPV, AES, RP, and *in vacuo* resistive annealing. Using this system, we performed studies of defect properties of ZnO nanopowders. *Ex situ* characterization experiments (PAS/LT and PL) were performed as well and correlated with SPV results to expand our ability to identify surface and subsurface defects in the studied specimens. Samples were also treated with remote plasma for possible modification of their surface properties.

In our experiments, SPV in tandem with PL has been employed to characterize optoelectronic properties of nanocrystalline ZnO samples, and PAS to probe the free volume in those samples. We found that the magnitude of the average lifetimes for all the ZnO nanopowders is much higher than that of the reference ZnO single crystal. This difference can be qualitatively be interpreted as a considerable abundance of a free volume in nanoscale samples. Similarly, the comparison between PAS/LT measurements of the as-received powders and pelletized samples provided evidence of a significant contribution of an intergranular space. The correlation between the mean LT values and PL emission features on the one hand and the average nanocrystal size on the other is not very insignificant, which exposes a much stronger influence of the quality of individual powders and overshadows possible scaling effects. Nevertheless, our results are consistent with a substantial increase of a free surface in the nanopowder samples as a source of a higher concentration of defects within the surface and subsurface layers.

For our nanopowder ZnO samples, we further successfully probed surface state energetics by performing SPV measurements for as-received, pelletized and RP-treated nanopowders. The band gap energy E_g at ~ 3.3 eV was consistently measured in the spectra of all the nanopowder samples, including those with the smallest grain size. The downward bending of the band gap transitions in the SPV spectra confirmed the *n*-type nature of the ZnO nanopowder samples.

Moreover, to the best of our knowledge, for the first time in ZnO nanopowders, numerous and distinct defect-related SPV transitions were observed for all the studied specimens. Assignments of the defect signatures present in the spectra of the various samples to native point defects are tentative and require further elucidation and adequate surface-specific theoretical calculations. These states are widely distributed within the band gap. Some of the observed states are also detected in the bulk of the sample by the photoluminescence spectroscopy. Moreover, SPV was used to determine the acceptor vs. donor nature of the common features that were also observed in PL. Among the tentatively assigned surface states were Zn vacancies, which might be the reason for the higher lifetimes observed in the PAS/LT experiments. Therefore, in this report we demonstrated that the combination of in SPV, PAS, and PL could serve as a powerful tool to study the bulk and surface properties of semiconductor materials, including those with nanoscale dimensions.

It was demonstrated that the surface treatment has the potential to reveal surface versus bulk nature of the energies of states in the band gap. Both pelletization and oxygen plasma treatment lead to a significant improvement of the SPV signal. Oxygen plasma treatment of the samples leads to a substantial changes in the near-surface

electronic properties evidenced in a significant reduction of the surface potential saturation rates. Oxygen plasma-induced changes in the signal-to-noise ratio as well as the transient characteristics indicate possible increase of the majority carrier concentration at the surface. Alternatively, oxygen plasma species may be absorbed by the ZnO surface and increase the induced field in the space-charge region, thus enhancing the electron-hole pair separation. On the one hand, remote plasma may also contribute to the removal of the surface contamination in the samples and can therefore serve as an efficient tool for nanoscale semiconductor surface cleaning.

Chapter VI. Future Plans

We plan to use plasmas other that oxygen (e.g. hydrogen, nitrogen, etc.) to determine the best strategies to modify the surface states of the studied samples. In addition, new protocols will be tried to optimize the plasma treatment parameters.

The employment of the installed *in situ* heating equipment will substantially expand our surface modification abilities. The plan is to perform experiments involving a sequence of characterization and controlled annealing at various temperatures and in different environments – vacuum and RPs. Surface-specific properties will be monitored vs. various heating procedures. Importantly, combination of RP treatments with *in vacuo* high-temperature processing will significantly broaden our efficiency in tailoring surface structural, chemical, and electronic properties. Hitherto, there are only a few published results on the effects of controlled heating done simultaneously with RP treatment.

AES will be used to assess correlations between surface stoichiometry, surface states, and specific surface treatments. We will employ our UHV characterization (AES and SPV) together with RP and annealing treatments as well as PL and other *ex vacuo* tools to further elucidate surface properties in nanoscale ZnO. Recently in our group we started AES characterization of the studied ZnO nanopowders. Auger spectrum of one of the as-received specimens is shown in Figure 6.1. It reveals an oxygen-rich and somewhat contaminated surface of a ZnO nanopowder. The influence of the surface cation/anion balance and the chemisorbed/physisorbed foreign species on the surface states is of particular interest for us.

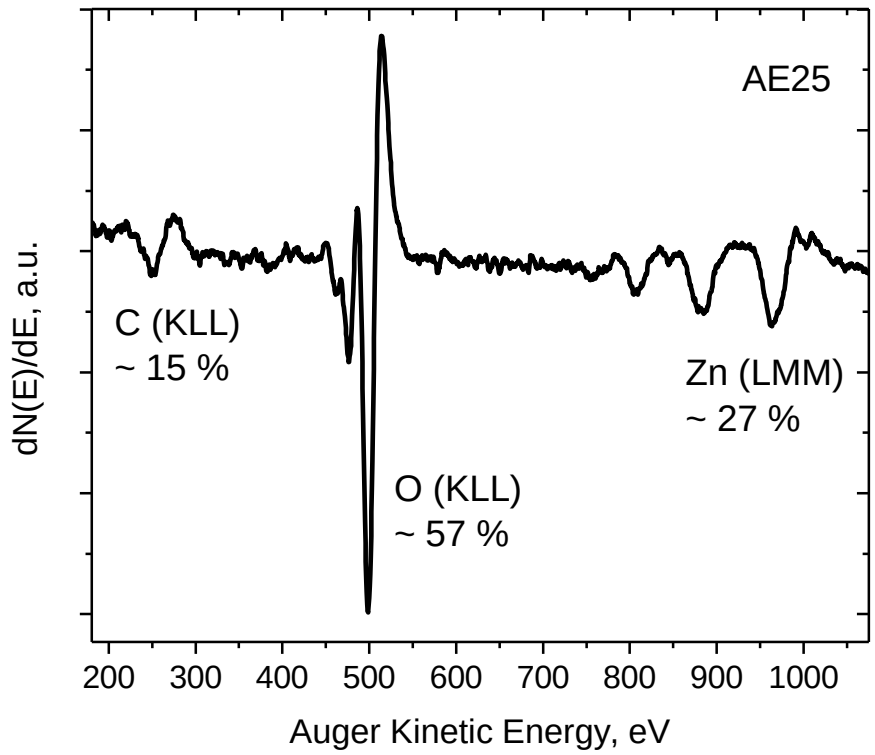

Figure 6.1: Auger spectrum showing surface composition of the AE25 pellet.

We also intend to broaden our studies by employing ZnO nanosystems of more complex morphologies. Investigations of such samples with more specific range of size distributions well controlled by the growth parameters will clarify influence of the scaling effects on the behavior of the surface properties.

Nanoscale materials other than ZnO are also of interest for our group. Currently we run experiments on nanopowders of complex perovskite oxides ($Ba_xSr_{1-x}TiO_3$, $SrTiO_3$), nanodiamonds, thin films of binary/ternary oxides containing TiO_2 and ZrO_2, thin film $ZnO/La_{1-x}Sr_xMnO_3$ interfaces, etc.

Appendix A

In this section (Table A.1) we provide a synopsis of the positron lifetime fitting results obtained for the studied ZnO nanopowders. The LT program (version 9) was employed to determine these lifetime values τ_i and their relative intensities I_i. The fits were performed using three lifetime components denoted in the table as τ_1, τ_2, and τ_3. Their relative intensities are labeled as I_1, I_2, I_3 respectively. The *VFit* column contains values of variances for each fit. We chose three different seed values for τ_1: 140 ps, and 160 ps and 180 ps. Interestingly, we found that for those different seed values the obtained variances were close to 1.00, an indication of a good fit. The first two components τ_1 (below 200 ps) and τ_2 (above 300 ps) were predominant, whereas the τ_3 component (ranging between slightly below 1 ns to several ns) was substantially weaker.

Sample	*VFit*	τ_M *(ps)*	τ_1*(ps)*	I_1 *(%)*	τ_2*(ps)*	I_2 *(%)*	τ_3*(ps)*	I_3 *(%)*
SA	1.063	278	142	37.2	379	52.1	1910	0.6
	1.060	285	159	49.6	388	49.8	2120	0.6
	1.060	292	178	52.8	399	46.7	3420	0.4

Sample	*VFit*	τ_M *(ps)*	τ_1*(ps)*	I_1 *(%)*	τ_2*(ps)*	I_2 *(%)*	τ_3*(ps)*	I_3 *(%)*
AA	1.068	281	149	49.0	387	50.4	2150	0.6
	1.068	287	165	51.5	396	48.0	2370	0.5
	1.062	294	180	54.3	405	45.2	2560	0.5

Sample	*VFit*	τ_M *(ps)*	τ_1*(ps)*	I_1 *(%)*	τ_2*(ps)*	I_2 *(%)*	τ_3*(ps)*	I_3 *(%)*
AE025	1.033	286	149	52.3	378	46.3	2335	1.4
	1.022	292	162	54.3	385	44.3	2385	1.4
	1.016	298	180	58.3	399	40.4	2468	1.3
AE031	1.069	282	148	48.3	376	50.6	1842	1.1
	1.069	288	160	49.7	381	49.2	1872	1.1
	1.069	293	177	53.2	392	45.8	1950	1.0

Sample	*VFit*	τ_M *(ps)*	τ_1*(ps)*	I_1 *(%)*	τ_2*(ps)*	I_2 *(%)*	τ_3*(ps)*	I_3 *(%)*
ZA	1.018	253	144	55.3	377	44.3	1580	0.4
	1.012	259	158	58.2	389	41.5	1970	0.3
	0.997	265	175	59.5	391	40.2	1350	0.3
ZB	1.051	254	141	50.5	355	48.4	1020	1.1
	1.050	261	158	55.2	373	44.1	1260	0.7
	1.051	268	178	60.5	393	39.1	1590	0.4

Table A. 1: PAS LT fitting results for the studied ZnO nanopowders employing three different seed value of the first lifetime components τ_1: 140 ps, 160 ps and 180 ps.

Appendix B

In this Appendix we provide supplemental information on the additional SPV transitions observed in the studied ZnO nanopowders. Table A.1 provides summary of these features. Figures A.1 to A.11 represent tentative assignments of the observed transitions to native point defect levels. Figure A.12 shows also a synoptic diagram containing these transitions.

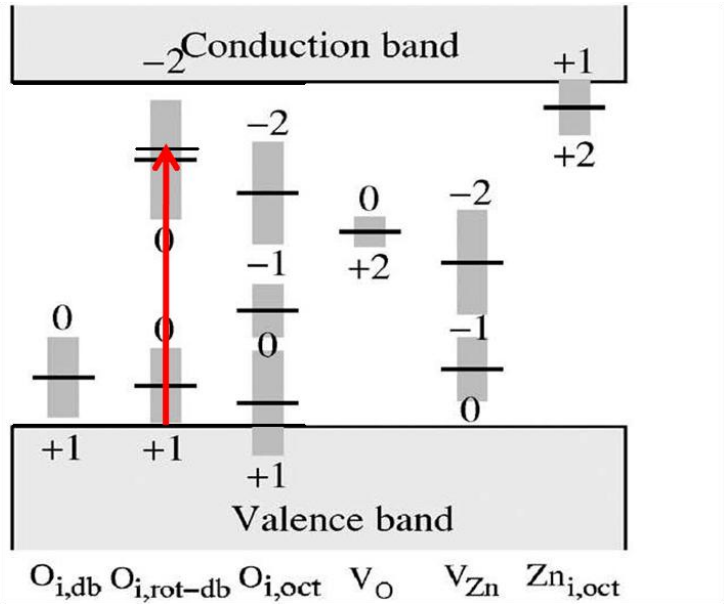

Figure A.1: ~ 2.7 eV SPV transition from the valence band.

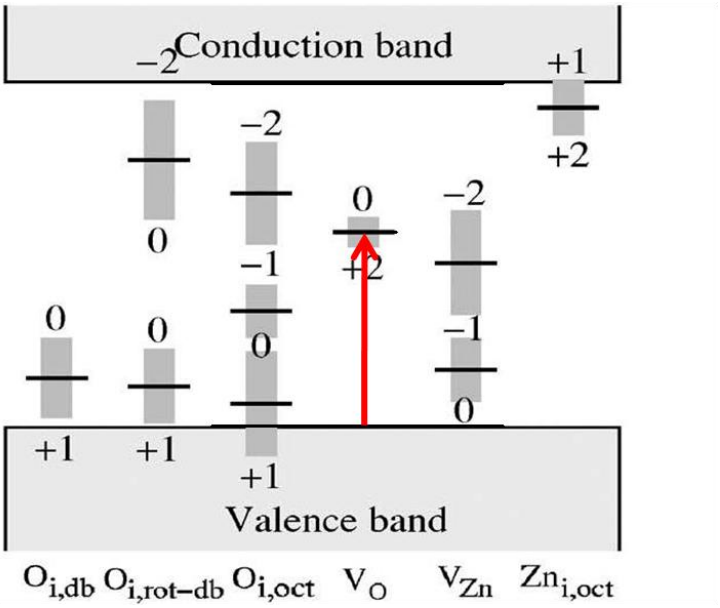

Figure A.2: ~ 1.9 eV SPV transition from the valence band.

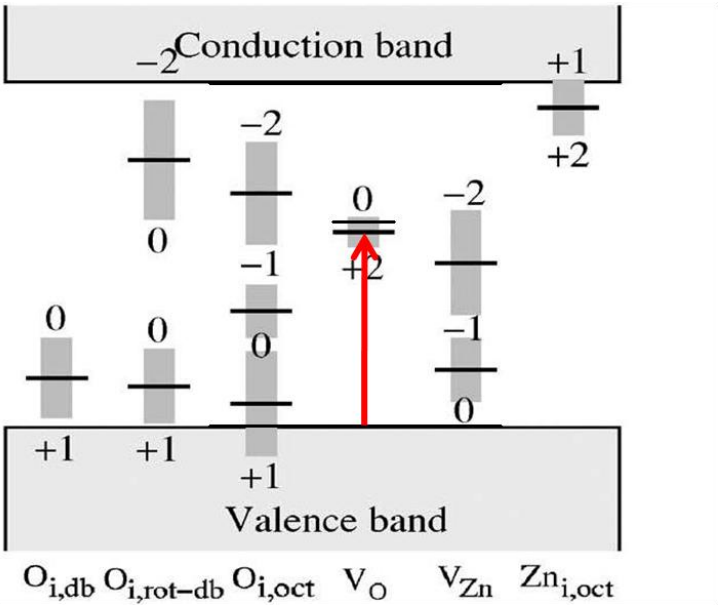

Figure A.3: ~ 2.0 eV SPV transition from the valence band.

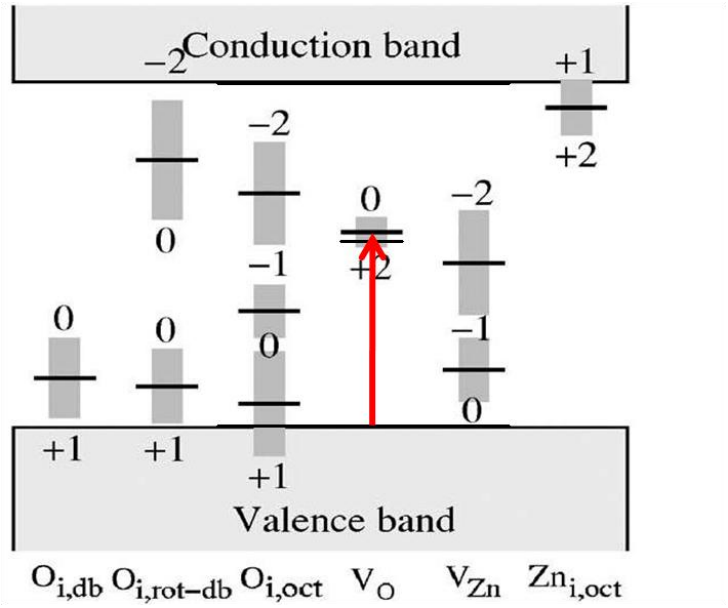

Figure A.4: ~ 1.8 eV SPV transition from the valence band.

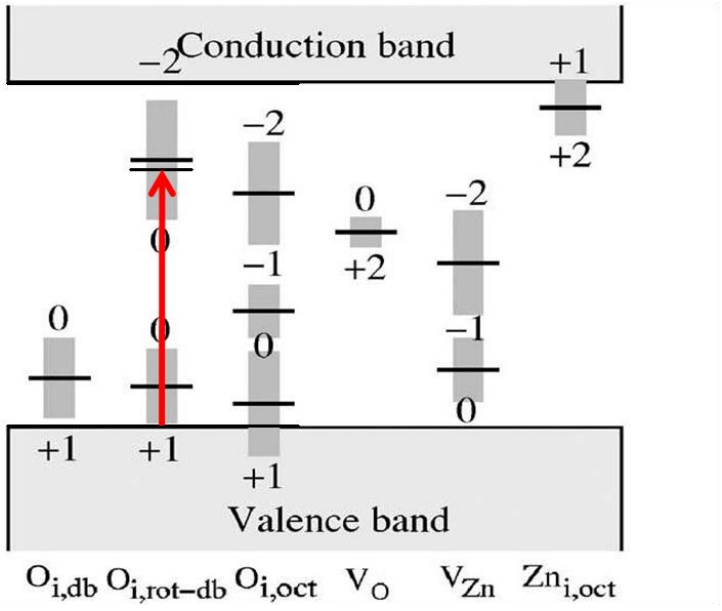

Figure A.5: ~ 2.5 eV SPV transition from the valence band.

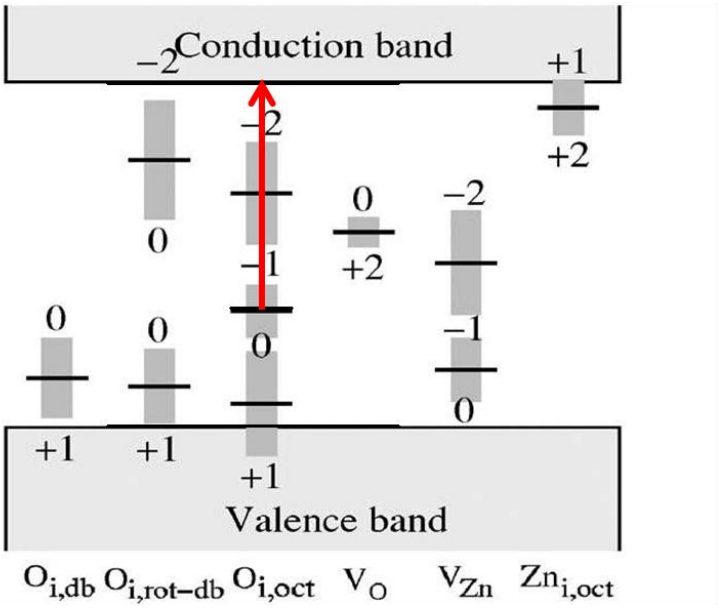

Figure A.6: ~ 2.2 eV SPV transition to the conduction band.

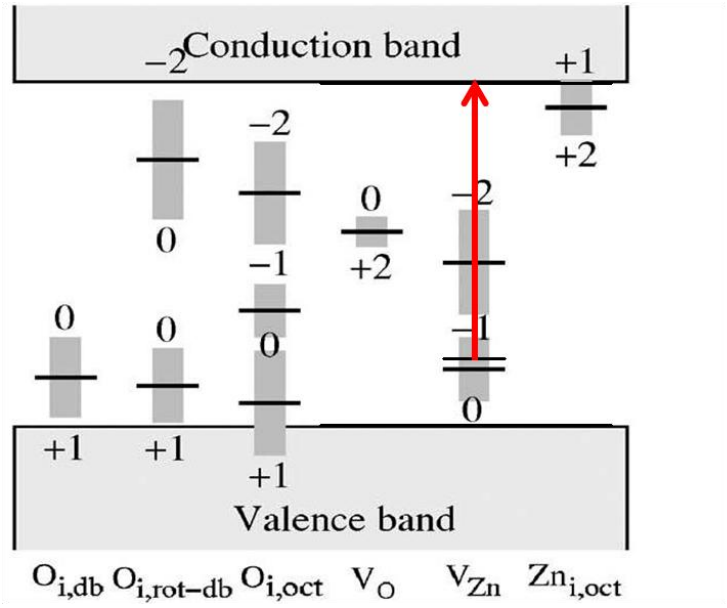

Figure A.7: ~ 2.7 eV SPV transition to the conduction band.

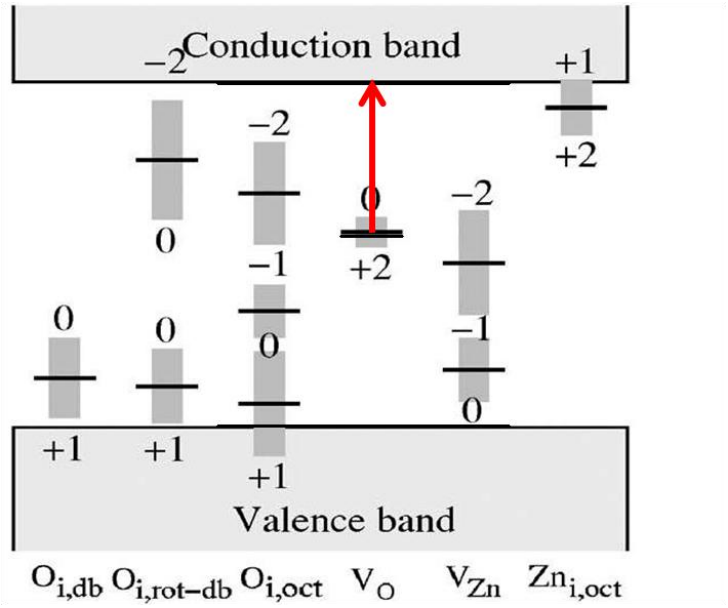

Figure A.8: ~ 1.5 eV SPV transition to the conduction band.

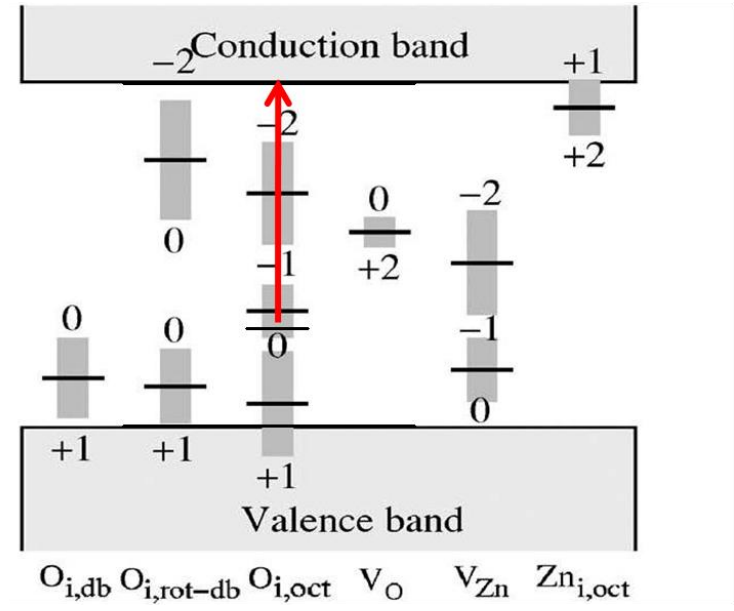

Figure A.9: ~ 2.4 eV SPV transition to the conduction band.

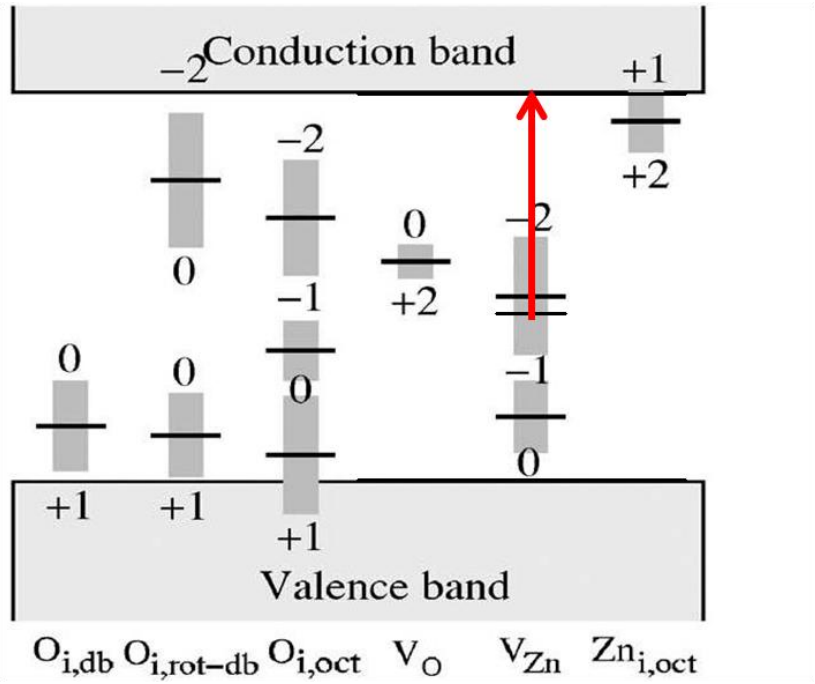

Figure A.10: ~ 1.9 eV SPV transition to the conduction band.

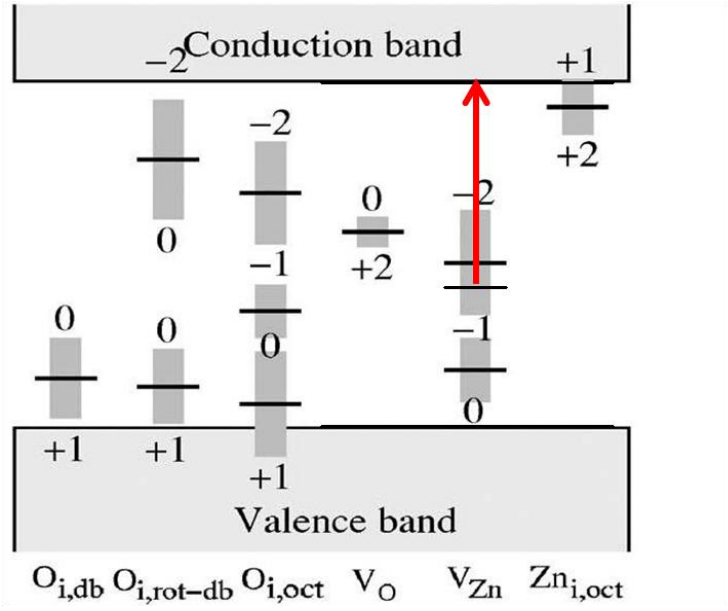

Figure A.11: ~ 2.0 eV SPV transition to the conduction band.

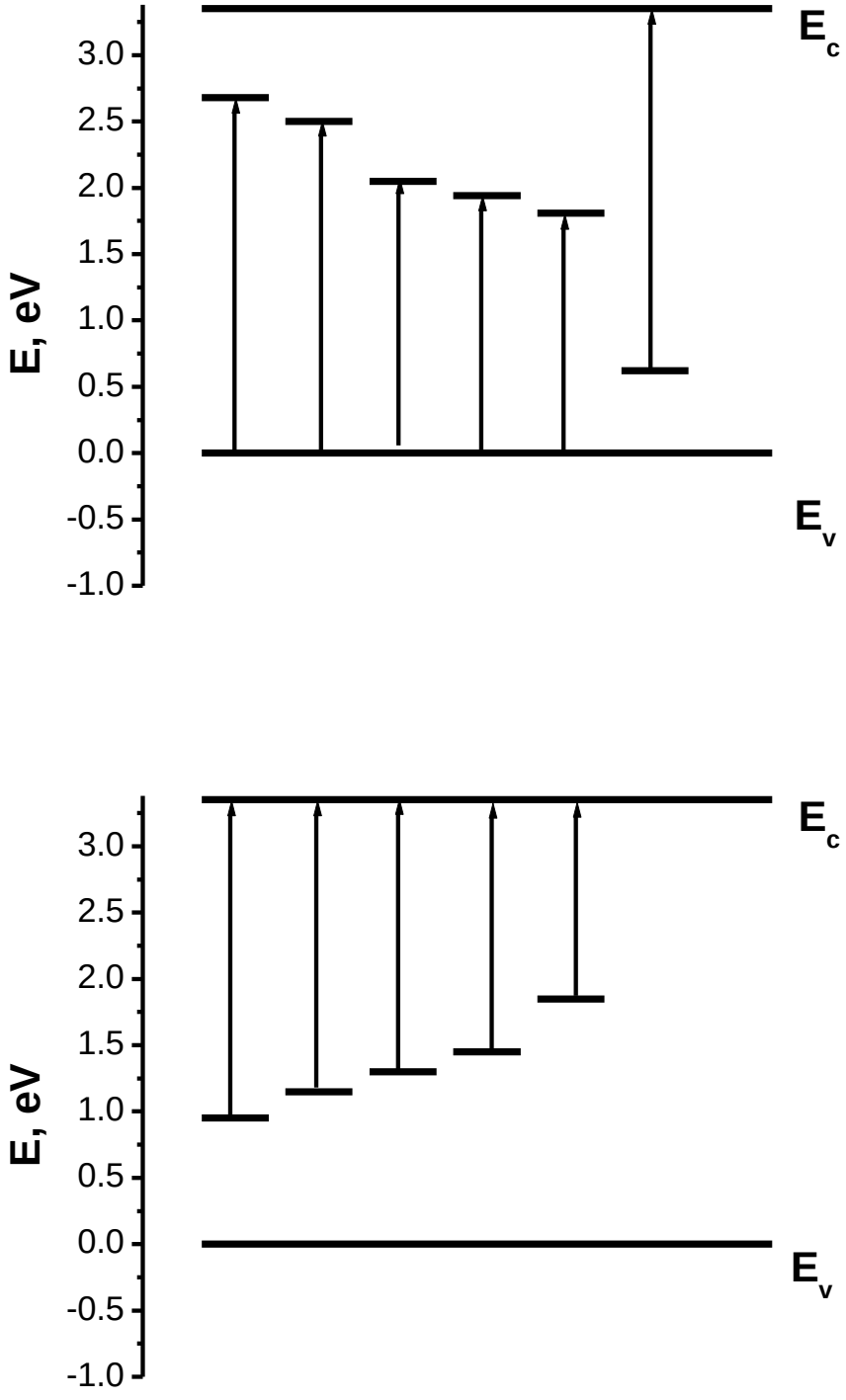

Figure A.12: Synoptic diagram of the additional SPV transitions observed in the studied samples.

	~ (E_c -E) /eV	~ (E_V + E) /eV
AE31	1.5, 1.7, **2.1**,1.9, 2.2, 2.4	2.5,
AE31-RP	1.5, 1.7, **2.1,** 1.6	2.5
AE25	2.2	
AE25-RP	1.9	
SA	1.8, 2.0, 2.7	2.6
SA-RP	1.8	2.4
Z	1.8, 2.1, 2.4	2.6,
Z-RP	1.8, 2.1, 2.4	2.1
AA	1.9, 1.5, 2.2, 2.4	
AA-RP	1.5, 1.9	2.4

Table A.2: Summary of the additional SPV transitions observed in the studied samples.

References

[1] D. Gal, Y. Mastai, G. Hodesa, and L. Kronik, *J. Appl. Phys.*, Vol. 86, **10**, 15 (1999).

[2] C. Kittel, *Introduction to Solid State Physics*, 4th edition, Wiley, 1972.

[3] B. G. Streetman, *Solid State Electronic Devices*, 3rd edition, Prentice Hall, New Jersey 1990.

[4] F. Tuomisto, K Saarinen, D. C. Look and G. C. Farlow, *Phys. Rev. B*, **72**, 085206 (2005).

[5] http://upload.wikimedia.org/wikipedia/commons/6/60/Zincite-3D-balls.png.

[6] Z. Q. Chen, S. Yamamoto, M. Mamoto, M. Maekawa, A. Kawasuso, X. L. Yuan and T. Sekiguchi, *J. Appl. Phys.* **94**,8 (2003).

[7] F. Tuomisto, V. Ranki, K. Saarinen and D. C. Look, *Phys. Rev. Lett.*, **91**, 20 (2003).

[8] G. Brauer, W. Anward, W. Skorupa, J. Kuriplach, O. Melikhova,C. Moisson, H. Von Wenckstern, H. Schmidt, M. Lorenz and M. Grundmann, *Phys. Rev. B* **74**, 045208 (2006).

[9] S.Dutta, M. Chakrabarti, S. Chattopadhyay, D. Jana, D. Sanyal, and A. Sarkar, *J. Appl. Phys*. **98,** 053513 (2005).

[10] Z. Q. Chen, A. Kawasuso, Y. Xu, H. Naramoto, X. L. Yuan, T. Sekiguchi, R. Suzuki and T. Ohdaira, *Phys. Rev. B.*, **71**, 115213 (2005).

[11] Z. Q. Chen, K. Betsuyaku and A. Kawasuso, *Phys. Rev. B* **77**, 113204 (2008).

[12] Z. Q. Chen, S. J. Juan, M. Maekawa, A. Kawasuso, H. Naramoto, X. L. Yuan, and T. Sekiguchi, *Phys. Rev. B,* **75,** 245206 (2007).

[13] L. Kronik, Y. Shapira, *Surface Science Reports* **37,** 1-206 (1999).

[14] L. J. Brilson, 1992, in: *Surface and interfaces: Atomic-Scale Structure, Band Bending and Band offsets,* ed P. T. Landsberg, Basic Properties of Semiconductors, Vol. I (New York) Ch. 7.

[15] K. Li, D. Wang, F. Wu, T. Xie, and T. Li, *Mater. Chem. and Phys.* **64,** 269-272 (2000).

[16] *Nanoscale Science and Technology* Edited by R. W. Kelsall, I. W. Hamley and M. Geoghegan, John Wiley and Sons, Ltd, 2005.

[17] J. Liqiang, W. Baiqi, X. Baifu, L. Shudan, S. Keying, C. Weimin, and F. Honggang, *J. Solid State Chemistry* **177**, 4221-4227 (2004).

[18] A. M. Fischer, S. Srinivasan, R. Garcia, F. A. Ponce, S. E. Guaño, B. C. Di Lello, F. J. Moura, and I. G. Solórzano, *App. Phys. Lett.* **91,** 121905 (2007).

[19] H. L. Mosbacker, Y. M. Strzhemechny, B. D. White, P. E. Smith, D. C. Look, D. C. Reynolds, C. W. Litton, and L. J. Brillson, *App. Phys. Lett.* **87**, 012102 (2005).

[20] D. C. Look, H. L. Mosbacker, Y. M. Strzhemechny, and L. J. Brillson, *Superlattices and Microstructures* **38,** 406-412 (2005).

[21] F. Xu, K. Yu, G. Li,Q. Li, and Z. Zhu. *Nanotechnology* **17**, 2855 (2006).

[22] T. Hirai, Y. Harada, S. Hashimoto, N. Ohno, and T. Itoh, *J. Luminescence* **113,** 115-120 (2005).

[23] J. Grabowska, K. Nanda, E. McGlynn, J.-P. Mosnier, M. O. Henry, A. Beaucamp, and A. Meaney, *J. Mater. Sci. Materials in Electronics* **16,** 397-401 (2005).

[24] J. Grabowska, A. Meaney, K. K. Nanda, J.-P. Mosnier, M. O. Henry, J.-R. Duclère, and E. McGlynn, *Phys. Rev. B* **71,** 115439 (2005).

[25] I. Shalish, H. Temkin, and V. Narayanamurti, *Phys. Rev. B* **69,** 245401 (2004).

[26] L. Wischmeier, T. Voss, S. Börner, and W. Schade, *Appl. Phys. A* **84,** 111-116 (2006).

[27] S. Sakohara, M. Ishida, and M. A. Anderson, *J. Phys. Chem. B* **102,** 10169-10175 (1998).

[28] L. Guo, S. Yang, C. Yang, P. Yu, J. Wang, W. Ge, and G. K. L. Wong, *Appl. Phys. Lett.* **76,** 2901-2903 (2000).

[29] J. Li, D. Zhao, X. Meng, Z. Zhang, J. Zhang, D. Shen, Y. Lu, and X. Fan, *J. Phys. Chem*. B **110,** 14685-14687 (2006).

[30] Y. Yang, B. K. Tay, X. W. Sun, J. Y. Sze, Z. J. Han, J. X. Wang, X. H. Zhang, Y. B. Li, and S. Zhang, *Appl. Phys. Lett*. **91,** 071921 (2007).

[31] Y. Yang, X. W. Sun, B. K. Tay, P. H. T. Cao, J. X. Wang, and X. H. Zhang, *J. Appl. Phys*. **103,** 064307 (2008).

[32] Y. M. Strzhemechny, *J. Vac. Sci. Technol.* A **24**, 1233 (2006).

[33] J. Čížek, N. Žaludová, M. Vlach, S. Daniš, J. Kuriplach, I. Procházka, G. Brauer, W. Anwand, D. Grambole, W. Skorupa, R. Gemma, R. Kirchheim, and A. Pundt, *J. App. Phys.* **103**, 053508 (2008).

[34] K. Oura, V. G. Liftshits, A. Saranin, A. V. Zotov, and M. Katayama, *Surface Science,* Springer, New York 2003.

[35] H. C. Gatos and J. Lagowski, *J. Vac. Sci. Technol*. **10,** 130 (1973).

[36] J. Lagowski et al, *Surface Science* **29,** (1972) 203-212.

[37] A. Zangwill, *Physics at surfaces,* Cambridge University Press, New York 1988.

[38] D. K. Schroder, *Semiconductor and Device Characterization,* John Wiley and Sons Inc, New York 1998.

[39] S. M. Sze, *Physics of semiconductor Devices*, 2nd edition, Wiley Interscience 1981.

[40] R. F. Bunshah, *Handbook of Deposition Technologies for films and coatings*, 2nd edition, Noyes, New Jersey 1994.

[41] D. K. Schroder, *Semiconductor and Device Characterization,* John Wiley and Sons Inc, New York 1998.

[42] *Handbook of plasma processing technology: fundamentals, etching, deposition, and surface interactions* / edited by S. M. Rossnagel, J. J. Cuomo, W. D. Westwood, and Noyes Publications 1990.

[43] K. Becker and A. Belkind, *Introduction to plasmas, Vacuum Technology and Coating,* October 2007, A. Belkind, *How plasmas are made,* Vacuum Technology and Coating, 2007.

[44] L. Kronik and Y. Shapira, *Surf. Interface Anal.* **31,** 954–965 (2001).

[45] I. Procházka, *Materials Structure*. **8**, 2 (2001).

[46] J. Cizek et al, *J. Appl. Phys*. **103,** 053508 (2008).

[47] G. Brauer, J. Kuriplach, J. Cizek, W. Anwand, O. Melikhova, I. Prochazka, and W. Skorupa, *Vacuum* **81,** 1314-1317 (2007), and references therein.

[48] S. Dutta, et al., *J. Phys: Condens. Matter*. **19**, 236218 (2007).

[49] A. K.Mishra, S. K. Chaudhuri, S. Mukherjee, A. Priyam, A. Saha, and D. Das, *J. Appl. Phys*. **102,** 103514 (2007).

[50] T. Ghoshal, S. Biswas, S. Kar, S. Chaudhuri and P. M. G. Nambissan, *J. Chemical Physics* **128**, 074702 (2008).

[51] "Correlation between optoelectronic and positron lifetime properties in as-received and plasma-treated ZnO nanopowders", R. M. Peters, J. A. Paramo, C. A. Quarles, and Y. M. Strzhemechny, in *Application of Accelerators in Research and Industry*, edited by F. D. McDaniel and B. L. Doyle, AIP, 965-969, (2009).

[52] L. C. Damonte, L. A. Mendoza Zélis, B. Marí Soucase, and M. A. Hernández Fenollosa, *Powder Technology* **148** 15-19 (2004).

[53] S. Dutta, S. Chattopadhyay, D. Jana, A. Banerjee, S. Manik, S. K. Pradhar, M. Sutradhar, and A. Sarkar, *J. Appl. Phys*. **100,** 114327 (2006).

[54] P. Erhart, K. Albe, and A. Klein, *Phys. Rev. B* **73,** 205203 (2006)

[55] J. A. Paramo, R. M. Peters, C. A. Quarles, H. Vallejo, and Y. M. Strzhemechny, *IOP Conf. Series: Materials Science and Engineering* **6,** 012030 (2009).

[56] "Identification and control of surface defect properties in nanoscale ZnO", Y. M. Strzhemechny, J. A. Paramo, R. M. Peters, C. A. Quarles, H. Vallejo, M. Bitenc, Z. Crnjak Orel, and T. Endo, submitted to *Journal of The Ceramic Society of Japan*.

[57]"Correlation between morphology and defect luminescence in precipitated ZnO nanorod powders", M. Bitenc, P. Podbršček, Z. Crnjak Orel, M. A. Cleveland, J. A. Paramo, R. M. Peters, and Y. M. Strzhemechny, *Crystal Growth & Design* **9,** 997 (2009).

[58] L. Jing, X. Sun, J. Shang, W. Cai, Z. Xu, Y. Du, and H. Fu, *Solar Energy Materials & Solar Cells* **79,** 133–151 (2003).

[59] L. Jing, Z. Xu, X. Sun, J. Shang, and W. Cai, *Applied Surface Science* **180,** 308 (2001).

[60] Y. Lin, D. Wang, Q. Zhao, M. Yang, and Q. Zhang, *J. Phys. Chem. B* **108,** 3202 (2004).

[61] L. Jing, B. Wang, B. Xin, S. Li, K. Shi, W. Cai, and H. Fu, *Journal of Solid State Chemistry* **177**, 4221 (2004).

[62] Y. Lin, D. Wang, Q. Zhao, Z. Li, Y. Ma, and M. Yang, *Nanotechnology* **17**, 2110 (2006).

[63] Q. Zhao, T. Xie, L. Peng, Y. Lin, P. Wang, L. Peng, and D. Wang, *J. Phys. Chem. C*, **111**, 17136 (2007).

[64] H. Dember, *Phys. Z.* **32**, 554 (1931).

[65] L. Yanhong, W. Dejun, Z. Qidong, Y. Min, and Z. Qinglin, *J. Phys. Chem. B* ***108***, 3202-3206 (2004).

[66] J. Liqiang, S. Xiaojun, S. Jing, C. Weimin, X. Zili, D. Yaoguo, and F. Honggang, *Solar Energy Materials & Solar Cells* **79** 133-151 (2003).

[67] "R. M. Peters, S. Glancy, J. Paramo, and Y. M. Strzhemechny: "In Situ Surface Photovoltage Spectroscopy of ZnO Nanopowders Processed by Remote Plasma", in *Zinc Oxide and Related Materials — 2009,* edited by S. Durbin, M. Allen, and H. von Wenckstern (Mater. Res. Soc. Symp. Proc. **Volume 1201**, Warrendale, PA, 2010), H03-03.

VITA

Personal Background	Raul Mugabe Peters Son of Anderson Peters and Julie Mae George
Education	Bachelor of Science, Physics & Mathematics, Midwestern State University, Wichita Falls, Texas, 2005 Doctor of Philosophy, Physics, Texas Christian University, Fort Worth, 2010
Experience	Research/Teaching Assistantship, Texas Christian University Fort Worth, TX, 2005- 2010 High School Teacher, Ministry of Education, St Johns, Antigua, 2000-2002
Professional Memberships	American Physical Society, Materials Research Society, National Society of Black Physics Students Sigma Pi Sigma National Physics Honor Society

1. R. M. Peters, Stephen Glancy, J. Paramo, Y. M. Strzhemechny: "In Situ Surface Photovoltage Spectroscopy of ZnO Nanopowders Processed by Remote Plasma", in *Zinc Oxide and Related Materials — 2009*, edited by Steve Durbin, Martin Allen, and Holger von Wenckstern (Mater. Res. Soc. Symp. Proc. **Volume 1201**, Warrendale, PA, 2010), H03-03.

2. "Identification and control of surface defect properties in nanoscale ZnO", Y. M. Strzhemechny, J. A. Paramo, R. M. Peters, C. A. Quarles, H. Vallejo, M. Bitenc, Z. Crnjak Orel, and T. Endo, submitted to *Journal of The Ceramic Society of Japan*.

3. "Defect properties of ZnO nanopowders and their modifications induced by remote plasma treatments", J. A. Paramo, R. M. Peters, C. A. Quarles, H. Vallejo, and Y. M. Strzhemechny, *IOP Conf. Series: Materials Science and Engineering* **6**, 012030 (2009).

4. "Correlation between optoelectronic and positron lifetime properties in as-received and plasma-treated ZnO nanopowders", R. M. Peters, J. A. Paramo, C. A. Quarles, Y. M. Strzhemechny, in *Application of Accelerators in Research and Industry*, ed. F. D. McDaniel and B. L. Doyle, AIP, pp. 965-969, (2009).

5. "Correlation between morphology and defect luminescence in precipitated ZnO nanorod powders", M. Bitenc, P. Podbršček, Z. Crnjak Orel, M. A. Cleveland, J. A. Paramo, R. M. Peters, Y. M. Strzhemechny, *Crystal Growth & Design* **9**, 997 (2009).

ABSTRACT

STUDIES OF SURFACE STATES IN ZINC OXIDE NANOPOWDERS

by Raul Mugabe Peters, Ph.D., 2010
Department of Physics and Astronomy
Texas Christian University

Dissertation Advisor:
Dr. Yuri M. Strzhemechny, Assistant Professor of Physics

The surface of ZnO semiconductor nanosystems is a key performance-defining factor in numerous applications. In this work we present experimental results for the surface defect-related properties of ZnO nanoscale systems.

Surface photovoltage spectroscopy was used to determine the defect level energies within the band gap, the conduction vs. valence band nature of the defect-related transitions, and to probe key dynamic parameters of the surface on a number of commercially available ZnO nanopowders. In our experimental setup, surface photovoltage characterization is conducted in high vacuum in tandem with *in situ* oxygen remote plasma treatments. Surface photovoltage investigations of the as-received and plasma-processed samples revealed a number of common spectral features related to surface states. Furthermore, we observed significant plasma-induced changes in the surface defect properties.

Ex situ positron annihilation and photoluminescence measurements were

performed on the studied samples and correlated with surface photovoltage results. The average positron lifetimes were found to be substantially longer than in a bulk single crystalline sample, which is consistent with the model of grains with defect-rich surface and subsurface layers. Compression of the powders into pellets yielded reduction of the average positron lifetimes.

Surface photovoltage, positron annihilation, and photoluminescence spectra consistently showed sample-to-sample differences due to the variation in the overall quality of the nanopowders, which partially obscures observation of the scaling effects. However, the results demonstrated that our approach is efficient in detecting specific surface states in nanoscale ZnO specimens and in elucidating their nature.